A MULTISCALE APPROACH TO MECHANICAL MODELING OF A LEAF PETIOLE: INTEGRATING CELL WALL, CELLULAR TISSUES, AND STRUCTURAL MORPHOLOGY

Written by:
TANVIR RAHMAN FAISAL

Doctor of Philosophy

Department of Mechanical Engineering

McGill University

Montreal,Quebec

October 2013

A thesis submitted to McGill University in partial fulfillment of the requirements for the degree of Doctor of Philosophy

DEDICATION

To my mother, Shamsun Nahar Rahman and my deceased father, A. K. M. Mukhlesur Rahman.

ACKNOWLEDGEMENTS

I would like to express my deepest gratitude to my supervisors Professor Damiano Pasini and Professor Alejandro D. Rey for their supervision, guidance, and encouragement during my doctoral study at McGill University. I would like to express special thanks to Professor Pasini, whose vision, enthusiasm, and dedication to this work motivated me developing an in depth understanding of the research topic. His thoughtful insights and detail feedback made a huge difference in my academic life, in writing several original research manuscripts, and this dissertation. I also would like to thank Professor Tamara Western for her valuable suggestions and collaboration for conducting the experiments, which made this dissertation more complete.

I would also like to thank Nicolay Hristozov for his continuous and diligent effort for conducting experiments. I have learned a lot about the biological experiments, working with him. I am also grateful to Lucy Federico, an undergraduate research student, for providing the micrographs of rhubarb tissues. In the same vein, I would also like to thank the administration and staff of the Montreal Botanical Garden for donating the *P. melinonii* petioles at the early stage of my research.

Furthermore, I also take the opportunity to thank all Pasini lab members, both past and present, for making the lab a congenial workplace. I especially thank Ehsan, the ANSYS guru, for being so helpful and accommodating. I have learned a lot about ANSYS and finite element modeling from him.

I would like also to thank the Graduate Secretary Ms Joyce Nault, and all the staff of the Department of Mechanical Engineering who were always eager to help. I graciously thank the Faculty of Engineering at McGill University and Fonds de recherche du Québec – Nature et technologies (FQRNT) for their

financial support.

Last but not the least, I am indebted to my mother whose inspiration and supports have always been with me, throughout my study. I would like to thank my sisters (Papri, Swati, and Buri), nephews and nieces, and my uncles, specially Sarwar Jahan and Sarwar Hasan; their unfailing support and love will always be remembered. Finally, I wish to express my extended and special thanks to my wife Tajeen for her support, understanding, and patience.

ABSTRACT

A plant is a natural hierarchical structure, which exhibits remarkable mechanical properties. The macro (scale) mechanical properties of a plant are the cumulative outcome of the structural properties of its preceding level of structural hierarchy. To develop engineering structures inspired by a plant and its organs, a comprehensive characterization of its mechanical properties exhibited at multiple hierarchical orders is essential to mimic such structures for engineering application.

This thesis presents a set of theoretical and computational models at various orders of the structural hierarchy to capture the overall structural properties of a plant petiole. The modeling method is framed within a multiscale mechanics framework, which is essential for any structure displaying hierarchical orders of organization. The macro structural properties, i.e. flexural and torsional stiffness, of a plant petiole are obtained by correlating cell wall construction, tissue microstructure, and structural shape morphology. The stiffness of the cell wall is modeled using the theory of a fiber reinforced composite material. The microarchitecture of the constituent tissues that govern the properties of the petiole are modeled with a novel algorithm – finite edge centroidal Voronoi tessellation (FECVT) – that is capable to provide a realistic visualization of the tissue. The effective stiffness properties of the constituent tissues are obtained via finite element analysis of the FECVT models coupled with cell wall properties. With the properties of the tissues, the cross-sectional shape of the petiole at the structural level is considered to determine its flexural and torsional stiffness, which are also validated experimentally for rhubarb petiole. This multiscale mechanical model will elucidate the role of each order of structural hierarchy to determine the structural compliance of the petiole.

A hierarchical modeling approach that captures the overall structural properties of a petiole has been introduced in this thesis. In particular, the model develops a relationship between the micro and macrostructural properties using a tailored multiscale mechanics approach. Therefore, this research can bridge the gap between plant biology and engineering to develop novel bio-inspired material and structures. This research can also help to develop fundamental knowledge of plant cellular bio-mechanics and its impact on the macroscopic mechanics of stems and petioles with the end goal of transferring this knowledge to the processing and design of compliant engineering structures and materials.

ABRÉGÉ

Une plante est une structure hiérarchique naturelle, qui présente des propriétés mécaniques remarquables. Les propriétés mécaniques à grande échelle d'une plante sont le résultat cumulatif des propriétés structurelles du niveau précédent de la hiérarchie structurelle. Pour développer des structures de génie inspirées par une plante et ses organes, une caractérisation détaillée de ses propriétés mécaniques manifestées aux multiples niveaux hiérarchiques est essentielle pour imiter ces structures pour les applications d'ingénierie.

Cette thèse présente un ensemble de modèles théoriques et numériques à divers niveaux hiérarchiques structuraux afin de capturer les propriétés structurelles aux niveaux globaux d'un pétiole d'une plante. La méthode de modélisation est cadrée au sein d'un système mécanique à niveaux multiples, qui est essentiel pour toute structure composée de plusieurs ordres hiérarchiques d'organisation. Les propriétés structurelles à grande échelle, c.à.d. la raideur en flexion et en torsion, d'un pétiole d'une plante sont obtenues par la corrélation entre la construction de la paroi cellulaire, la microstructure des tissus, et la morphologie de la forme structurelle. La raideur de la paroi cellulaire est modélisée en utilisant la théorie des matériaux composites à renfort fibreux. La microarchitecture des constituants des tissus qui gouverne les propriétés du pétiole est modélisée avec un nouveau algorithme – La tessellation de Voronoi de centre à bord fini (FECVT) – qui est capable de fournir une visualisation réaliste du tissu. La raideur effective des constituants des tissus est obtenue par la méthode des éléments finis des modéles FECVT accouplée avec les propriétés de la paroi cellulaire. La forme du pétiole en coupe transversale au niveau structural ensemble avec les propriétés des tissus sont considérées afin de déterminer sa raideur en flexion et en torsion, qui sont également validés

expérimentalement pour le pétiole de la rhubarbe. Ce modéle mécanique à échelles multiples éclaircira le rôle de chaque niveau de la hiérarchie structurelle pour déterminer la souplesse structurelle du pétiole.

Une méthode de modélisation hiérarchique qui capture les propriétés structurelles globales d'un pétiole a été introduite dans cette thèse. Notamment, le modèle établit une relation entre les propriétés du micro et macro niveaux structuraux en utilisant un procédé mécanique adapté, à échelles multiples. Par conséquent, cette recherche peut combler le vide entre la biologie végétale et le génie afin de développer de nouveaux matériaux et des structures bio-inspirées. Cette recherche peut également aider à développer les connaissances fondamentales de la biomécanique cellulaire des plantes et son impact sur la mécanique macroscopique des tiges et des pétioles avec l'objectif final de transférer ces connaissances pour le traitement et la conception des structures et matériaux souples de génie.

TABLE OF CONTENTS

LIST OF TABLES

LIST OF FIGURES

CHAPTER 1
Introduction

1.1 Motivation

The long and pragmatic tradition of man-made technology is to focus on stiff structures, whereas nature traditionally builds more flexible structures. Nature, especially the plant kingdom, resorts to stiff structures only in special situations, such as when the need arises to stay erect against gravity. Often, we can observe that twisting due to wind brings some branches of a tree closer to a downward orientation with many of the branches in a closer proximity to each other, thus reducing the tendency of the tree to bend over. The compromise between torsional and bending stiffness can be observed at a larger scale in bamboo culms [1] and banana petiole [2], and in a smaller scale, for instance, in sedges [3] and daffodil flowers [4]. The structural compliance of a plant and its organs are dependent on the flexural stiffness and torsional rigidity of the respective structures. Both the flexural and torsional stiffness of plant organs, such as the petiole and stem, are dependent on their geometry and constituent tissue (material) stiffness. This stiffness essentially depends on plants at each length scale, from cell to tissue. The structural properties of petioles and stems—as well as other plant organs—are correlated, among others, with their macrostructural shape, and size; microstructural properties of tissue, and cell wall construction.

Over the course of its life cycle, a plant may develop roots, stems, branches, leaves, and eventually flowers and fruits. These biological organs work in synergy to ensure the survival and reproduction of the organism. Within the shoot system of a plant, petioles and stems can be considered as multifunctional

organs that optimize structural and functional performance, such as bending resistance and nutrient transport. The petiole is an organ that attaches the leaf to the stem, whereas the primary function of the leaf is to harvest the light needed to drive the photosynthetic process, which is essential for the synthesis of organic compounds [5]. A petiole acts as a cantilever beam, holding their blades out, and must not bend easily. On the other hand, a petiole twists to permit the leaves to be clustered, which reduce their drag in a storm or under high wind. The overall geometry of a leaf petiole, the microstructure of the underlying tissues, and their hierarchical organization aids the petioles in stretching, bending, and twisting.

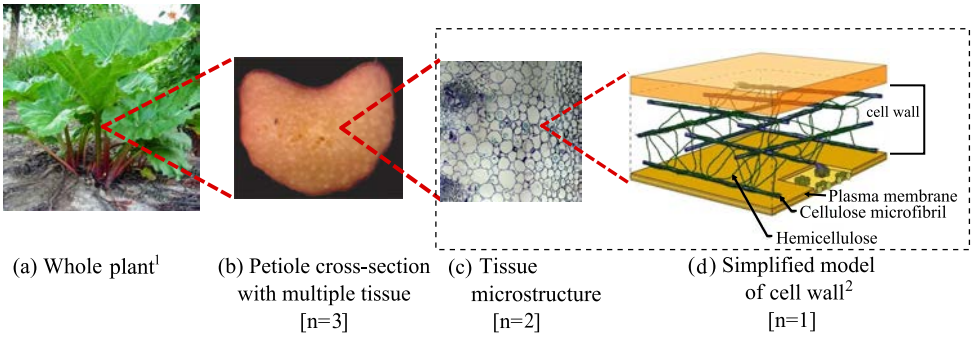

Figure 1–1: Multiscale hierarchic organization of a plant (*Rheum rhabarbarum*) petiole.

The petiole can be considered as a hierarchical cellular structure that has structural features defined at multiple length scales. The *Rheum rhabarbarum* petiole, as shown in Figure 1–1, exhibits structural hierarchies at multiple length scales ranging from a nanometer to a meter. The cell wall belongs to the first order of hierarchy ($n = 1$). The structural features at a smaller length

[1] ©2000 Rosie Lerner, Purdue University

[2] ©US Department of Energy Genome Programs/genomics.energy.gov

scale (below the first order of hierarchy) are not considered in the present hierarchical organization, because the continuum modeling approach will be inappropriate at this length scale. Therefore, the cell wall constituents are assumed to be shapeless at hierarchical order $n = 0$. The tissue stiffness at the second order of hierarchy, $n = 2$, is mostly controlled by the cellular microstructure. The heterogeneous cellular structure makes natural cellular solids comparatively more mechanically efficient than man-made engineered cellular materials [6]. The third order of hierarchy, $n = 3$, depicts the shape contour of the petiole. The cross-section of the petiole varies across species and may exhibit a longitudinal groove (for example, *Rheum rhabarbarum* petiole exhibits an semi-elliptical shaped top groove). The grooved non-circular shape elevates the structural flexibility to a greater extent than a circular cross-section.

To predict the overall mechanical properties (performance) of plant petioles and stems, a multiscale model capable of capturing structural properties at each length scale is required to model the overall mechanical properties (performance) of plant petioles and stems. Thus, mathematical formulations are required to model the structural properties at each order of hierarchy. The challenging tasks of the multiscale model of the petiole are to comprehend the structural properties at each order of hierarchy and to integrate the hierarchical structural properties to determine the overall mechanical properties. Thus, a successful integration of the anisotropic cell wall properties and micro-architecture of cellular tissue and its properties are necessary. To this end, a multiscale mechanical model that integrates hierarchical structural properties was developed through the present research to gain insight into the complete mechanical properties of the petiole. Nonetheless, the research on biomechanical characterization of petiole is conducted because structured

solids with torsional flexibility like petiole can be incorporated into boat mast, building, structure subjected to high wind, and wind turbine tower that can flex with wind. The multiscale mechanical model will elucidate the role of each order of structural hierarchy to determine the overall flexural and torsional stiffness of the petiole.

1.2 Goals of the Current Research

The goal of this doctoral research is to develop multiscale mathematical models to capture the overall mechanical properties of a petiole by correlating its hierarchical structural responses at different orders of hierarchy. The specific aim of the current research is to determine the flexural stiffness and the torsional rigidity of the petiole, where the properties are related to cell wall anisotropy, tissue microstructure, and cross-sectional morphology. The objectives of the current research are to:

1. Develop a mathematical model correlating the composite structure of the cell wall to obtain the stiffness of the cell wall.
2. Generate a non-periodic cellular network to realistically illustrate the tissue microstructure.
3. Conduct a finite element analysis to determine the effective/homogenized stiffness for the random (non-periodic) cellular microstructure.
4. Correlate the flexural and torsional stiffness of the petiole by considering its morphology and constituent tissue stiffness by way of the concept of shape transformers.
5. Validate experimentally the mathematical models.

1.3 Requirements of the Multiscale Mechanics Model

Since the petiole displays a hierarchical organization at multiple length scales, a multiscale model of a plant petiole requires a set of mathematical models that integrates plant biology with the quantitative approach of

engineering to explicitly model biomechanical properties through theory, computation, and experiments. A multiscale model for a natural hierarchic cellular structure should be able to provide a quantitative formulation, which allows a researcher to simulate and predict the mechanical/structural properties of the structure. Thus, a multiscale model should enable an integration of the interaction between the geometry and material properties within a hierarchy and between hierarchies, while also making precise and verifiable predictions.

The biomechanical model of a plant organ requires a systematic hierarchical approach as the organ displays hierarchical organization at multiple length scales. The systematic modeling approach integrates the biological sciences with the quantitative approaches of engineering to model the overall biomechanical properties of the plant organ. Hence, the determination of the mechanical properties at different orders of the structural hierarchy and their integration are important. The mechanical characterization of an individual hierarchical order is commonly found in literature. For example at the cell level, the structural properties of cell wall have been modeled based on the stiffness properties of the wall constituents and their compositions [7–9]. Other factors that govern the biological and structural properties of the plant tissues include the spatial distribution of cells and their size, and shape. In general, the mechanical properties of plant tissues have been mostly modeled without considering the actual cell distributions [10–12]. At the structural level, the geometric properties of the plant organ along with the material properties play a crucial role in determining mechanical properties—flexural stiffness and torsional flexibility [1, 13–15]. Although research on plants and plant-based materials on several level of the structural hierarchy has been carried out, the integration among the hierarchical outcomes to characterize the overall biomechanical properties is currently lacking. A multiscale model can, thus, contribute to

capture the properties at multiple orders of the structural hierarchy of the plant organ. The model requires being more comprehensive and allows to integrate the interaction between geometry and material properties within the hierarchical orders, while making precise and verifiable predictions. Hence, the proposed biomechanical research has the aim of elucidating the relationship between the structural properties of the petiole, its microstructures, and the mechanics at each level of the structural hierarchy of a leaf petiole.

The modeling of the structural properties of plants is challenging since the hierarchical orders of plants are observed in several scales, ranging from the subcellular level (nanometer) to the whole organism (meter). Hence, each order of hierarchy has to be quantitatively modeled to describe its biological processes. The multiscale model, comprising hierarchical mathematical models, should able to explicitly predict the biomechanical properties of the petiole. However, the multiscale model also reveals the general principles by exploring the mathematical models based on experimental observations. Therefore, a mathematical model should have the following characteristics: (1) it should be biologically based and explicit—the variables described in the model should have counterparts in the experimental data against which the model is calibrated, (2) it should be parametrized with biological data upon availability, (3) it should be developed in such a way that it can make key predictions that are experimentally verifiable, and (4) it should be able to make efficacious predictions that can be used to generate novel hypotheses [16].

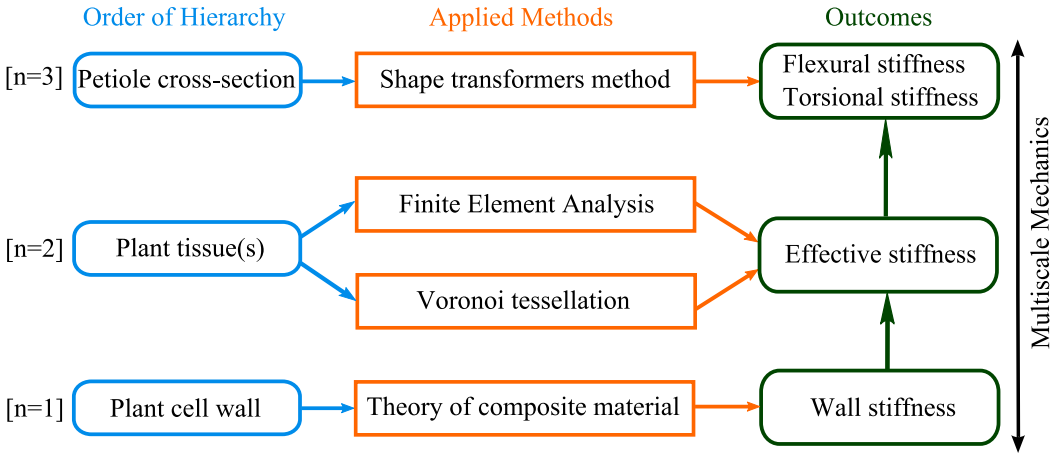

Figure 1–2: Hierarchical research approach.

Multiscale models usually are organized around two approaches—bottom up or top down, consisting of density functional theory (DFT), molecular dynamics (MD), dislocation dynamics (DD), cellular automata (CA), Monte Carlo, finite difference (FD), finite element (FE) and Fast Fourier transform (FFT). In this thesis, the former has been used. Figure 1–2 briefly illustrates the modeling approach used. The cell wall is modeled at the first order of hierarchy using the classical micro (*Voigt* and *Reuss*) and macromechanical theories of composite materials. Since plant tissues usually exhibit graded cellularity as well as complex heterogeneity, Voronoi tessellation has been chosen to capture the cellular distribution at the third order of hierarchy [17]. At this level of hierarchy, the virtual model coupled with wall stiffness (from the hierarchy below) undergoes a finite element analysis. However, the finite element analysis (FEA) applied to stochastically selected representative volume elements yields homogenized/effective tissue stiffness [12, 18–20]. At the top order of hierarchy, the petiole is modeled with the shape transformers method [21, 22] coupled with its effective tissue properties to obtain the compliant beam mechanical properties. Thus, the structural ability of the petiole to withstand a bending and twisting load depends on the stiffness properties of the cell wall, turgor

pressure, the microstructure of tissue and its stiffness properties, and the petiole's cross-sectional shape [23].

1.4 Outline of the Dissertation

Chapter 2 is a comprehensive literature survey delineating the related background works at each order of hierarchy. The literature review also provides insight into the need for the present research. The hierarchical modeling approaches are mainly presented in *Chapter 3* to *6*. In *Chapter 3*, the stiffness of the plant cell wall is modeled with respect to the first and second order of hierarchy. At the first order of hierarchy, the stiffness of the cell wall is mathematically modeled using the theory of a composite material. The engineering properties of the cell wall are modeled using micro and macromechanical theories of composite material at this order of hierarchy. Experimentally measured volume fractions of the constituents and fiber orientation angle of the cell wall of the model plant are used to approximate the cell wall stiffness.

Chapter 4 provides a geometrical modeling of plant tissues, which belong to the third order of hierarchy. Since the tissue microstructures exhibit gradient-based heterogeneity, Voronoi tessellation can capture these complex microstructures. The inherent drawback, semi-infinite edges at the boundary, makes the conventional Voronoi model unrealistic and restricts its use in FEA. Therefore, a novel algorithm, finite edge centroidal Voronoi tessellation (FECVT), was developed to realistically capture the microstructures. The FECVT algorithm was used to model a variety of plant tissues. The virtual models and their geometric and statistical characterizations are discussed in this chapter.

Chapter 5 analyzes the effective stiffness of tissues for the heterogeneous tissue microstructures, which belong to the third order of hierarchy. The finite

element analyses of the Voronoi models coupled with the cell wall properties provide the effective/homogenized stiffness. In addition to apparent tissue stiffness, the FEA also provides an insight into the effect of microstructural variations on tissue stiffness.

In the hierarchical organization of the present study, the cross-section of the petiole belongs to the fourth order of hierarchy. Thus, *Chapter 6* develops the flexural and torsional stiffness of the petiole by considering its shape morphology and constituent tissue properties. The flexural and torsional stiffness analyses describe the cumulative effect of the structural properties of the preceding hierarchies. The computed flexural and torsional stiffness also are compared with the experimental stiffness.

The organization of the thesis is shown in Figure 1–3:

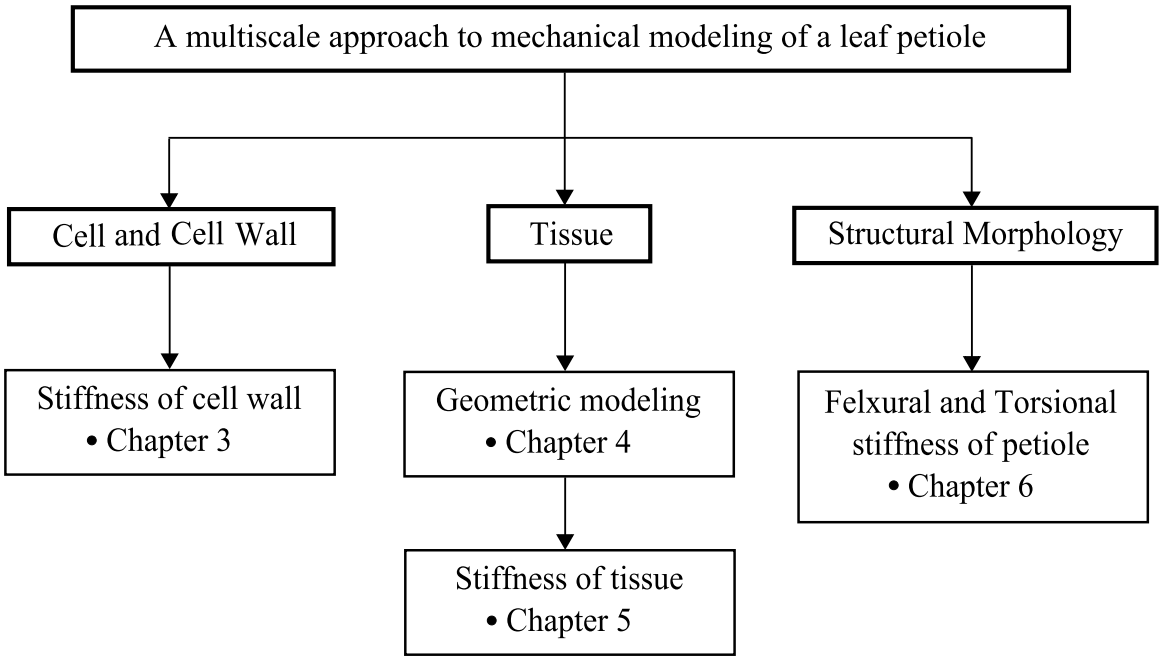

Figure 1–3: Thesis organization of chapters.

CHAPTER 2
Literature Review

2.1 Overview

The word *petiole* comes from the Latin word *petiolus*, which literally translates into "little foot". Evolutionary processes have shaped the morphology of petioles and other plant organs, and over generations natural selection has driven the evolution of efficient and structurally sound petioles. The petiole resembles a cantilever beam that supports the leaf against gravity, allowing for its exposure to the sun. Figure 2–1 shows the image of a plant with its leaf in an extended petiole. When exposed to wind, a petiole acts as a beam that resists the drag acting on the frontal area of the leaf. The petiole thus provides mechanical support against the weight of the leaf and against environmental factors such as rain and wind, resisting both bending and twisting loads [24].

2.2 Stiffness of Cell Wall

The structural properties of plant organs collectively depend on the geometry of their constituent cells, cell wall composition and the structural properties of the cell wall constituents. Cell walls are mainly composed of complex networks of polysaccharides, namely cellulose (C), hemicelluloses (HC) and pectin, along with comparatively minor quantities of structural protein and/or lignin [25–28]. Each Cellulose Microfibril (CMF) is a semi-crystalline aggregate of 36 β-1, 4-glucan chains. CMFs are several µm long but only about 3-4 nm thick and lay 15-30 µm apart in the wall [8]. The construction of the cell wall is considered to be a fiber-reinforced composite where the cellulose fibrils act as the main load-bearing elements [7, 29, 30]. The CMFs are embedded in a compliant matrix of hemicelluloses and lignin, where the

Figure 2–1: *Rheum rhabarbarum* (Rhubarb) whole plant in a garden.

stiffness of the matrix is approximately two orders of magnitude lower than the CMF [9, 27]. Experiments on plant cells also show that the properties of CMF strongly dictate the elasticity of the cell wall while, lignin and hemicelluloses have a marginal effect [31]. The stiffness of the cell wall can be approximated considering the simplest composite model, where the cell wall is a two phase system under uniaxial loading condition [32, 33]. Based on the elastic properties and the volume fractions of the CMF and lignin/hemicellulose or pectin/hemicelluloses matrix, the stiffness of the cell wall can be determined for two limiting architectures—parallel (*Voigt* model) and perpendicular fiber orientations (*Reuss* model)—with respect to loading direction. Due to a significant difference in stiffness between the polysaccharides at the cell wall level and other hierarchies, the orientation of the microfibrils in the cell wall influences the stiffness properties of individual cells and tissues as well. The Microfibril Angle (MFA) has been experimentally shown to be a key factor in determining the mechanical properties of a plant's cell walls [26–28, 30]. Hence,

the Voigt and Reuss models are insufficient to approximate the stiffness of the cell wall. To determine the longitudinal and transverse modulus, the orthotropic nature of the cell wall should be considered [34, 35]. However, the stiffness of the cell wall is highly species dependent since the cell wall composition and the MFA vary with the species [36–39]. An integrated modeling approach is necessary to approximate the wall stiffness of the species of interest. A stiffness bound for the cell wall can be estimated based on its constituent's properties and arrangements through the classical micro and macromechanical theories of composite materials. Based on the experimentally determined MFA, volume fractions, and Young's moduli of the wall constituents, the stiffness of the cell wall can be modeled assuming orthotropic material properties, where the constitutive relation yields the stiffness of the cell wall along the orthogonal directions. However, the effect of turgor pressure, another factor, which affects the apparent wall stiffness is not considered in this analysis.

2.3 Geometric Modeling of Plant Tissue

A plant organ is generally composed of an assembly of cellular tissues which make up its microstructure and essentially govern its physical properties. Each tissue has evolved to meet specific functional requirements that guarantee the plant's survival in a given environment. The way in which multiple tissues are geometrically tessellated within an organ helps determine mechanical performance and is important for achieving optimal structural support. It has been demonstrated that the shape, size, and spatial distribution of cells are among the main factors that govern the physical, biological and structural properties of a cellular material [22, 40]. Hence, the ability to realistically model the cellular microstructure of a plant tissue is crucial to understanding its mechanical behavior [41].

Cellular structures in plants may appear quasi-regular and periodic. For example, the microstructure of cork and balsa wood are almost as regular as honeycomb [10]. This type of structure can be modelled using a repeated unit cell with a given geometric shape. While important for analysing the microstructure of periodic cellular solids, this method cannot account for the structural variations and imperfections inherent to most natural cellular solids. An alternative technique, the Voronoi tessellation, can be used to generate an accurate representation of a non-periodic microstructure [11,12,42]. In previous works, however, the actual cellular distribution of a natural structure has not been considered when generating virtual models. In fact, the nucleation points of the Voronoi cells were generated randomly, with no realistic replication of the cellular tissue, thereby yielding a structure that differed significantly from the actual cell distribution of an actual plant tissue. Nevertheless, the structural analyses of these Voronoi models delineated the dependence of the mechanical properties on the randomness of non-periodic microstructures.

A Voronoi tessellation is a partition or tiling of a $d-$dimensional space into $d-$dimensional polyhedral cells. Such a technique has been applied in numerous fields including biology, meteorology, metallurgy, crystallography, forestry, ecology, geology, geography, computer science and engineering [43–45]. Because of its ability to capture the randomness of a cellular pattern, this technique can be applied to model a plant tissue with irregular cell shapes and sizes. Voronoi tessellation is used extensively to model grain geometry for the characterization of the properties of polycrystalline aggregates [46] and inter granular cracks [47]. Mattea [48] and Roudot [49] pioneered the use of Voronoi tessellation to model the microstructure of fruit tissues. However, neither group was able to generate a representative geometrical model that resembled the actual tissue micrograph. Both groups aimed only to capture the

randomness of the fruit tissue microstructure without necessarily producing a model that accurately represented the real tissue. Mebatsion [50] applied a Voronoi algorithm to model the parenchyma tissue of different apple cultivars. They developed virtual models using Centroid-based Voronoi Tessellation (CVT) and Poisson Voronoi Tessellation (PVT); the latter model bears a closer resemblance to the actual fruit parenchyma. However, the techniques are unable to differentiate between the actual cells and the extracellular spaces that are present in the fruit tissues. Moreover, the cells are more elliptical in fruit parenchyma compared to those in plant petiole and stems. Mebatsion *et al.* later developed a new modelling technique, the ellipse tessellation, which was able to generate a more accurate representation of the fruit parenchyma [50, 51].

The need to develop a realistic geometric model of plant tissue is crucial to understanding tissue mechanics, since certain mechanical properties are governed by the architecture and structural distribution of the tissues. Given that stem and petiole tissues are morphologically different from fruit parenchyma, Voronoi tessellation, specifically CVT, can be an appropriate modelling tool. In a recent publication, Ntenga *et al.* [52, 53] tried to analyse the structure, morphology, and mechanical properties of *Rhectophyllum camerunense* (RC) plant fiber using a conventional Voronoi diagram. Due to inherent drawbacks in the Voronoi (CVT) model, semi-infinite edges were present at the boundary of the fiber, making the model unsuitable for finite element analysis (FEA). To overcome this challenge, the authors developed a virtual model coupled with a java-based image-processing program, ImageJ. This method can be used to model an arrangement of cells bound by an irregular shape; however, one requirement for its application is that the edges at the sample boundary be reconstructed to obtain straight line edges.

The conventional CVT has the drawback of yielding semi-infinite edges at the fiber boundary. As a result, the mechanical response of a microstructure with an irregular shape contour is impossible to calculate. Therefore, the development of a comprehensive CVT-based technique for generating geometric models that possess finite edges at the sample boundary is of utmost importance for determining the stiffness properties of plant tissues [17]. From geometrical considerations, the Voronoi model is a good candidate to generate random microstructure since it provides planar boundaries, which separate the cells. As compared to other procedure such as using a micrograph of the cross-section into a finite element model, the major advantage of Voronoi modelling is the ability to generate a virtual tissue with a very large number of cells at a low computational cost.

2.4 Stiffness of Plant Tissue

Microstructural analysis of cellular solids is crucial to understanding their overall behavior since cellular solids are prevalent both in nature and in man-made engineering structures. Many researchers have modeled natural cellular solids using repeating unit cells to construct a regular microstructure in the form of circular, square or hexagonal arrays [54]. Closed-form relations of the structure-property can be derived using a simplified geometrical model based on repeated unit cells [10, 12]. However, modeling plant tissue is a challenging task, for its heterogeneity as natural cellular solid often exhibits non-periodic microstructures. Since the microstructure is heterogeneous in shape and size, the Voronoi tessellation technique is effective at capturing such irregular distribution of cell shapes. In addition, finite element analysis (FEA) of the geometric (Voronoi) model can be used to obtain the effective/apparent/homogenized stiffness properties of a real representation of the tissue.

Most studies on the homogenization of cellular solids are based on regular models with a periodic microstructure. However, real solid foams exhibit amorphous arrangements of pores with different sizes and shapes rather than perfectly periodic structures. The homogenized/apparent elastic property for periodic honeycomb varies from 10∼15% compared to non-periodic honeycomb [12]. To consider the microstructural irregularity, the Voronoi cell finite element method (VCFEM) was developed and coupled with asymptotic homogenization theory to generate a global homogenized elastic property [40]. This method only considers the local periodicity of the microstructure. To take into account the global periodicity in the irregular microstructures represented by the Voronoi tessellation, the homogenization process requires a large scale representative volume element (RVE). Analyses of such models had been provided, among others, by Silva *et al.* [11], Fazekas *et al.* [55], Roberts and Garboczi [56] for both two and three-dimensional models. Even a large scale RVE of a plant tissue having heterogeneous cellularity may not attribute to the respective tissue. Moreover, the large scale RVEs are inefficient in terms of computational effort. To overcome this limitation, instead of a large scale RVE, the computational homogenization technique can be applied to several small scale RVEs with non-periodic microstructures for global homogenization [57–59]. This stochastic approach is able to effectively consider the microstructural irregularity present in the plant tissues. For a given boundary condition, the finite element analysis of the 2D virtual tissue (RVE) provides the homogenized stiffness. The homogenized material property can thus be used in the next order of hierarchy to capture macro-scale mechanical properties—bending and torsional stiffness.

2.5 Flexural and Torsional Stiffness of Plant Petiole

The structure of the petiole adapts to meet multiple evolving requirements. Besides sustaining metabolic functions, the primary task of a petiole is to

(a) basal (b) middle (c) apical

Figure 2–2: Petiole cross-sections at different locations along the length.

provide structural support to the leaves of a plant. The petiole acts as a cantilever beam as it withstands the load of a large leaf blade and upholds the blade to maintain its exposure to the sun without bending against gravity. It helps clustering the leaves by twisting, which reduces drag in both frontal and total exposed area [14]. Along with the material properties, the geometric properties of the petiole play a crucial role in determining flexural stiffness and torsional flexibility. The twist-to-bend ratio is an index that has been used to examine the ability of living organisms to twist without bend [60–63]. Petioles with a top groove usually have higher twist-to-bend ratios than petioles without grooves. Figure 2–2 shows the cross-sections of roughly semi-elliptical shaped rhubarb petiole at different locations along the longitudinal axis. The petiole's cross-sectional shape can be captured using Gielis' superformula, which has demonstrated its capacity for a wide range of biological cross-sectional shapes [64]. This enables the accurate representation of natural forms and is used here to capture the last hierarchy of the petiole, i.e. the grooved contour.

Along with the shape morphology, the mechanical properties of a petiole depend on the series of integrated tissues; for instances, rhubarb petiole mainly consists of epidermis (bark), collenchyma, and parenchyma tissue. Each of these tissues is distinguishable in terms of its function and its material properties. The material and geometric properties of each tissue may play a role in governing the flexural stiffness and torsional rigidity of the whole petiole. The ability

of an organism to resist deformation by an imposed load depends on both the shape of its body and the mechanical properties of its tissues [65]. The effect of cross-sectional geometry on the mechanical properties of structures has been widely studied [66, 67]. Shape transformers [66] and shape factors [67] are two main criteria used to study this relationship. Using shape factors, the geometry of a cross section is compared with a square of the same area. Using shape transformers, the cross-sectional geometry is compared with a rectangle that envelops the given cross section. While shape factors depend on both the size and shape of a cross section, shape and size are decoupled when using shape transformers. Shape transformers, thus, might provide a more convenient approach for investigating the geometric effect of cross-sectional shape on the mechanical properties of a structure. Shape transformers were previously formulated for idealized pure geometric shapes [21, 66]. The Gielis parametrization of the Lamé curves [64] has been considered in the present analysis to redefine their formulation for the natural forms of biological organs and has been coupled with the shape transformers method [41]. This coupled approach is capable of capturing the overall macro-structural effect of layered architecture of the constituent tissues along with the petiole's natural shape morphology.

2.6 Summary

The analysis of the mechanical response of petiole requires the development of mathematical models and experiments that can describe the structural properties of a petiole at each order of hierarchy spanning from cell wall to whole petiole. The proposed research will address each order of hierarchy and will integrate the hierarchical outcomes to obtain the overall response of the plant petiole. The following points are addressed in this research:

- The stiffness of cell wall is approximated to a fibrous composite material to capture the anisotropic cell wall stiffness, whereas the cell wall is mostly considered to be isotropic in the earlier works.
- To capture the actual architecture and geometry of the cells in a tissue, a novel algorithm, Finite-Edge Centroidal Voronoi Tessellation (FECVT), is developed and implemented.
- Since a large scale RVE (virtual tissue) is computationally inefficient and may not capture the detail heterogeneity, a stochastic computational homogenization technique is realized in this work.
- Finally, the bending and torsional stiffness of the petiole are modeled considering the shape morphology, the stiffness of constituent tissues and cell wall, and the cell turgor pressure. Since such cumulative approach of modeling the macroscale mechanical response has not been addressed, the overall bending and torsional stiffness will provide an insight into the cumulative effect of the hierarchical structural properties.

CHAPTER 3
Cell Wall Stiffness

3.1 Overview

In this chapter, the stiffness of plant cell wall is modeled by relating two orders of structural hierarchy. At the sub-cellular level—the first order of hierarchy—the cell wall is modeled by considering the material as a fiber-reinforced composite. The stiffness of the parenchymal cell wall is approximated based on the composition of the wall constituents, their volume fractions and elastic properties. Additionally, to predict the elastic properties of the collenchymatous cell wall, the effect of the fiber orientation angle is taken into account. The stiffness of both the parenchyma and collenchyma cell wall will be used to determine the elastic properties of the respective tissues.

3.2 A Micromechanical Model of the Cell Wall Stiffness

The cell wall is considered as the building block of the first order of hierarchy as shown in Figure 1–1. Since the cell wall is considered to be a fiber-reinforced composite material, stiffness bounds can be obtained by considering the microfibril angle (MFA) and the volume fractions of the wall constituents, and their elastic properties. The upper and lower bounds of the stiffness of the cell wall can be approximated by using micromechanical models: the *Voigt* (*iso-strain*) and the *Reuss* (*iso-stress*) models. To use these models, three pieces of information are required: (i) the elastic moduli of the cell wall constituents, (ii) the volume fractions of the various constituents, and (iii) the geometric arrangements of the constituents relative to each other. The properties of the cell wall constituents are available in the literature. An earlier theoretical prediction of the Young's modulus provides relatively higher

values—246 and 319 GPa [68, 69]—whereas more recent analyses show 120–140 GPa [70–72] and 167 GPa [73] for crystalline cellulose along the fiber direction. Data for the elastic modulus of hemicelluloses are scarce and fall within a range of 5–8 GPa [74]. The elastic properties of lignin are difficult to assess and vary from 4 to 7 GPa [75, 76]. The constitutive properties of pectins also are scarce in the literature, and the stiffness vary between 1 to 4 GPa [77–80]. Along with the Young's modulus of 1 GPa for the pectins, a set of rational moduli [9] considered in this work are shown in Table 3–1.

Table 3–1: Elastic properties of cell wall constituents used in the present work [9].

Properties	CMF	Lignin	Hemicellulose
E (GPa)	134	2.0	2.0
G (GPa)	4.4	1.0	0.6
ν	0.1	0.2	0.3

The values shown in Table 3–1 are used in the Voigt and Reuss models to determine the wall stiffness along the fiber direction, E_1, and across the fiber direction, E_2 (Figure 3–1). The *Voigt upper bound* is

$$E_1 = E_f v_f + E_m v_m \tag{3.1a}$$

and the *Reuss lower bound* is

$$\frac{1}{E_2} = \frac{v_f}{E_f} + \frac{v_m}{E_m} \tag{3.1b}$$

where E_1 and E_2 refer to the Young's moduli of the composite; E_f and E_m refer to the Young's modulus of the fiber and matrix, respectively; v_f and v_m refer to the volume fraction of the fiber and matrix, respectively, with $v_f + v_m = 1$.

Using a similar micromechanical concept, the major Poisson's ratio ν_{12}, along the fiber direction is

$$\nu_{12} = \nu_f v_f + \nu_m (1 - v_f) \tag{3.2a}$$

and, the minor Poisson's ratio ν_{21}, across the fiber direction, can be derived with reciprocal relationship

$$\frac{\nu_{21}}{E_2} = \frac{\nu_{12}}{E_1} \tag{3.2b}$$

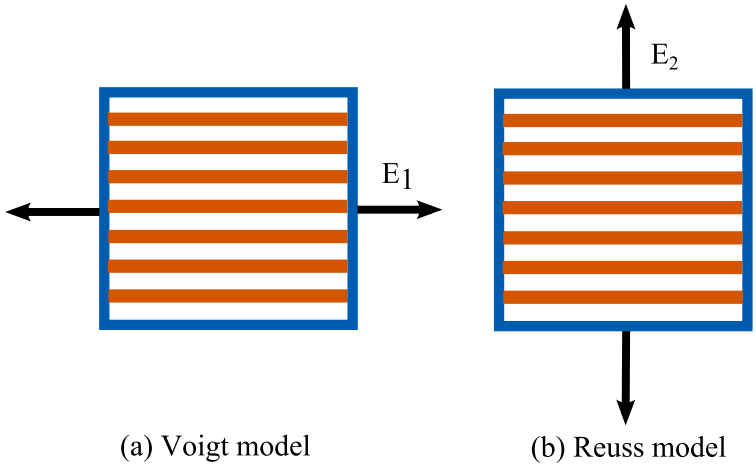

Figure 3–1: *Voigt* and *Reuss* model.

The in-plane shear modulus can be expressed as

$$G_{12} = \frac{G_m G_f}{G_f (1 - v_f) + G_m v_f} \tag{3.3}$$

An actual cell wall, however, may not behave according to the predictions based on either the pure Reuss or the pure Voigt model. Rather, a hybrid model appears to be the best modeling approach, although the Voigt elements appear to be dominant.

On the other hand, to predict the Young's modulus of the primary cell wall (E_{pcw}), considering a random or a biaxial fiber-reinforced composite material, the efficiency factor or Krenchel factor, η_θ, can be used with a rule

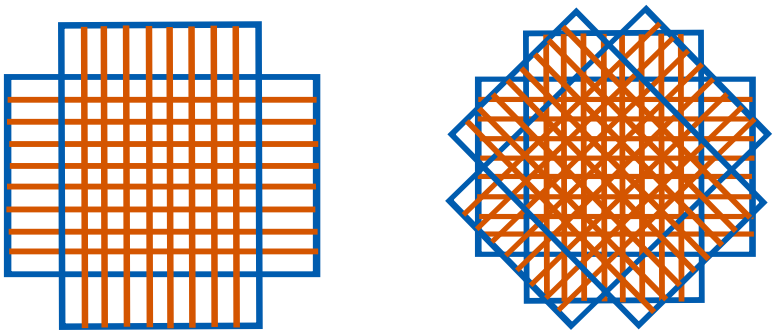

(a) $\eta_\theta = 0.5$ (b) $\eta_\theta = 0.375$

Figure 3–2: Bi-axial and multi-axial fiber matrix resulting in a composite material with a Krenchel factor (η_θ) of 0.5 and 0.375 respectively.

of mixture (ROM) that can capture the effect of fiber orientation on the cell wall stiffness [81–83]. For the biaxial and random fiber-reinforced composite, as shown in Figure 3–2, the Krenchel factor is $\eta_\theta = 0.5$ and $\eta_\theta = 0.375$, respectively, assuming the fibers are longer than the critical length of the fiber of that type. Therefore, the Young's modulus of the parenchyma cell wall can be expressed as

$$E_{pcw} = \eta_\theta E_f v_f + E_m v_m \tag{3.4}$$

3.3 Constitutive Properties of the Cell Wall using Macromechanics

The constitutive relation of the fiber (CMF) reinforced composite cell wall depicts the stiffness in the global coordinate system. For an orthotropic cell wall, the compliance matrix is expressed for plane stress conditions as

$$[S] = \begin{bmatrix} S_{11} & S_{12} & 0 \\ S_{12} & S_{22} & 0 \\ 0 & 0 & S_{66} \end{bmatrix} \tag{3.5}$$

where $S_{11} = \frac{1}{E_1}$, $S_{12} = -\frac{\nu_{21}}{E_2} = -\frac{\nu_{12}}{E_1} = S_{21}$, $S_{22} = \frac{1}{E_2}$, $S_{66} = \frac{1}{G_{12}}$
Therefore, the constitutive relation for an orthotropic material is

$$\{\epsilon\} = [S]\{\sigma\} \tag{3.6a}$$

$$\{\epsilon\} = [Q]^{-1}\{\sigma\} \tag{3.6b}$$

where $[Q]$ is the stiffness matrix, $[S]$ is the compliance matrix with $[S] = [Q]^{-1}$.

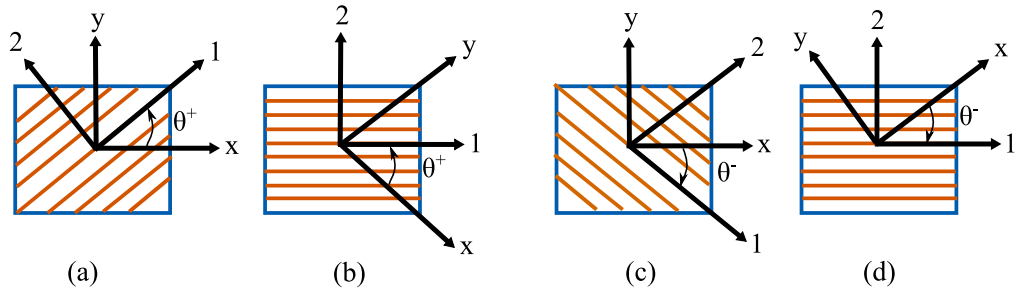

Figure 3–3: *On-axis* and *off-axis* configuration.

Equation (3.6) stands for the *on-axis* configuration, where the global coordinate system, the $x - y$ axis, coincides with the local coordinate system, the $1 - 2$ axis, respectively. When the local and global coordinates do not coincide, the arrangement is an *off-axis* configuration as shown in Figure 3–3. Therefore, the on-axis stress-strain relationship is not adequate for an analysis of an off-axis configuration. In the off-axis configuration, the stiffness depends on the fiber orientation angle, which is the MFA for the cell wall configuration. Thus, the MFA needs to be addressed in the constitutive relation. If the $x - y$ coordinate system is aligned with the direction of loading, and the $1 - 2$ coordinate system is aligned with the fibers, MFA, θ, is the angle between the two systems (Figure 3–3).

The local $(1-2)$ and global $(x-y)$ coordinate systems are related through a transformation equation. Hence, the transformation of strains between the

loading (local) direction and the fiber (global) direction is denoted by

$$\begin{Bmatrix} \epsilon_1 \\ \epsilon_2 \\ \epsilon_6 \end{Bmatrix} = \begin{bmatrix} m^2 & n^2 & mn \\ n^2 & m^2 & -mn \\ -2mn & 2mn & m^2 - n^2 \end{bmatrix} \begin{Bmatrix} \epsilon_x \\ \epsilon_y \\ \gamma_{xy} \end{Bmatrix} = [T_\epsilon] \begin{Bmatrix} \epsilon_x \\ \epsilon_y \\ \gamma_{xy} \end{Bmatrix} \tag{3.7}$$

where $m = cos\theta$, $m = sin\theta$ and $[T_\epsilon]$ is the strain transformation matrix. Similarly, the stress transformation matrix is

$$\begin{Bmatrix} \sigma_1 \\ \sigma_2 \\ \sigma_6 \end{Bmatrix} = \begin{bmatrix} m^2 & n^2 & 2mn \\ n^2 & m^2 & -2mn \\ -mn & mn & m^2 - n^2 \end{bmatrix} \begin{Bmatrix} \sigma_x \\ \sigma_y \\ \tau_{xy} \end{Bmatrix} = [T_\sigma] \begin{Bmatrix} \sigma_x \\ \sigma_y \\ \tau_{xy} \end{Bmatrix} \tag{3.8}$$

Rearranging and combining equations (3.6 to 3.8), the Cartesian strain-stress relationship in the global coordinate system is given by

$$\begin{Bmatrix} \epsilon_x \\ \epsilon_y \\ \epsilon_{xy} \end{Bmatrix} = [T_\epsilon]^{-1}[S][T_\sigma] \begin{Bmatrix} \sigma_x \\ \sigma_y \\ \tau_{xy} \end{Bmatrix} \tag{3.9a}$$

$$\Rightarrow \begin{Bmatrix} \epsilon_x \\ \epsilon_y \\ \epsilon_{xy} \end{Bmatrix} = [\bar{S}] \begin{Bmatrix} \sigma_x \\ \sigma_y \\ \tau_{xy} \end{Bmatrix} \tag{3.9b}$$

where $[\bar{S}]$ is a new matrix and known as the *transformed reduced compliance* matrix. The new compliance matrix represents an anisotropic constitutive relationship that has shear coupling terms. The off-axis constitutive relationship can be expressed in the following form:

$$\begin{Bmatrix} \epsilon_x \\ \epsilon_y \\ \gamma_{xy} \end{Bmatrix} = \begin{bmatrix} \bar{S}_{11} & \bar{S}_{12} & \bar{S}_{16} \\ \bar{S}_{12} & \bar{S}_{22} & \bar{S}_{26} \\ \bar{S}_{16} & \bar{S}_{26} & \bar{S}_{66} \end{bmatrix} \begin{Bmatrix} \sigma_x \\ \sigma_y \\ \tau_{xy} \end{Bmatrix} \tag{3.9c}$$

The elements of $[\bar{S}]$ are shown in Appendix A. In summary, the constitutive (engineering) properties of the cell wall are

$$E_x = \frac{E_1}{m^4 + \left(\frac{E_1}{G_{12}} - 2\nu_{12}\right) n^2 m^2 + \frac{E_1}{E_2} n^4} \tag{3.10a}$$

$$\nu_{xy} = \frac{\nu_{12}\left(n^4 + m^4\right) - \left(1 + \frac{E_1}{E_2} - \frac{E_1}{G_{12}}\right) n^2 m^2}{m^4 + \left(\frac{E_1}{G_{12}} - 2\nu_{12}\right) n^2 m^2 + \frac{E_1}{E_2} n^4} \tag{3.10b}$$

$$E_y = \frac{E_2}{m^4 + \left(\frac{E_2}{G_{12}} - 2\nu_{21}\right) n^2 m^2 \frac{E_2}{E_1} n^4} \tag{3.10c}$$

$$\nu_{yx} = \frac{\nu_{21}\left(n^4 + m^4\right) - \left(1 + \frac{E_2}{E_1} - \frac{E_2}{G_{12}}\right) n^2 m^2}{m^4 + \left(\frac{E_2}{G_{12}} - 2\nu_{12}\right) n^2 m^2 + \frac{E_2}{E_1} n^4} \tag{3.10d}$$

$$G_{xy} = \frac{G_{12}}{n^4 + m^4 + 2\left(2\frac{G_{12}}{E_1}\left(1 + 2\nu_{12}\right) + 2\frac{G_{12}}{E_2} - 1\right) n^2 m^2} \tag{3.10e}$$

3.4 Experiments on Model Plant (Rhubarb) and Results

Rheum rhabarbarum (rhubarb), commonly known as a vegetable, grows wild in central Asia and often is cultivated in the western and north-western provinces of China, in Tibet and in Europe and North America. Although fresh rhubarb is usually available from early winter through early summer, winter rhubarb is commercially produced in green houses in the northern United States and Canada. Rhubarb can be naturally grown as an annual in subtropical and tropical climates that have a cool production period. In these environments, the usual average spring temperatures during the day are $\sim 24\,^{\circ}\mathrm{C}$ and $10\,^{\circ}\mathrm{C}$ to $12.8\,^{\circ}\mathrm{C}$ at night; the average summer temperature is below $\sim 32\,^{\circ}\mathrm{C}$. Rhubarb is a hardy, perennial, dicotyledonous plant that grows from a bulbous rhizome, forms thick and long leaf stalks (petioles) that bear heart-shaped large leaves

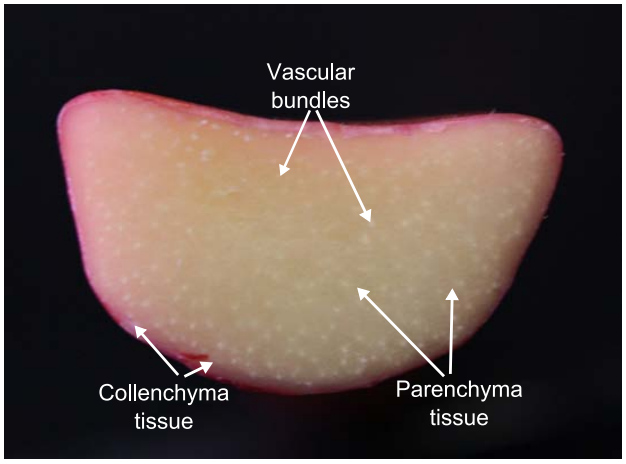

Figure 3–4: Photograph of a cross-section of rhubarb petiole with constituent tissues.

of up to $1m^2$ in size (Figure 2–1). The typical size of the rhubarb plant varies from 3 to 5 feet in height, or even more, and 3 to 4 feet in diameter. Generally, the fleshy petiole is slender with a length of up to 18 inches and $1-2$ inches in diameter. However, the width (diameter) of investigated rhubarb petioles ranged between 0.55 and 1.2 inch ($14 \sim 30.5$ mm). The petiole cross-section is solid with a roughly semi-elliptical grooved shape [66, 84, 85]. The rhubarb plant is chosen as the model plant because the petioles of the rhubarb plant carry large leaf blades and have longitudinal top groove, which assists the structural flexibility than the circular cross-sectional shape.

Fresh Rhubarb petioles were imported from leading international fruit and vegetable suppliers—"The Greenary" in Barendrecht, Netherlands and "Dragonberry Produce" in Clackamas, OR, USA. The petioles were stored at $4\,^{\circ}$C in plastic bags to prevent decay and dehydration during shipping so to preserve their freshness. A photograph of a cross-section of rhubarb petiole with different tissues is shown in Figure 3–4.

3.4.1 Experimental Measurement of Cell Wall Thickness

Deparaffinised rhubarb sections on slides were mounted on SEM stubs using carbon tape, and sputter coated with gold (Au). The sections were imaged using a JEOL JSM-7400F High Resolution Field Emission Scanning Electron Microscope (Figure 3–5).

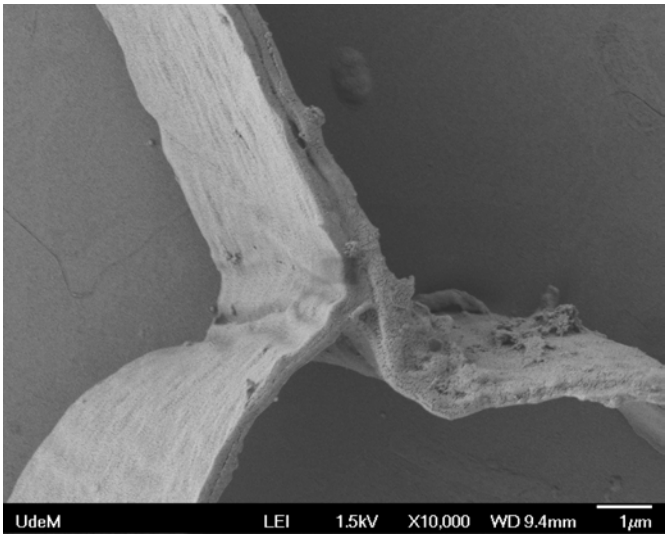

Figure 3–5: Scanning electron micrograph of parenchymal cell wall.

The scanning electron micrographs were acquired for three different rhubabrb petioles and include a total of 21 sample locations. To approximate the thickness of the parenchymal cell wall, 5 to 35 images were taken from the sample locations. The wall thickness was measured from the scanning electron micrographs using ImageJ64, a Java-based image processing program, which supports standards image processing functions including edge detection, contrast manipulation, smoothing and others. For each location, a sample mean (thickness) has been computed. The means of the pooled data are statistically analyzed to approximate an average cell wall thickness (the pooled mean wall thickness). About 95.45% of the values lie within two standard deviations of the pooled mean. However, 2 of the 21 sample means are not reflected

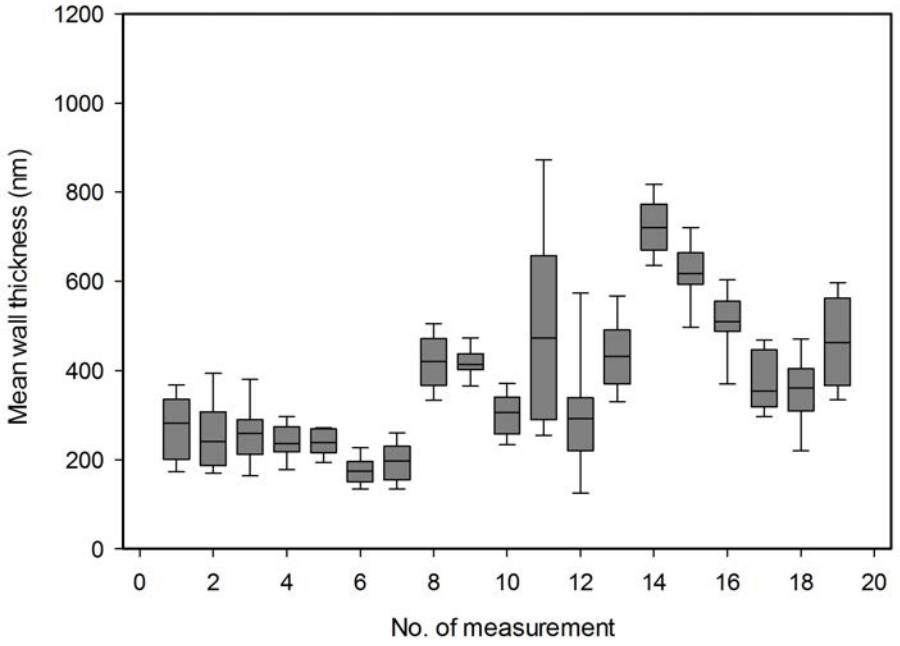

Figure 3–6: Distribution of the mean parenchymal cell wall thickness.

in the subsequent calculation, since they are considered to be outliers (i.e., an observation that lies an abnormal distance from other values in a random sample from a population). The sample means of a 95% confidence interval level are shown in Figure 3–6.

To calculate a single/equivalent mean value, the principle of pooled variance has been used. The pooled variance is used to estimate the variance given in several populations taken in different circumstances. A set of formulas used to calculate the pooled parameters is given in Appendix B. By using the principle, the pooled standard deviation and mean cell wall thickness have been calculated. The estimated mean parenchymal wall thickness is

Pooled mean cell wall thickness = 367.323 (SD 112.006) nm.

3.4.2 Measurement of Cell Radius using Light Microscopy

Rectangular pieces of tissue, measuring $\sim 5 \times 5 \times 5$ mm, were cut out of the rhubarb petioles and fixed in formaldehyde: acetic acid : alcohol (FAA).

These fixed tissues were subsequently dehydrated in ethanol and embedded in Paraplast Plus [86]. Samples were cut into 8-µm sections and stained with 0.05% toluidine blue O (TBO) in sodium citrate. Images were acquired with a Leica DM6000B microscope using OPENLAB, a modular imaging software used for fluorescence imaging. Individual sections were imaged at multiple points, and the images were digitally stitched together to form composite micrographs using Adobe Photoshop®.

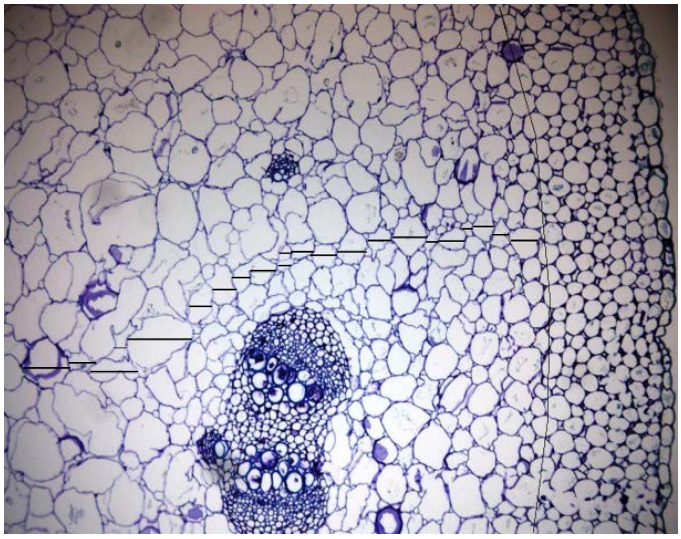

Figure 3–7: Measurement of cell radii from the micrograph of a rhubarb tissue sample. A vertical line arbitrarily separates the parenchyma from the collenchyma, and horizontal lines represent the location of cells that were measured.

By using the similar principle of pooled variance, the pooled standard deviation and mean cell wall thickness have been calculated. The estimated mean parenchymal wall thickness is

$$\text{Pooled mean parenchyma cell radius} = 72.75 \text{ (SD } 28.22) \text{ µm}$$

3.5 Computational Results and Discussion

The computational results are obtained based on the mathematical models along with the experimental measurements of cell dimensions. The results are discussed in the following subsections.

3.5.1 Constitutive Properties of Collenchyma Cell Wall

The properties of the collenchyma cell wall depend on the wall constituents, mainly cellulose microfibril, hemicellulose, and lignin. The CMF, embedded in a pliant lignin/hemicellulose matrix, acts as the load bearing element that controls the wall properties. In addition to the elastic properties of these cell wall constituents (shown in Table 3-1), the volume fractions of the constituents play an important role as well. The volume fractions of the constituents are not homogeneous throughout a multi-layered cell wall. Usually, the layered construction is evident in woody plants, but it is also observed in many other non-woody plants. Although the number of layers depends on several factors, such as the types of species and cells, the cell wall is widely accepted to be considered as a three-layered structure. In fact, the woody plants typically exhibit three secondary layers plus a primary layer and middle lamellae. The primary layer only plays a significant role in the early stage of a growing plant and in the parenchymal cell. When a plant cell reaches maturity, the secondary wall becomes the determinant that governs its mechanical performance. The volume fractions of CMF, lignin, and hemicelluloses as shown in Table 3–2 represent the values of a typical set of multilayered plant cell walls. Nevertheless, the composition of the constituents depends on several factors as well, such as the types of species and cells, the location of the cells, and the age of a plant.

Table 3–2: Approximate volume fractions of tracheid cell wall [68].

Cell wall layer	CMF (%)	Lignin (%)	Hemicellulose (%)
S_1	28	45	27
S_2	45	20	35
S_3	47	15	38

The data shown in Tables 3–1 and 3–2 have been used to compute the effective engineering properties, such as stiffness and Poisson's ratio, of the cell wall. The variations of stiffness with respect to MFA along different layers are shown in Figures 3–8(a) to 3–8(c). Figure 3–8(a) depicts the effect of MFA on the longitudinal Young's modulus for each layer. Up to 40°, the effect of MFA on the longitudinal wall stiffness is substantial, and the stiffness is reduced to a considerable amount. In contrast, the transverse stiffness is nearly invariant with the MFA up to 50° as shown in Figure 3–8(b). Beyond this limit, the transverse modulus varies with MFA and increases with increasing MFA. The shear modulus is maximum for CMF equal to 45° in the loading direction(Figure 3–8[c]). However, the variation of shear modulus up to 20° is less significant, and a gradual increase is observed until the MFA reaches 45° and starts decreasing afterwards. The Poisson's ratios shown in Figures 3–9(a) and 3–9(b) vary with the MFA. The major Poisson's ratio increases rapidly up to MFA of 20° compared to the minor Poisson's ratio. The major Poisson's ratio plays an important role in controlling the anisotropic cell wall properties.

It is evident that the MFA plays a significant role in the cell wall stiffness, an observation that has been experimentally detected in the cell walls of numerous plants [37, 87–89]. MFA usually varies between 0 to 40° in the S_2 layer [37,87,90] and plays a leading role in determining the overall wall stiffness. Moreover, since the thickness of the S_2 layer is generally much thicker than that of the S_1 and S_3 layers, the measurement of MFA for the whole cell wall, or the average MFA across the cell wall, involves the approximation of MFA in the S2 layer. Therefore, the S_2 layer is often the main determinant of the stiffness of the plant [91]. This concept is used to determine the effective engineering properties of a single layered dicotyledonous cell. Although a more accurate

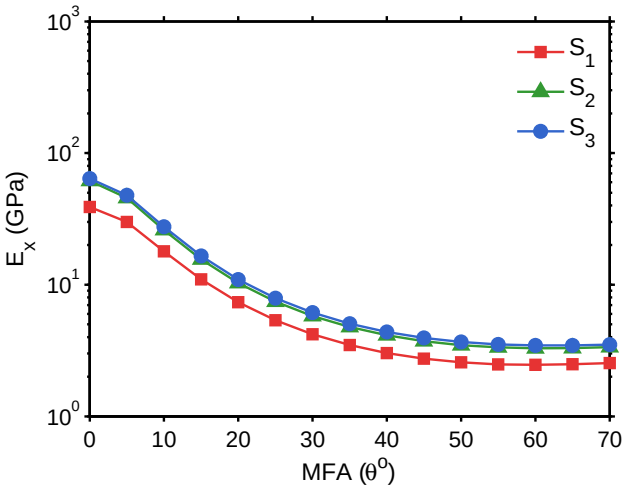

(a) Longitudinal stiffness

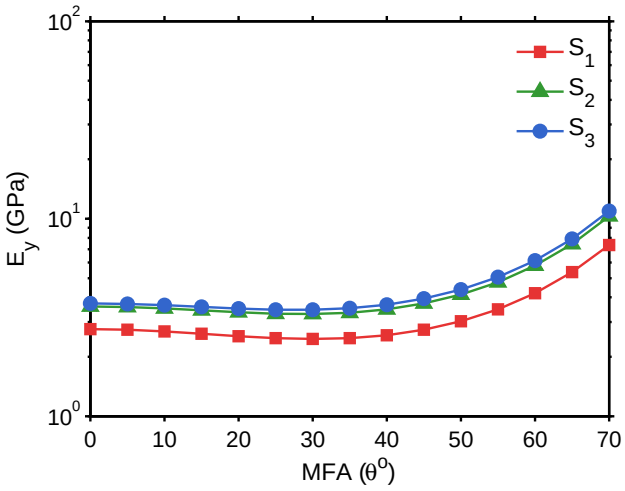

(b) Transverse stiffness

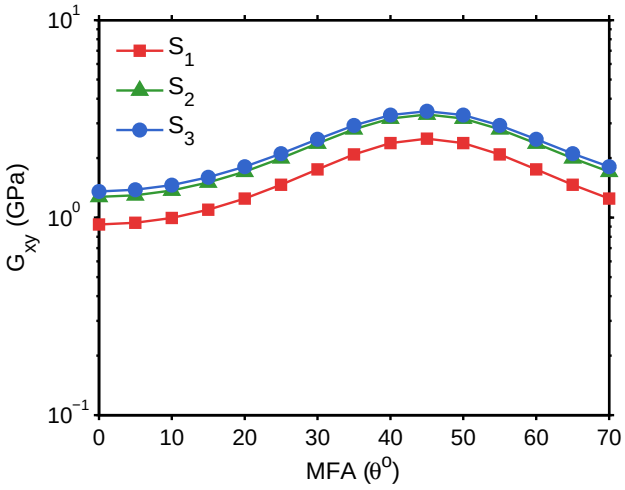

(c) Shear modulus

Figure 3–8: Stiffness properties of different cell wall layers for varying MFA.

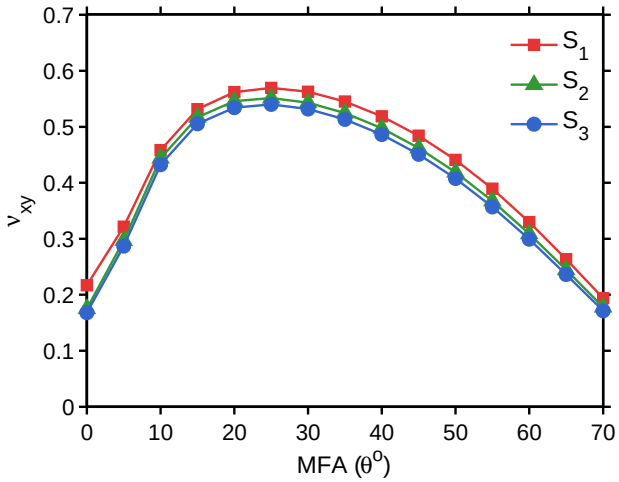

(a) Major Poisson's ratio

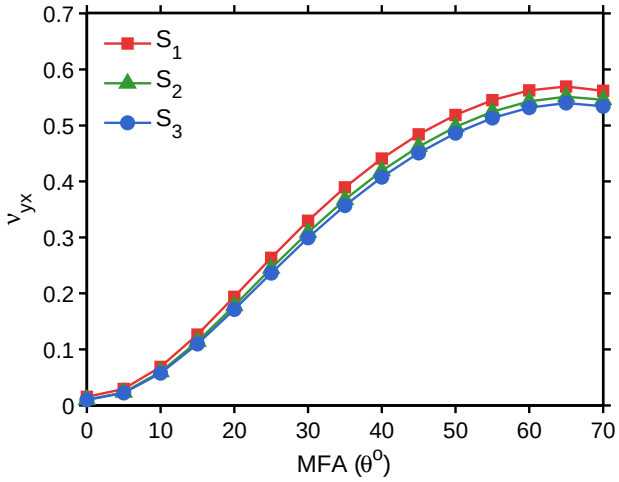

(b) Minor Poisson's ratio

Figure 3–9: Poisson's ratio of different cell wall layers for varying MFA.

and rigorous analysis would be conceivable by considering microfibril angles at different layers, the composition of the S_2 layer with respective MFA provides a good approximation of the overall stiffness of the collenchyma cell wall. Also, the measurement of MFAs in different layers is not always experimentally possible.

Typically, the collenchyma tissue in petioles and stems is observed in peripheral locations beneath the epidermal layer (Figure 3–4). As per experimental measurements, the collenchyma tissue typically comprises 20% of

cellulose and 80% of the HC/lignin matrix [92,93]. Although no clear distinction exists, the collenchyma cell walls can be considered to be a secondary cell wall [92, 94], where the orientation of CMF is mostly found to be inclined to the longitudinal axis [95–100]. However, the MFA also varies with respect to the measuring technique used. For dicotyledonous plants, the MFA usually lies between $6^\circ \sim 25^\circ$ [101]. Based on the fiber volume fraction and MFA, the stiffness properties of the collenchyma cell wall can be computed. The stiffness properties of the collenchyma cell wall with 20° MFA are summarized in Table 3–3. The elastic properties of the collenchyma cell wall will be used to predict the respective tissue stiffness.

Table 3–3: Stiffness properties of collenchyma cell wall determined via Equation 3.10.

	E_x (GPA)	E_y (GPA)	G_{xy} (GPA)	ν_{xy}	ν_{yx}
Cell wall	8.405	2.503	1.467	0.3872	0.1183

3.5.2 Elastic Properties of Cell Wall

Thin walled parenchyma cells make up the bulk of most non-woody plants. The parenchymal cell wall is mainly the primary cell wall composed of cellulose microfibril embedded in a hemicellulose/pectin matrix. The constituent composition of the primary cell wall differs from the secondary cell wall. Earlier analyses showed that the typical primary plant cell wall is composed of $9 - 25\%$ CMF and an interpenetrating matrix of $25 - 50\%$ hemicelluloses, $10 - 35\%$ pectins, and 510% structural proteins [102–104]. Weibel has shown that roughly 40% cellulose, 30% hemicelluloses, and 30% pectins are present in the parenchymal cells of sugar beet pulp in one of his patents [105]. Later, Vorwerk and his coworkers approximated the constituent composition of the primary cell wall of dicotyledonous plants to be 30% cellulose,

30% hemicelluloses, 35% pectin, and $1-5\%$ structural proteins on a dry weight basis [106]. Hence, the primary cell wall is plainly characterized by relatively less CMF and greater pectin compared to the secondary walls. The pectins content are especially found to be more in the primary cell walls of the dicotyledonous plants. The primary cell walls of dicotyledonous plants typically contain $25-35\%$ cellulose, 50% or more pectin, and a remainder of xyloglucan and other hemicelluloses [25,107,108]. In the primary cell walls of the celery (*Apium graveolens L.*) parenchyma cells, Thimm *et al.* found 43% CMF, 51% pectin, and 6% hemicelluloses [109]. A more recent analysis revealed that the primary cell wall is composed of $15-40\%$ CMF, $30-50\%$ pectic polysaccharides, and $10-20\%$ hemicelluloses and other structural proteins [110]. The primary cell walls of all higher plants appear to contain the same general polysaccharides, albeit sometimes in very different proportions.

The primary cell wall grows, elongates and provides mechanical support for the plant by being rigid and stiff. This conflicting characteristic of the primary cell wall originates from the arrangement of the cellulose microfibrils. The orientation of the CMFs often is dispersed in the primary cell wall, but may show varying degrees of alignment because of cell elongation [111–115]. Wardrop showed that the orientation of CMFs altered from a transverse to longitudinal direction, relative to the cell axis, from the inner part to the outer part of the primary cell wall of the macerated tracheids of Pinus radiate [115]. According to Wardrop, the CMFs originally were deposited in the transverse direction to the cell axis, and during cell enlargement, their orientation passively shifts to the longitudinal direction. Later, Wardrop [116] and Harada and Cote [117] proposed a model for the primary cell wall that consisted of loosely aggregated CMFs, which were oriented more or less transversely in the inner part and longitudinally in the outer part of the cell wall. A similar variation in the

orientation of CMFs is observed during the formation of the primary cell walls in Pinus densiflora [113]. Later, Abe *et al.* reported that the newly deposited CMFs on the innermost surface of the primary cell walls of *Abies sachalinensis* are random, and their arrangements vary during the differentiation [111]. The predominant orientation of the CMFs altered from the transverse to longitudinal direction of the cell axis [111,112,118]. Nonetheless, recent analyses have found that CMFs initially are oriented transverse to the direction of growth of the inner face of the primary cell wall; however, as the wall expands, the CMFs tend to reorient. Yet, the distribution of CMFs, integrated across the thickness of the expanded cell wall, becomes nearly random [119–121]. Figure 3–10 shows both random and bi-directional orientation of CMFs in the primary cell wall of different plants.

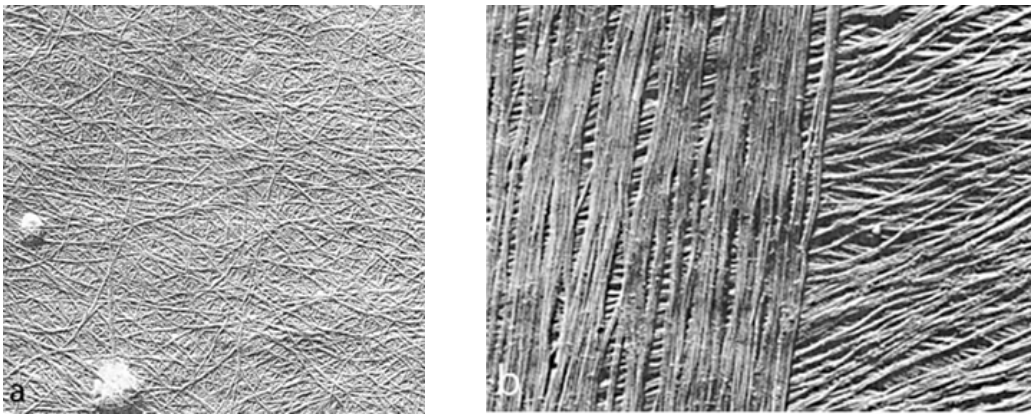

(a) (b)

Figure 3–10: (a) Primary wall of a fiber from the xylem of angiosperm showing the arrangement of cellulose microfibrils. Magnification ×21900. (b) Cell wall from the alga *Cladophora prolifera* showing different orientations of cellulose microfibrils in adjacent wall lamellae. Magnification ×15230. (Adapted from Frei-Preston [122]).

If the orientation of deposited CMFs does not change during the cell expansion, the CMFs of the mature primary cell wall should be oriented approximately transversely in the inner part and longitudinally in the outer

part with respect to the cell axis. Hence, an inference can be made from the experimental evidence and various cell growth models that the stiffness of the fiber-reinforced primary cell wall can be approximated as isotropic. In the present work, the hypothesis of random orientation of CMFs is adopted to determine the stiffness of the parenchyma cell wall. Nevertheless, the cell growth is ignored, since the parenchyma cell wall is assumed mature in the current mathematical model.

In this work, to predict the stiffness of the parenchyma cell wall, the volume fractions of the wall constituents are considered to be 30% CMF, 60% pectin, and 10% hemicelluloses. To compute the theoretical Young's modulus using Equation (3.4), the stiffness values shown in Table 3–1 are used along with the modulus of stiffness of 1 GPa for the pectins. The predicted composite stiffness of the parenchyma cell wall is

$$E_{pcw} = 15.8\,\text{GPa}$$

$$G_{pcw} = 6.1\,\text{GPa}$$

The typical values of computed stiffness fall between 150 MPa and 71.4 GPa, a range given by Vincent [123]. However, the stiffness of the parenchymal cell is affected by the water content and varies with the turgor pressure, as described in the following section.

3.6 Summary

This chapter has focused on the constitutive properties of the plant cell wall by considering the first order of hierarchy. At this hierarchical order, the constitutive properties of cell walls have been computed considering the constituents, and their compositions and organization. The upper and lower bounds of stiffness of the collenchyma cell wall are approximated by using the classical micromechanical models of Voigt and Reuss. Since the thick collenchyma cell wall resembles the secondary wall, the microfibril angle and

the stiffness bounds at the sub-cellular level have been used to compute the effective stiffness of the collenchymatous cell wall. On the other hand, the thin primary cell wall of the parenchyma tissue have been modeled for isotropic stiffness since the experimental evidence often exhibits biaxial or random fiber orientation in the respective cell wall. We have computed the stiffness of the parenchymal cell wall by using the rule of mixture associated with the Krenchel (efficiency) factor for random fiber orientation. However, the stiffness of the walls might differ significantly from the actual wall stiffness of the model plant rhubarb since the constitutive values are computed based on the generic composition of the dicotyledonous plant cell wall. Therefore, if the volume fractions and MFA of the model plant were determined experimentally, the computational stiffness would be more representative and closer to the actual wall stiffness. Further, the model used in the present work is simplified since it has ignored the presence of multi-layers. Despite these limitations, the approach is able to approximate the theoretical stiffness of the collenchyma and parenchyma cell walls. It would have been more appropriate to have wall stiffness values obtained via experiments. However, due to the limitation of our current experimental facility, we could not conduct the experiments at the cell wall level. Furthermore, the experimental data of wall stiffness are also scarce in literature and not available for rhubarb.

CHAPTER 4
Geometric Modeling

4.1 Overview

In this chapter, the geometric modeling of cellular plant tissues is considered. The geometric model aids to capture the contribution of tissue microstructure, which influences the structural behaviour and mechanics of biological beams, such as leaf petioles and stems. To represent the microstructure of tissue via simulations, a novel computational method, namely Finite-Edge Centroidal Voronoi Tessellation (FECVT), is developed and coded in MATLAB. The technique presented in this chapter might serve as a generalized way of modelling plant microstructures. The algorithm is applied to a variety of plant tissues, including *Arabidopsis thaliana*, *Philodendron melinonii* and *Rheum rhabarbarum* (rhubarb), to generate geometric models. The chapter mainly encompasses the description of plants, image acquisition techniques, the concept of Voronoi tessellation, and the FECVT algorithm. The outcomes and limitations of the proposed method are also discussed. The results obtained for *Arabidopsis* and *P. melinonii* via this method satisfactorily obey the geometric, statistical, and topological laws of naturally evolved cellular solids [17]. However, in this chapter, the results have been discussed in detail for rhubarb tissues, which equally satisfy all the empirical laws.

4.2 Growth Condition, Sample Preparation and Image Acquisition

The virtual geometric models are generated for three distinct plants, *Arabidopsis*, *Philodendron melinonii*, and *Rheum rhabarbarum* (rhubarb). As mentioned in Chapter 3, rhubarb is a hardy, perennial, dicotyledonous plant that grows from a bulbous rhizome, forms thick and long leaf stalks (petioles),

bearing heart-shaped large leaves of up to 1 m^2 in size (shown in Figure 2–1). The fleshy petiole is generally slender with a length of up to 18 inches long and $1-2$ inches of diameter Small slices of petiole were fixed in FAA, dehydrated and embedded in Paraplast Plus as described by Ruzin [86]. These were cut into 8 μm sections and stained with 0.05% toluidine blue O in sodium citrate. Images were acquired with a Leica DM6000B microscope using OPENLAB as shown in Figure 4–1. To obtain high resolution images, micrographs of individual sections were digitally stitched together to form composite images using Adobe Photoshop®.

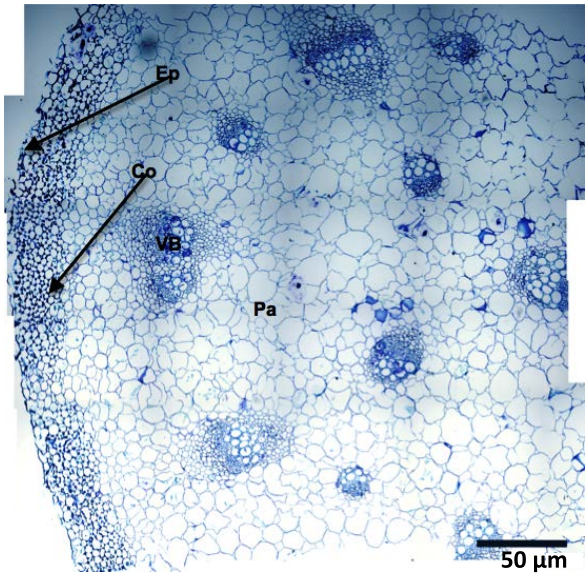

Figure 4–1: Paraffin-embedded rhubarb petiole cross-section stained with TBO and imaged with light microscopy at 20x magnifications. approximately 16 photos were stitched together to create this composite image. **Ep**-epithelium, **Co**-collenchyma cells, **VB**-vascular bundle, **Pa**-parenchyma cells are visible. Scale bar = 50 µm.

Arabidopsis thaliana as shown in Figure 4–2(a) is a flowering plant that has become very popular as a model organism in genetics and molecular biology [124]. It is a terrestrial plant, whose primary inflorescence stem grows to a height of about 30 cm. The small size, brief life cycle and high fertility

of *Arabidopsis* make it amenable to rapid and large-scale experimentation. Furthermore, the availability of thousands of mutant lines makes it relatively trivial to grow plants that display subtle micro-architectural differences.

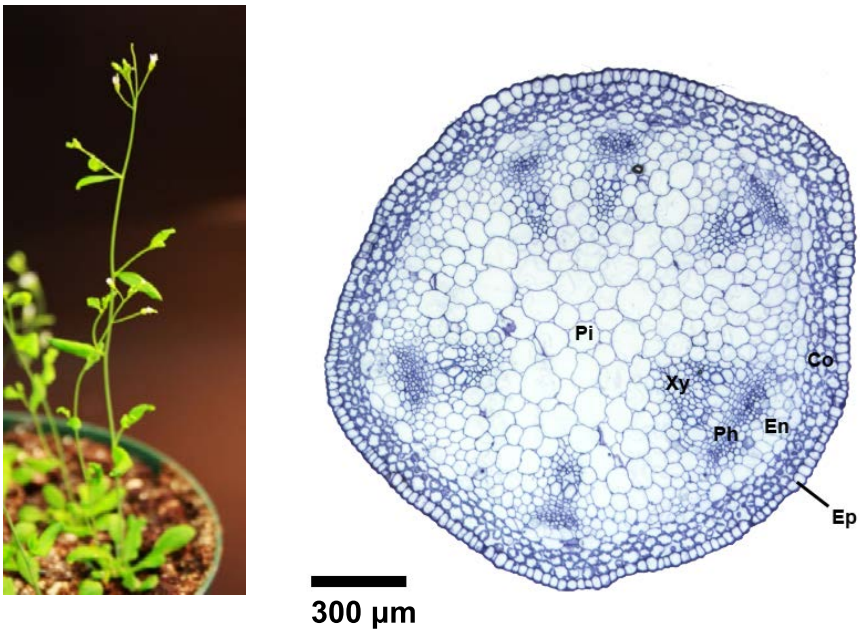

Figure 4–2: (a) Maturing *Arabidopsis thaliana* plant, (b) Micrograph of transversely sectioned *Arabidopsis* stem stained with toluidine blue. **Ep**-epidermis, **Co**-cortex, **En**-endodermis, **Ph**-phloem, **Xy**-xylem and **Pi**-pith are visible. Scale bar = 300 µm.

Arabidopsis thaliana seeds were planted on solid AT media [125] and stratified at 4 °C for $2-5$ days. They were grown at 22 °C under continuous light before being transplanted onto soil after $7-10$ days. Stem segments were harvested at $\sim$ 5 weeks. Short segments from below the shoot apical meristem were fixed in 0.5% glutaraldehyde, dehydrated and embedded in Spurr's resin as described in Western *et al.* [126]. These were cut into 1000 *nm* sections which were then stained with 1% toluidine blue O in 1% sodium borate. Sections were imaged as shown in Figure 4–2(b).

Philodendron melinonii is a relatively rare tropical plant that is substantially larger in size, with petioles measuring up to $1m$ in length (Figure

(a)

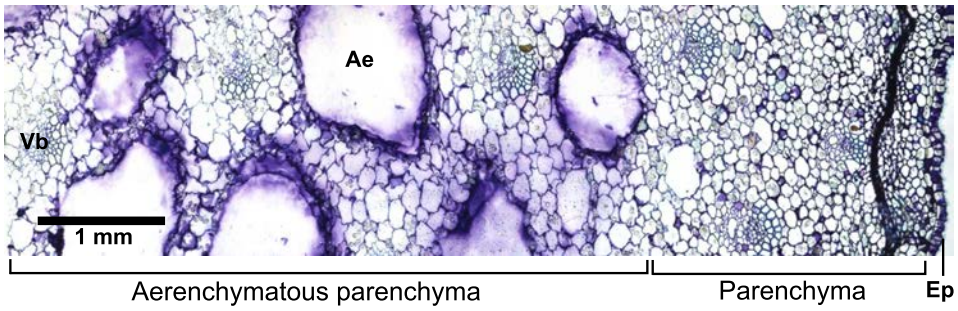

(b)

Figure 4–3: (a). Adult *Philodendron melinonii* plant, (b) Micrograph of transversely sectioned *P. melinonii* petiole stained with toluidine blue. Aerenchyma (Ae) and vascular bundles (Vb) are visible, as are three tissue layers: epidermis (Ep), parenchyma and aerenchymatous parenchyma. Scale bar = 1 mm.

4–3[a]). These petioles must support large, heavy leaves against physical stresses like wind and precipitation. Aside from being lightweight and very stiff, *P. melinonii* petioles display two unusual structural adaptations: an aerenchymatous core and a broad, flat groove along the apical surface (Figure 4–3b). Aerenchymatous tissues are normally found in the roots of aquatic plants, where they aid in gas exchange. In their study of two related species, Hejnowicz and Barthlott [127] reason that aerenchymae such as these primarily serve a structural role, reducing the density and energetic cost of these large

petioles. The apical groove, meanwhile, gives the petiole a peculiar D-shaped cross-section which may contribute to its mechanical anisotropy. We examine these two species, whose cellular structures are very dissimilar, to demonstrate the broad applicability of FECVT in tissue modeling.

Fresh *Philodendron melinonii* petioles were collected from the Montreal Botanical Garden. Small slices of petiole were fixed in FAA, dehydrated and embedded in Paraplast Plus as described by Ruzin [86]. These were cut into 8 μm sections and stained with 0.05% toluidine blue O in sodium citrate. Sections were imaged and shown in Figure 4–3(b).

4.3 Voronoi Tessellation

Given two points p_1 and p_2, their Voronoi regions in the plane are the two regions on either side of the perpendicular bisector of the line segment joining p_1 and p_2 (Figure 4–4[a]). This bisector is the boundary edge of the Voronoi region. A Voronoi microstructure is constructed based on a set of randomly generated points called Voronoi sites. The cell boundaries are drawn such that any point within the enclosed polygon is closer to its Voronoi site than to the Voronoi sites of the surrounding polygons. The Voronoi tessellation thus divides a space into as many regions as there are Voronoi sites (Figure 4–4[b]). Usually in a two-dimensional space, two methods are used to generate a Voronoi diagram. One is known as PVT, where points are randomly distributed in space according to the Poisson point process. The second one is the CVT, where the centroids of the cells are used to construct the Voronoi diagram.

In a CVT, the associated generating points are centroids (centre of mass with respect to a given density function) of the corresponding Voronoi cells. For a given domain $D \subseteq R^N$ and a density function $\rho(x)$ defined for $x \in D$,

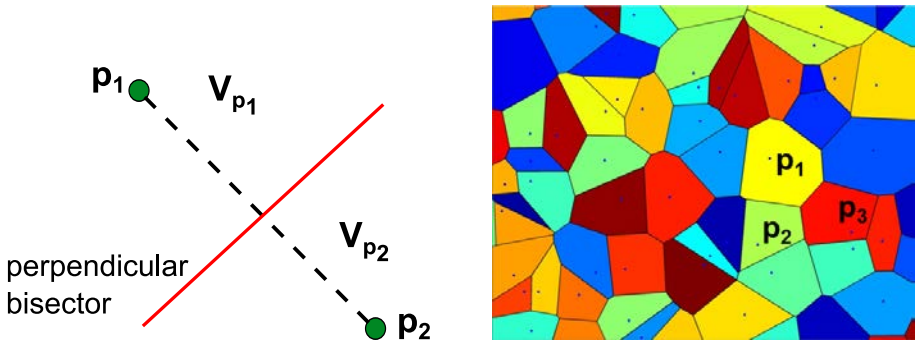

(a) (b)

Figure 4–4: (a) Schematic illustrating the creation of two Voronoi domains through the perpendicular bisector (solid line) of the line segments joining p_1 and p_2. (b) 2D Voronoi region generated for 50 randomly generated Voronoi sites [17].

the center of mass or centroid z_c of D is given by

$$z_c = \frac{\int_D x\rho(x)dx}{\int_D \rho(x)dx} \tag{4.1}$$

If an object has uniform density, its centre of mass is the same as the centroid of its shape. When the centroids of the cells and Voronoi sites coincide, the resulting diagram is called CVT.

4.4 Generation of a Conventional CVT

To generate a conventional CVT from an image or a micrograph, several steps are required to follow. The steps are discussed in this section. The steps are also included in the FECVT algorithm.

4.4.1 Image Segmentation

To model the microstructure, we need to calculate the centroids of the cells present in a micrograph. This begins with the segmentation of a colour micrograph of plant tissue. Segmentation refers to the process of partitioning a digital image into multiple segments [128]. The goal of this process is to simplify both the representation of an image and its analysis. It helps to distinguish the cells and the cell boundaries from the background. The simplest method for

image segmentation is known as "thresholding". Based on an optimum threshold value, thresholding converts a colour or greyscale image into a binary (black and white) image. Thresholding is performed here using Otsu's method [129], a well-known algorithm for global thresholding. The interclass variance of black and white pixels of the binary image is minimized to compute a global threshold value, which is a normalized value between 0 and 1.

4.4.2 Edge Detection

Since plant tissue microstructures exhibit graded cellularity as well as complex heterogeneity, thresholding is not sufficient to identify the cells in a micrograph. An edge detection algorithm is used in conjunction with thresholding to obtain the cellular distribution accurately. The Canny edge detection algorithm, which uses the double thresholding, is applied here because it can detect true but weak edges [130]. In this algorithm, the noise is first removed to smooth the image. Next, the edge detector finds the image gradient to highlight regions with spatial derivatives. The regions are tracked and the pixel that is not at the maximum is suppressed. The gradient array is then reduced by hysteresis, which is used to trace the remaining pixels that have not been suppressed. The hysteresis uses two thresholds and is set to zero (non-edge) if the magnitude is below the first threshold. The edge is created if the magnitude is above the high threshold. However, if the magnitude is between the two thresholds, it is set to zero unless there is a path from this pixel to a pixel with a gradient above higher threshold. As a result, the shape of the cell can be detected more precisely.

4.4.3 Calculation of Centroids

The calculation of centroids depends on the *Region of Interest* [131], a region of non-zero pixel value, which is 1 for a binary image. Based on X and Y coordinates of the pixels, the centroids of the cells are obtained calculating

the 1st order moments of the cells are computed. Since we are working with a digital image, the moment equation is modified into following algebraic form

$$m_{pq} = \sum_{i=1}^{n_1} \sum_{j=1}^{n_2} X_i^p Y_j^q f(i,j) \tag{4.2}$$

where (X_i, Y_j) is the coordinate of the i,j th pixel, $f(i,j)$ have value 1 if the i,j th pixel is in the shape and 0 otherwise. Considering the region of interest, which is completely enclosed in a rectangular region G of size n_1 by n_2 pixels, i varies from 1 to n_1 and j varies from 1 to n_2 in the function $f(i,j)$. For a 2D region, $p+q$ denotes the order of moment, where p and q are integers. Hence, the coordinates of the centroid of a cell are

$$\bar{X} = \frac{m_{10}}{m_{00}} \quad \text{and} \quad \bar{Y} = \frac{m_{01}}{m_{00}} \tag{4.3}$$

where the zeroth moment, physically, is equal to the area of the region.

4.4.4 Generation of CVT

After determining the centroids of the cells, which are the Voronoi sites, by drawing the cell boundaries such that any point within the enclosed polygon is closer to its centroid that to the centroids of the surrounding Voronoi cells. The outcome is a CVT (Figure 4–5) with semi-infinite edges at the boundary. Furthermore, while there may be a clear boundary in the micrograph, there is no specific boundary in the corresponding Voronoi model. The semi-infinite edges complicate finite element analysis because the boundary conditions, applied at an infinite distance, are not realistic. This problem is especially difficult to correct in models with irregular shape contour.

4.5 Finite Edge Centroidal Voronoi Tessellation (FECVT)

Conventional CVT is not sufficient to represent a microstructure with an arbitrary shape contour. To remove the infinite edges from the boundary, the centroids of the outermost cells should be determined. For each centroid, the

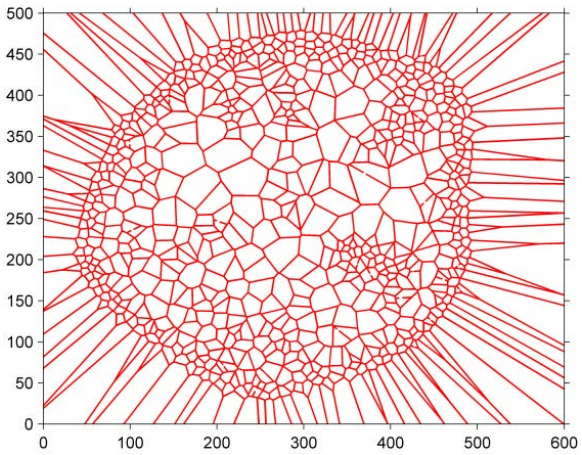

Figure 4–5: *Arabidopsis* stem modeled with the conventional Voronoi tessellation. The unrealistic semi-infinite edges appearing at the boundary of the figure are a limitation of this method [17].

distances between the centroid and the surrounding Voronoi sites (centroids of the surrounding polygons) are calculated and the minimum distance is determined. An imaginary point is created such that the distance between itself and the centroid is half of the minimum distance. The imaginary point is thus created for each of the selected centroid. The purpose of generating the imaginary points is to create a boundary using Quick hull algorithm [132]. The Quick hull algorithm is an algorithm for computing the convex hull of a set of points in two or more dimensions. If a finite planer set of points is given, the convex set of minimum area, which contains the original set, is known as the convex hull. In computational geometry, especially in computer graphics and image processing, the set usually consists of points (in two or higher dimensions). In two dimensions (2D), a convex hull is the minimal polygon that encloses all the given points. Based on the set of imaginary points and the convex hull algorithm, a boundary is imposed, after which a Boolean subtraction is realized. With this Boolean operation, the semi-infinite edges are truncated and the vertices of the truncated edges are reconnected to form the final boundary. Hence, the semi-infinite edges are removed, and straight line edges are obtained

to create cell boundaries. The Finite Edge Centroidal Voronoi Tessellation (FECVT) technique is thus capable of representing the microstructure of an image with an arbitrarily shaped or a rectangular boundary contour, as shown in Figures 4–6 and 4–7, respectively.

4.6 Computational Results

The FECVT method is applied to replicate the *Arabidopsis*, *P. melinonii*, and rhubarb tissues. *Arabidopsis*, a dicotyledon, displays a complex stem structure consisting of several tissue layers (Figure 4–2[b]). The core of the stem is composed of pith, a foam-like tissue composed of large, thin-walled parenchyma cells. Surrounding this core is a ring of fibrous xylem and interfascicular fibers, which functions as the stem's main structural support. Outside this layer lie the phloem, the endodermis and a thick layer of cortical cells. An epidermal monolayer then surrounds the entire stem. Although six types of tissues were identified, the cross-section of the inflorescence stem of *Arabidopsis thaliana* displays mainly three layers of tissues. The outer layer consists of epidermis (Ep), cortex (Co), primary phloem (Ph), middle layer comprises of primary xylem (Xy) and interfascicular fiber tissue (if any), and the inner layer represents pith (Pi). These layers of tissues are used to define stem's micro-architecture and response to mechanical perturbation [41]. This microstructure is modelled using the FECVT method (Figure 4–6). The FECVT model represents the stem realistically, in the sense, capturing the geometry of the cellular tissues.

P. melinonii, a monocotyledon, displays relatively simple structural organization (Figure 4–3[b]). The interior of the petiole is composed almost entirely of parenchyma cells. There is a steady gradation in cell size, with the outermost cells being the smallest and the innermost cells being the largest. Vascular bundles, which contain stiff xylem cells, are scattered randomly

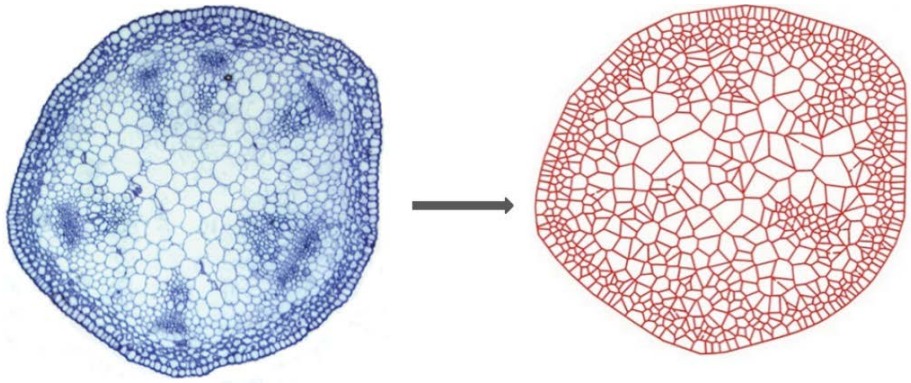

Figure 4–6: FECVT model of the entire cross-section of *Arabidopsis* stem [17].

throughout this parenchymatous tissue. Once again, an epidermal monolayer surrounds the entire structure. An FECVT model of a *P. melinonii* petiole is shown in Figure 4–7.

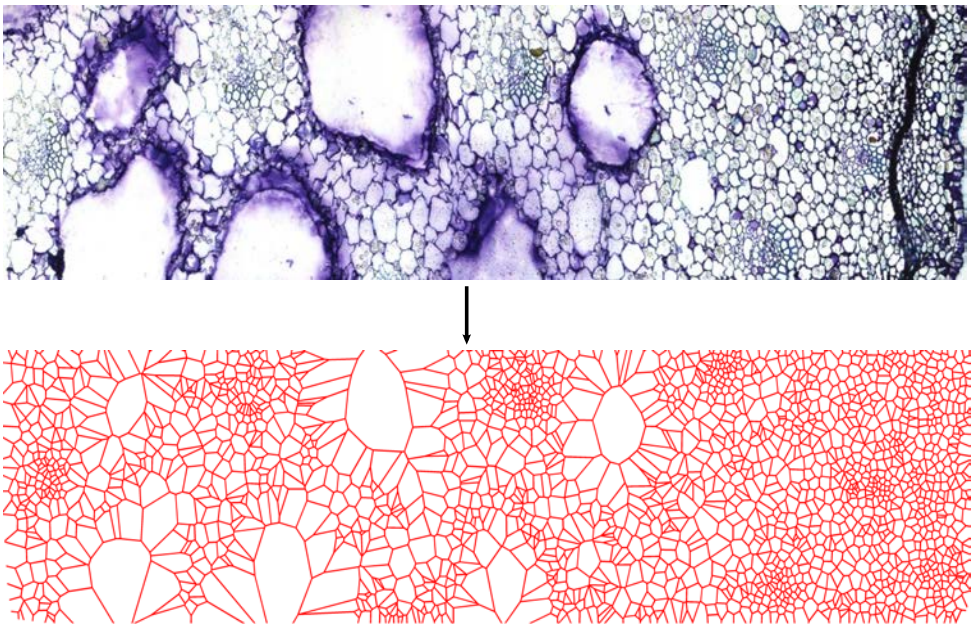

Figure 4–7: FECVT model of a portion of the cross-section extracted from a *P. melinonii* petiole [17].

The tissue of the *Rheum rhabarbarum* petiole, as shown in Figure 4–2(b), consists of a parenchymatous core surrounded by several layers of parenchyma cells and an epidermal layer. The parenchymal tissue has cellulose cells and fills the space between the dermal and the vascular bundles. The vascular bundles

consisting of xylem, phloem and cambial tissues are pervaded throughout the parenchyma tissue fairly evenly. The dermal system consists of a stiff and strong layer, which encloses all the core tissues. This layer is known as bark. In between bark and parenchymal tissue, the other structural tissue collenchyma consisting of thick but relatively flexible cell walls is present [66, 84]. The FECVT models of different rhubarb (petiole) tissues are shown in Figures 4–8 to 4–10. The geometric models are generated for the collenchyma, parenchyma and both the collenchyma-parenchyma (col-par) tissue, respectively. Since experimental data are used to formulate the mathematical model, the accuracy of the model appears to depend on the quality of the micrograph. The FECVT method, thus, can capture the detail of cellular distribution if the micrograph of the tissue microstructure is vivid and clear. However, the polygons at the boundary of a FECVT model may differ in shape and size from the boundary polygons of a conventional CVT.

The application of the Canny edge detection algorithm significantly enhances the accuracy of detecting the cell boundaries. In the previous works [50,53], the tissue microstructures were less complex in terms of variation of cell shape, and size and did not display an intense cellular gradient. On the other hand, the microstructures examined in this work are highly non-periodic and heterogeneous (Figures 4–1, 4–2[b], and 4–3[b]), displaying remarkable cellular gradients. In the virtual geometric models as shown in Figures 4–8 to 4–10, the FECVT method shows its ability to capture this complex heterogeneity and the graded cellularity. However, the linear interpolation between the points results in straight edge Voronoi cell boundary, whereas the actual cell boundary may contain curve edges. The simplification is accepted, because the length scale of the cells is much smaller than that of the whole petiole.

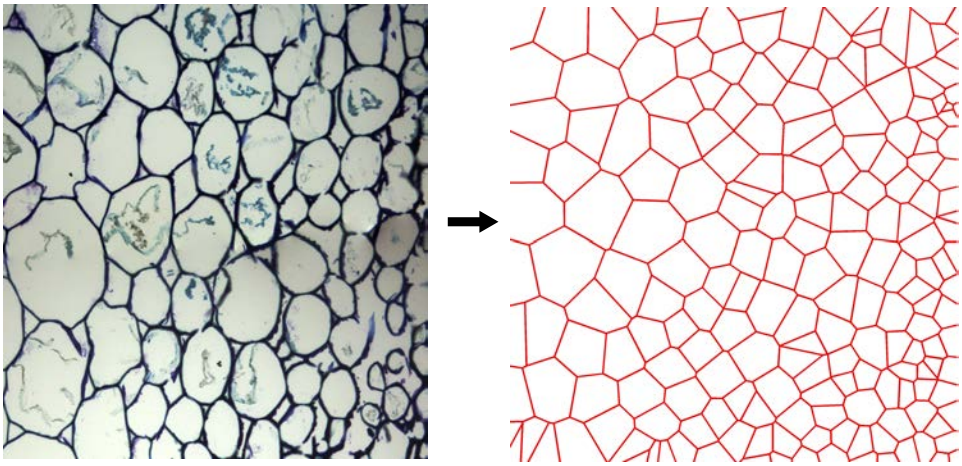

Figure 4–8: FECVT model of collenchyma tissue of rhubarb petiole [18].

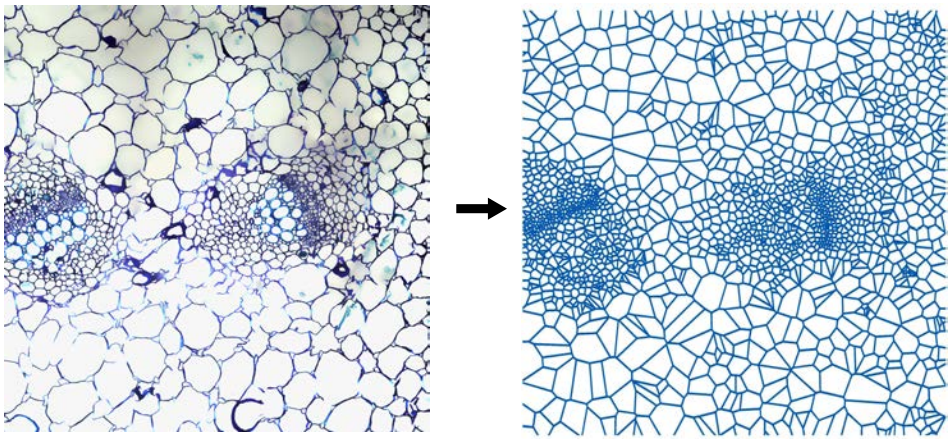

Figure 4–9: FECVT model of parenchyma tissue of rhubarb petiole.

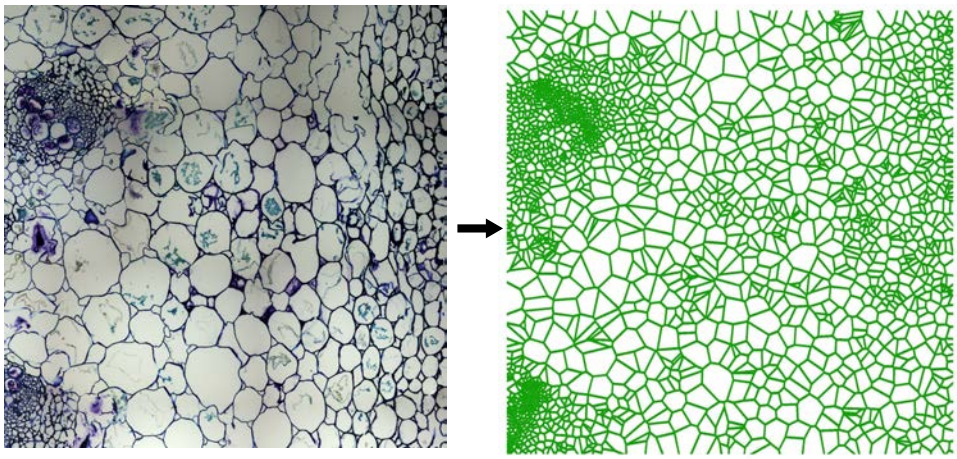

Figure 4–10: FECVT model of combined collenchyma-parenchyma tissue of rhubarb petiole.

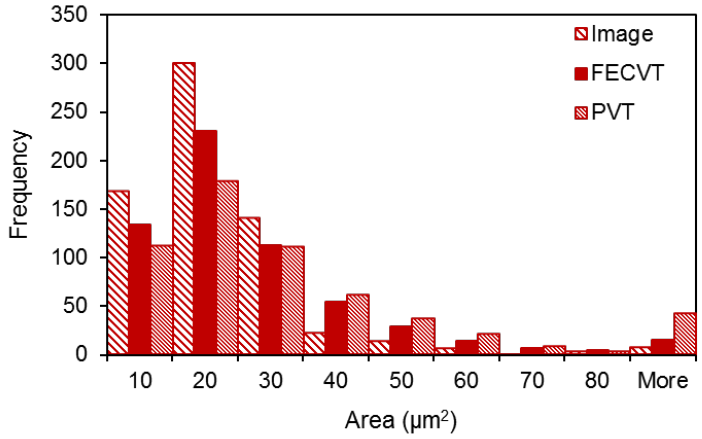

(a) Collenchyma tissue

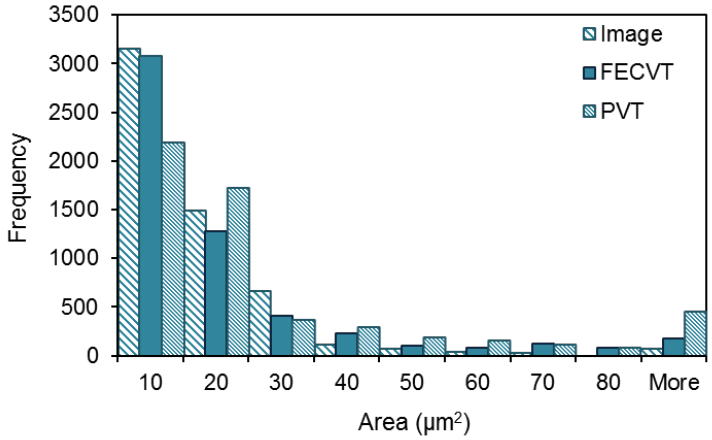

(b) Parenchyma tissue

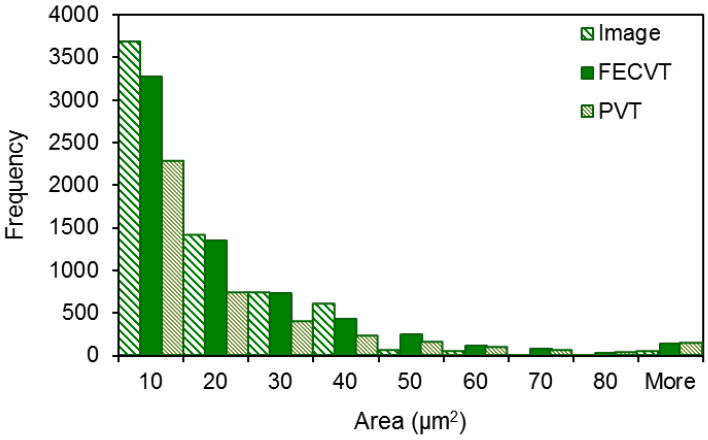

(c) Collenchyma-parenchyma tissue

Figure 4–11: Cellular area distribution of *Rheum rhabarbarum* tissue images and corresponding FECVT and PVT models of collenchyma (a), parenchyma (b) and collenchyma-parenchyma tissue (c).

Table 4–1: ANOVA for FECVT models of collenchyma tissue.

Col FECVT	Sum of Squares	df	Mean Square	F	Sig.
Between Groups	0.655	2	0.327	0.174	0.840
Within Groups	1147.104	611	1.877		
Total	1147.759	613			

Table 4–2: ANOVA for FECVT models of parenchyma tissue.

Par FECVT	Sum of Squares	df	Mean Square	F	Sig.
Between Groups	4.458	4	1.114	0.572	0.683
Within Groups	8452.119	4337	1.949		
Total	8456.577	4341			

Table 4–3: ANOVA for FECVT model of collenchyma-parenchyma tissue.

Col-Par FECVT	Sum of Squares	df	Mean Square	F	Sig.
Between Groups	0.623	2	0.623	0.331	0.565
Within Groups	7723.589	4105	1.882		
Total	7724.212	4106			

FECVT models are generated for several arbitrary chosen sections of different types of tissues. For each of the tissue microstructures, $3-5$ sections are chosen to generate the FECVT models. Each section is representative of the respective tissue type. Nonetheless, A one-way ANOVA is used to test the difference among the FECVT models generated for collenchyma, parenchyma, and combined collenchyma-parenchyma (col-par) tissues and shown in Tables 4–1 to 4–3, respectively. The first column in the ANOVA tables corresponds to the between-groups, and within-groups estimate of variance, which are shown in the fourth column, showing the mean square. The second column gives the sum of squares for each of the estimates of the variance. The third column gives the degrees of freedom (df) for each estimate of the variance. The number

of FECVT models and the sum of the Voronoi cells in the models are used to calculate the degrees of freedom between-groups and within-groups, respectively. The fifth column, F, corresponds to the ratio of the variance of between-groups and within-groups, shown in the preceding column. The last column gives the probability of significance of the F ratio, i.e., p value. Since, the p value is greater than the significance level ($\alpha = 0.05$), the null hypothesis is not rejected. It is evident from Table 4–1 that the FECVT models of the collenchyma tissue sections statistically do not differ significantly across the models as determined by one-way ANOVA ($F(2, 611) = 0.172, p = 0.837 > 0.05$). Similarly, for both the parenchyma and whole tissue, there are no statistically significant differences among the respective FECVT models (Table 4–2 and 4–3). The output of the ANOVA test, thus, implies that the FECVT models of the stochastically chosen tissue sections are statistically invariant; hence each model can be considered to be a representative volume element for the FEA.

4.7 Discussion

The virtual models of the tissues generated by the FECVT method should manifest the characteristics of naturally evolved cellular solids. Therefore, the FECVT models should conform to a number of geometric, statistical, and topological laws. The FECVT models of *Arabidopsis* and *P. melinonii* tissues satisfactorily obey these laws [17]. The characterization of the FECVT models of the rhubarb tissues based on the empirical laws have been discussed in this section.

The statistical characteristics are shown in Figures 4–11 to 4–15. In Figure 4–11, both the original micrographs and the virtual models, (i.e., FECVT and PVT models), are considered, whereas in the other figures, the characteristics are shown only for the virtual models. The cell areas of the *Rheum rhabarbarum* tissues are determined using the image micrographs, and the area distributions

are used to validate the FECVT models. In the original micrographs, the cell areas are calculated using digital image processing based on the pixel information. The cell areas from the different images and their corresponding FECVT and PVT models are statistically compared in Figure 4–11. It is reflected in this figure that the variations of cell area distributions of the FECVT and PVT models are subtle. The cell area distributions for both the models conform to the distributions of the corresponding image area. By contrast, in a conventional Voronoi model with semi-infinite edges, the areas of the virtual cells differ significantly with respect to the original images since the boundary cell areas are large due to semi-infinite edges. Figure 4–12 depicts the frequency distribution of polygon shapes in different FECVT and PVT models. Although both the FECVT and PVT methods create cells more than ten edges, we do not see such cell shapes in the original micrographs. However, in contrast to PVT models, the FECVT models are inclined to hexagon-dominated where five-sided polygons are counterbalanced by seven-sided polygons. The FECVT models display geometric randomness, but they strongly tend to follow Euler's law, which relates the number of vertices V, edges E, and faces F of cells. As a consequence of Euler's law, an irregular honeycomb with an edge-connectivity of 3 should have, on average, six sides per face. For a honeycomb with regular hexagonal cells, the average number of sides is $\langle n \rangle = 6$; in these centroidal Voronoi models, $\langle n \rangle$ varies from 5.94 to 5.98 while for the PVT models, $\langle n \rangle$ varies from 5.82 to 5.95. When we compare the average cell sides between the two types of models, we note that the FECVT models have the tendency to follow Euler's law more accurately.

Biological tissues, soap bubbles and polycrystalline grains are natural examples of random, space-filling cellular networks. Despite large differences in length scales and formation processes, all these cellular networks evolve to a

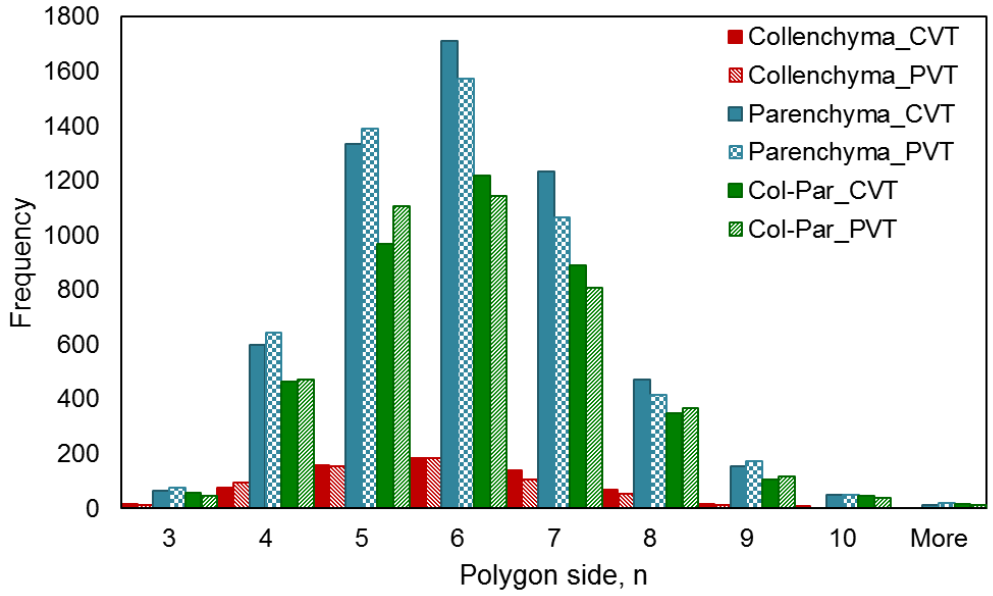

Figure 4–12: Frequency distribution of polygon side of the FECVT and PVT models for the collenchyma tissue, parenchyma tissue and combined collenchyma-parenchyma tissue of the *Rheum rhabarbarum*. The average number of sides in the FECVT models varies from 5.94 to 5.98; for the PVT models, On the Other Hand, it ranges between 5.82 and 5.95.

steady state with a similar structure. In most systems, the pinning of boundaries by surface grooving leads to stagnation of grain or tissue growth. This can be characterized by measuring the spatial distribution of cell sizes, shapes and their geometric correlations. There is a strong correlation between the microstructural geometry and the structural properties of space-filling networks. The interdependence between topology, geometry and physical dynamics of the spherulitic grain size-shape arrangement in semi-crystalline polymeric cellular networks has been shown both experimentally and theoretically [133, 134]. In naturally evolved cellular structures, the few-edged cell has a tendency to be in contact with many-edged cells and vice versa [135, 136]. Since the FECVT models represent plant tissues, they are expected to follow this spatial distribution. In Figure 4–13, we observe that polygons with fewer sides tend to be surrounded by polygons with more sides and that this holds true for all the

models generated by both the FECVT and PVT methods. We expect similar trends for both the types of models, since only the distribution of the points is different in the Poisson Voronoi tessellation.

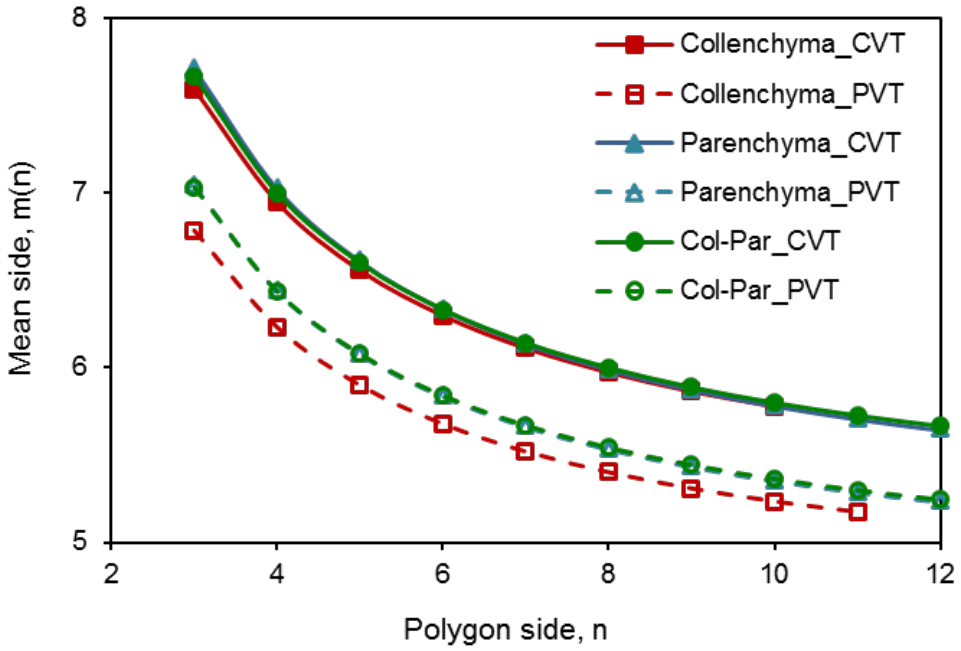

Figure 4–13: Polygons of fewer sides are surrounded by the polygons of more sides for different FECVT and PVT models. In naturally evolved cellular structures, the few-edged cell has a tendency to be in contact with several edged cells and vice versa [135, 136].

Furthermore, Aboav-Weaire [135, 137] established a linear relationship between the mean cell sides and the neighbouring cell sides for an infinite random cellular structure. This correlation is empirical and is satisfied by a large number of naturally grown cellular structures. According to the Aboav-Weaire law, on average, the sum of the number of sides of the cells immediately adjacent to an $n-$sided cell, $nm(n)$ is linear in n such that,

$$nm(n) = (6 - a)\, n + (6a + \mu_2) \tag{4.4}$$

where, μ_2 is the second moment of the $P(n)$, the probability distribution of the number of edges and a, a system-constant, is a measure of nearest

neighbour correlation that depends on the topology. Generally, in biological structures, a is in the order of 1 [138, 139]. The second moment is defined as $\mu_2 = \sum_n P(n)(n - \langle n \rangle)^2$, where,$\langle n \rangle$ is the average with respect to the same distribution, $P(n)$, and whose variance, $var(n) = (\langle n^2 \rangle - \langle n \rangle^2)$ is a measure of topological disorder. However, for finite networks with $\langle n \rangle \neq 6$, the topological model yields the relation,

$$nm(n) = (\langle n \rangle - a)\, n + \left[\langle nm(n) \rangle - \langle n \rangle^2 + \langle n \rangle a\right] \tag{4.5}$$

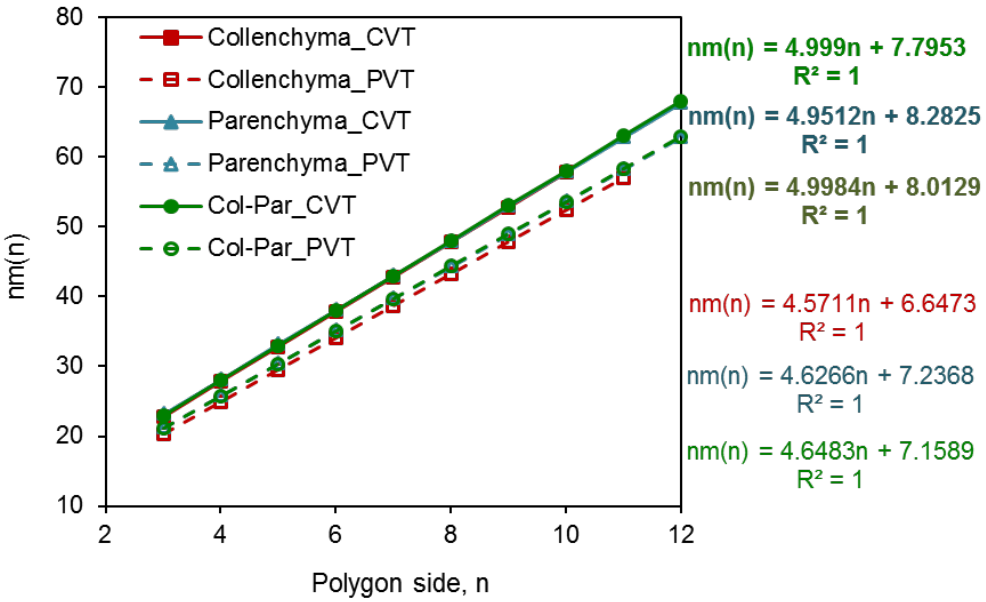

Figure 4–14: Aboav-Weaire law for 2D topology. A linear relation between the mean cell sides to the neighbouring cell sides for a random cellular structure. The upper 3 equations in bold represent FECVT models and the lower 3 equations represent PVT models.

A wide range of experiments conducted on various natural structures have demonstrated that their cellular geometries obey the above correlations [135, 138–140]. In Figure 4–14, the tessellated models for both the FECVT and PVT methods display a linear relationship between the mean sides of the polygonal cells and the surrounding cells. The variation of mean cell sides can

be completely explained by the polygons side since coefficient of determination R^2, is 1.For the FECVT models, $a \approx 1$, whereas for the PVT models, $a \approx 1.4$. The parameter a quantifies the deviation of the slope from the average number of sides. Hence, the FECVT method is apparently an appropriate tool for generating virtual models of plant tissues.

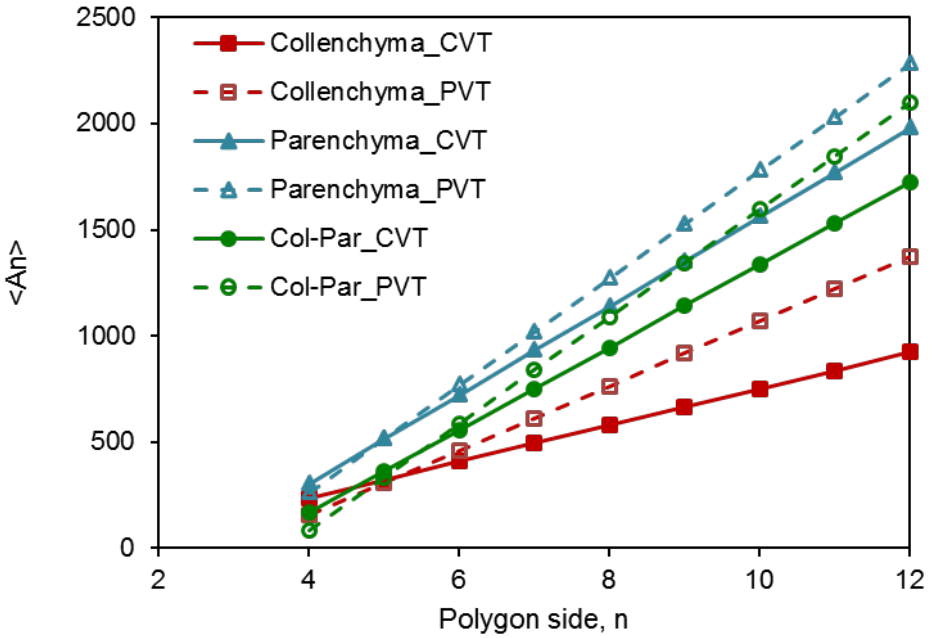

Figure 4–15: Relations between the average area of cells and the number of polygon sides for the FECVT and PVT models. The linear relationship between cell size (area) and shape, stated in Lewis's law, holds true for biological tissues and various cellular networks.

Another useful statistical measure, Lewis' law, states that the average area of a polygon with n sides $\langle A_n \rangle$ should be a linear function of the number of sides n, which holds true for various cellular networks and biological tissues [135, 136, 141–143],

$$\langle A_n \rangle = \langle A_n \rangle \left[1 + \lambda \left(n - 6\right)\right] \qquad n \geq 3 \tag{4.6}$$

where λ is a constant and usually, $\lambda = 1/4$ for a Voronoi tessellation [144]. Mombach *et al.* [145] investigated five different epidermal vegetable tissues

and found the values of λ in the range of $0.16 - 0.23$. Figure 4–15 shows the correlation between the sizes and shapes of the cells for the FECVT models and the corresponding PVT models. In the virtual tissues (Voronoi models) generated by both the methods, as expected, the average area $\langle A_n \rangle$ of the n sided cells varies monotonically with varying n. In the FECVT models, λ varies from 0.18 to 0.37, whereas in the PVT models, λ varies from 0.24 to 0.48. Speculatively we can say, λ is influenced by the dispersion of cell areas as well as the number of cells. The values of λ for the FECVT models are close to its usual value [144].

Topologically, the shape of the Voronoi polygons is considered to be random variable. The polygons cannot be defined and distinguished by their sizes or any other metric measures alone. For this reason, we can use topological entropy as a measure of randomness, i.e., a statistical measure of a disordered pattern. The topological entropy, S_t, is defined as $S_t = -\sum_n p(n) ln(p_n)$, where $S_t \geq 0$ and p_n is the probability of finding $n-$sided polygons within a Voronoi diagram. For perfectly regular and periodic patterns, the topological entropy is zero. It increases with the increasing randomness of the polygons in a region of interest [43]. The image entropies of the collenchyma and parenchyma tissues are 1.82364 and 1.84739, respectively, while the corresponding FECVT models' entropies are 1.73274 and 1.76854, respectively. In contrast with FECVT, the PVT models' entropies are 1.68957 and 1.70265, respectively. The image entropy is calculated from a greyscale image derived from a color micrograph. The entropic variation between the image and its model is partly due to the conversion of the image to greyscale and also to the original quality of the micrograph. For the high magnification wedge-shaped micrograph, the image entropy and FECVT model entropy are closer to each other. Cell boundaries tend to appear sharper under higher magnification, which allows the

corresponding FECVT model to be as random as the natural microstructure. In case of the whole tissue (collenchyma-parenchyma) tissue, the image entropy and the corresponding FECVT and PVT models entropies are 1.81623, 1.79045, and 1.74398, respectively. However, for all the tissues, FECVT model entropies are close to the corresponding image entropies comparing with PVT models. These statistical analyses demonstrate the applicability of the FECVT method to a range of different tissue microstructures. In a nutshell, the accuracy of the model in capturing the microstructure is highly dependent on the quality, resolution and magnification of the micrograph.

4.8 Summary

The chapter focuses on the generation of Voronoi model that can realistically capture the microstructure of plant tissues. To demonstrate the effective application of the FECVT method, three distinct and complex non-periodic structures displaying graded cellularity have been modeled. The geometric representation of a tissue can enhance our understanding of how microstructure determines mechanical properties. The fidelity of the prediction FECVT models are assessed and partially validated by topological laws as well as experimental data and compared with PVT models. A number of statistical and topological analyses manifest the appropriateness of the FECVT method in modeling plant tissues.

The FECVT method can be used to capture the microstructure of any shape, in which the tissues display complex heterogeneity and graded cellularity. The use of an edge detection algorithm augments the ability of the FECVT method to represent these types of geometries. The model can be generated using MATLAB without the assistance of any other image processing software and can be integrated directly with FEA software (ANSYS) without the need for pre-processing. Additionally, the FECVT method can generate a model

with finite edges, making it easier to study the mechanics of the structure using finite element analysis. The geometric models are representative of the structures they mimic and allow us to computationally model the elastic properties, will be described in next chapter, of a cellular tissue with higher accuracy.

CHAPTER 5
Finite Element Analysis and Effective Stiffness of Tissues

5.1 Overview

This chapter describes the finite element analysis (FEA) of the collenchyma and parenchyma tissues, generated by the finite edge centroidal Voronoi tessellation (FECVT), of the model plant. Coupling the cellular microstructure (geometric representation) and cell wall (material) properties, the effective stiffness of the tissues is obtained by using a numerical homogenization technique via detailed finite element analysis of the models of sub-regions of the tissues. Since the microstructures of the tissues are highly random, a representative volume element (RVE) would not have been effective to capture the extensive randomness observed in the tissue. Hence, a stochastic approach has been adopted in this work to obtain the characteristic apparent tissue stiffness. The statistical volume element (SVE) is, therefore, considered, as opposed to a large-scale RVE. The finite element analysis of FECVT models—the SVEs—are conducted in ANSYS. With appropriate boundary conditions, the FEA can capture the random microstructural variations and determine the apparent (homogenized) stiffness of the FECVT models. This chapter provides the apparent/effective stiffness of the tissues and their combination. The results yield insight into the effect of cell size and the graded cellularity of the tissue stiffness.

5.2 Finite Element Modeling for Homogenized Tissue Properties

Although the mechanical properties of a random microstructure can be determined by using direct numerical simulation, this strategy is computationally expensive to apply throughout the whole domain. Instead,

the homogenized/effective properties of a material with random microstructure can be obtained from an RVE, which avoids the use of a large scale direct numerical simulation [146,147]. The RVE contains the essential microstructural features and has been widely used to compute the effective material properties of heterogeneous and composite material having microstructural irregularities such as grains, inclusions, voids, fibers and others. An appropriate RVE needs to be (a) spatially invariant and large enough to represent the microstructural variability, and (b) representative of a microstructure that is typical of the entire microstructure [148]. Since the intrinsic non-homogeneity in the constituent tissues of the rhubarb petiole is highly random, it is not viable to capture the heterogeneity with a single FECVT model because the requirement of the RVE size, being infinite, is neither practical nor desirable, and the simulation of such a large RVE may suffer from a heavy computational burden [149, 150].

In the present analysis, to overcome the limitations of the RVE approach and to address the effect of microstructural variability in the constitutive tissue properties, the concept of SVE is adopted. The size of the SVE is smaller than a conventional RVE, but larger than the microstructure characteristic length scale [151]. Hence, each of the FECVT models of a particular tissue should correspond to the respective SVE for the numerical simulation so as to capture the microstructural randomness present in the tissue. To obtain the effective/homogenized mechanical properties, the numerical simulation of compressive deformation in each SVE is performed by finite element analysis. The stochastic approach of using several SVEs better captures the overall randomness present in a tissue.

5.2.1 Construction of the Finite Element Model

The geometric information of the FECVT model (i.e., SVE) is transferred to ANSYS, and the model is reconstructed using ANSYS Parametric Design

Language (APDL). In the finite element model, the cell walls are considered to be straight and of uniform thickness throughout the generated model. The relative density of a given model is specified by assigning the appropriate cell wall thickness. The constitutive behavior of the wall material is assumed to be elastic-perfectly plastic according to J_2 plasticity theory. Each cell wall of the Voronoi microstructure is modeled with a BEAM23 element, which is capable of modeling both elastic and plastic behavior. The shear deformation, which is important for stubby beams, also is captured by considering the shear deflection coefficient of the beam element. The beam elements have a rectangular cross-section of uniform thickness t. The relative density, ρ^*/ρ_s of the SVE, is given by

$$\frac{\rho^*}{\rho_s} = \frac{area\ of\ solid\ walls}{total\ area\ of\ a\ Voronoi\ model} = t\frac{\sum_{i=1}^{N} l_i}{L_X L_Y} \tag{5.1}$$

where N is the total number of beams, l_i is the length of the beam i; L_X and L_Y are the dimensions of the Voronoi model along X and Y axes, respectively. The FEA is conducted for different relative densities, adjusted by the value of t. In the finite element analysis, a Young's modulus $E_s = 1$ is assigned to each beam to obtain the normalized tissue stiffness. To present the FE results in non-dimensional form and to facilitate the loading condition, the value of Young's modulus is only chosen for convenience. The finite element model accounts for the appropriate loading and boundary conditions, as explained in the following section.

5.2.2 Loading and Boundary Condition

One of the most important aspects of using the FEA is the decision about the most suitable boundary conditions. The best boundary condition should lead to the average global behavior for the 2D FECVT models and

avoid any localized deformation near the mesh boundaries. Three types of boundary conditions (BC) generally imposed by the FEA are the (1) periodic boundary condition, (2) prescribed displacement boundary condition, and (3) mixed boundary condition [20, 152]. The *periodic boundary condition* assumes that the corresponding nodes on the opposite beams or struts of the mesh have the same expansion or compression in the normal directions, the same displacements in the other directions, and the same rotations in all directions. Since the microstructures of the tissues (and corresponding FECVT models) are not periodic, the periodic boundary condition is not appropriate for use in the current analysis. On the other hand, the *prescribed displacement boundary* condition enforces very strong constraints and is usually used with problems related to plastic deformation. The *mixed boundary condition* enforces the normal displacement, which eliminates the tangential force and the bending moments at the nodes on the boundaries. Since the mixed boundary condition tends to underestimate the Young's modulus [20, 152], the displacement boundary condition has been selected here as it was proved to be appropriate for the analysis of non-periodic microstructures for uniaxial and biaxial loading cases [11, 12, 55, 153, 154].

To determine the effective Young's modulus, the uniaxial compression load with prescribed displacement is simulated in both X and Y directions. A uniaxial compressive strain along the X axis is imposed on the nodes of the right edge, while the nodes at the left edge are constrained from translating in this direction as shown in Figure 5–1(a). The nodes of the bottom edge also are constrained from translating in the Y direction to prevent the rigid body motion. Similarly, uniaxial compression along Y axis also is performed (Figure 5–1[b]). In both cases, the nodes are constrained from rotating in the $X - Y$ plane. To determine the effective shear modulus as shown in Figure 5–1(c),

a biaxial loading test has been simulated with a positive displacement in the X direction and a negative displacement in the Y direction. The results have been computed for the alternative values of relative densities for the prescribed boundary condition.

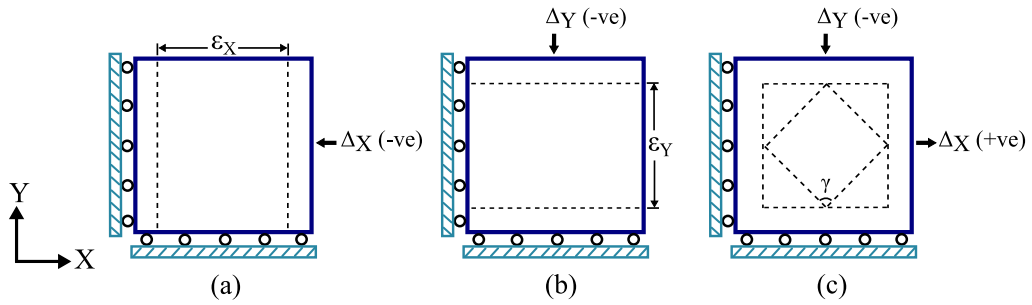

Figure 5–1: Simulated tests for determining the effective stiffness properties.

5.2.3 Determination of the Effective Stiffness Properties

For each model with a given relative density, the effective Young's modulus E^*,and effective shear modulus G^*_{XY} are determined. The macroscopic stress σ^* is calculated from the global reaction forces of the structure in the loading direction. The sum of the nodal reaction forces is divided by the edge length to determine the average normal stress in the loading direction. The strain ϵ^* is determined based on the technique of gage lines introduced by Silva [12] so as to eliminate the end effects. The displacement at each location, where the gage line intersects a cell wall, is computed using a linear interpolation of the displacements of the two adjacent nodes. For a given pair of gage lines, the normal strain is computed as the change in distance between the gage lines divided by their original distance. The shear strain is computed as the change in the angle between the gage lines oriented at 45° with respect to the coordinate axes. Nevertheless, the computed elastic constants for any model may vary by several percent, depending on the location of the gage lines.

5.3 Experimentally Determined Tissue Stiffness

The stiffness of parenchyma tissues is experimentally determined and later compared with the tissue stiffness obtained via computation. Cubes of parenchyma tissue were cut using a potato chipper and a knife, and their dimensions were measured with digital calipers. The cubes were placed between two glass plates and tested in compression using a Micro EP miniature UTM (ADMET) fitted with a 10 lb load cell. Data were sampled and acquired at 100Hz using an MTESTQUATTRO system from ADMET. The stiffness of the parenchyma tissue was found to 4.87 (SD 0.73) MPa and 4.36 (SD 1.47) MPa for the basal and apical location, respectively.

5.4 Computational Results and Discussion

The normalized stiffness properties of the collenchyma, parenchyma, and combined collenchyma and parenchyma (col-par) tissues are approximated by using the FEA of the respective FECVT models—the SVE. The finite element analyses of the SVEs determine the average stiffness of the corresponding tissues. The FECVT model captures the cellularity present in the tissue microstructure, which in turn is used in the FEA.

5.4.1 Effective Stiffness of Collenchyma Tissue using the FEA

The FECVT models of the collenchyma sections are simulated in ANSYS to determine the effective tissue stiffness. Each of the FECVT models is simulated for a set of relative density, varying from 5% to 30%. Figure 5–2 shows the nodal displacements of the model tissue for 15% relative density, with compressive strain along X and Y directions. The microstructure in the X direction is less stiff than that in the Y direction. The microstructural anisotropy of the plant tissue originates from the cellular distribution.

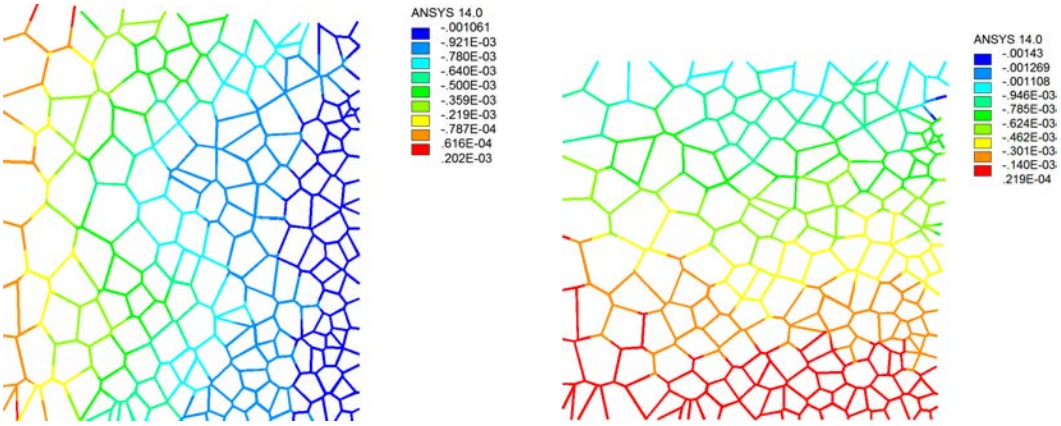

(a) Nodal displacement along X direction (b) Nodal displacement along Y direction

Figure 5–2: Nodal displacement of FECVT model of collenchyma tissue under uniaxial displacement BC [18](a) X component of nodal displacement (b) Y component of nodal displacement.

Figures 5–3(a) to 5–3(c) represent the variability of the computed stiffness with one standard error. The variations of the shear moduli are significant compared to the Young's moduli of the FECVT models at varying density.

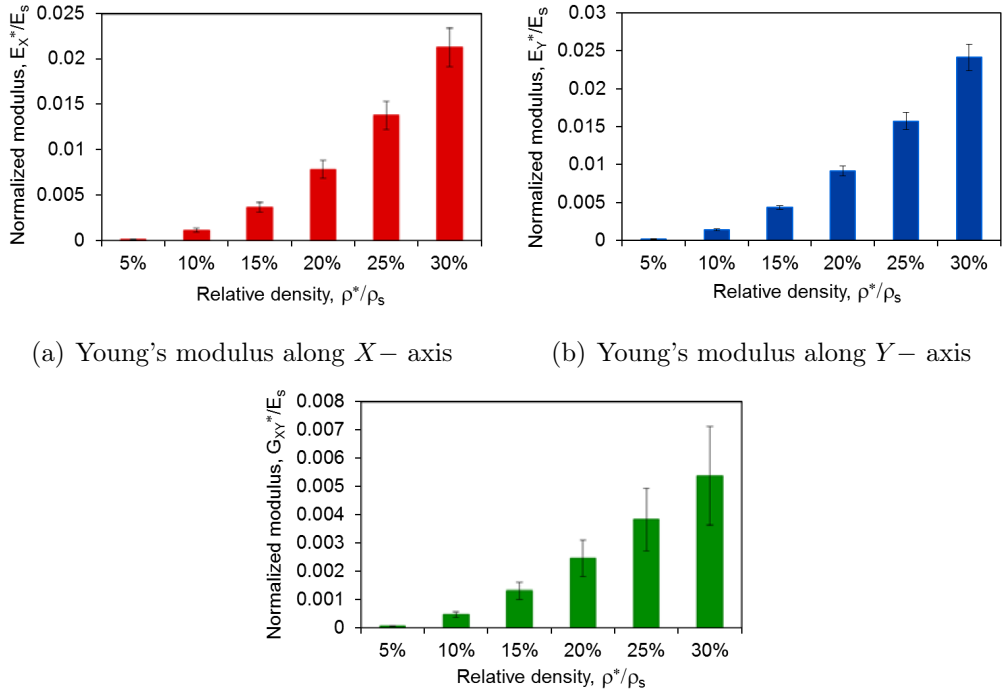

(a) Young's modulus along $X-$ axis (b) Young's modulus along $Y-$ axis

(c) Shear modulus

Figure 5–3: Variability of the mean stiffness of the FECVT models of collenchyma tissue for varying relative density with one standard error.

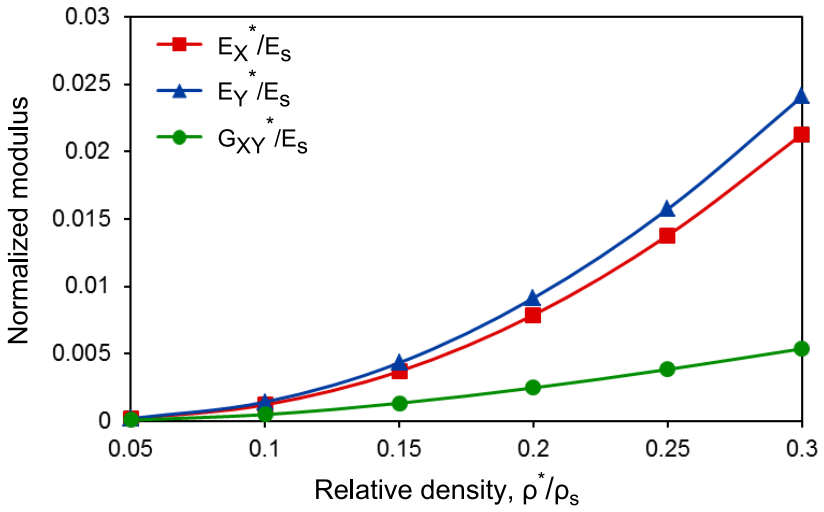

Figure 5–4: Normalized moduli of the FECVT model of collenchyma tissue.

The normalized effective stiffness of the FECVT model along the Y direction is around 15% to 25% higher than that of the FECVT model along the X direction for the range of density considered here (Figure 5–4). The variation reflects the stiffening effect of the cell shape, size, and cellular distribution, and also depicts the anisotropic behavior of the collenchyma tissue of the rhubarb petiole. Figure 5–5 depicts the variability of the Poisson's ratio, ν^*_{XY} and ν^*_{YX}, of the FECVT model of the collenchyma tissue. However, the effective Poisson's ratios, ν^*_{XY} and ν^*_{YX}, exhibit no difference within the range of relative density (Figure 5–6).

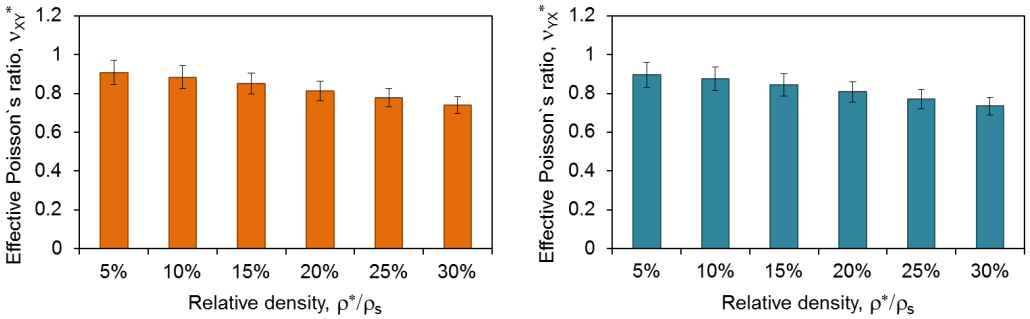

(a) Poisson's ratio ν^*_{XY} (b) Poisson's ratio ν^*_{YX}

Figure 5–5: Variability of mean Poisson's ratio of the FECVT models of collenchyma tissue for varying relative density with one standard error.

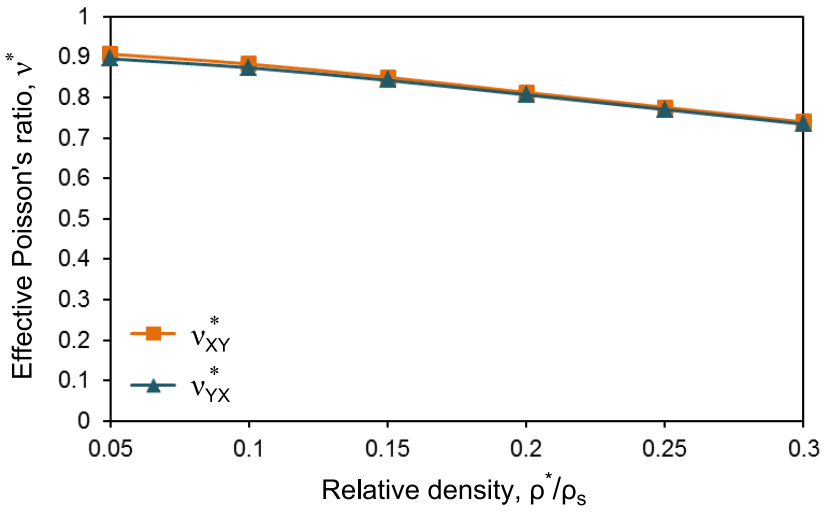

Figure 5–6: Effective Poisson's ratio of the FECVT model of collenchyma tissue.

5.4.2 Apparent Stiffness of Parenchyma Tissue using the FEA

The FECVT models of the parenchyma sections also are simulated for the range of relative density, $0.05 \leq \rho^*/\rho_s \leq 0.30$, in ANSYS to determine the effective tissue stiffness. Figure 5–7 shows the nodal displacements of model tissue for 15% relative density, with compressive strain along X and Y directions. The microstructure in the Y direction is less stiff than that in the X direction, whereas the collenchyma is less rigid in X direction; this indicates that the microstructural anisotropy of the parenchyma tissue displays an opposite behavior compared to the collenchyma tissue.

Figures 5–8(a) to 5–8(c) represent the variability of the computed stiffness with one standard error. Similar to the collenchyma tissue, the variations of the shear moduli are significant compared with the Young's moduli of the FECVT models at varying relative density.

The normalized effective stiffness of the parenchyma FECVT model along the X direction is an average of 15% higher than that of the FECVT model along the Y direction for the range of density considered here (Figure 5–9). The clustered and graded cellularity of the vascular bundle stiffens the parenchyma

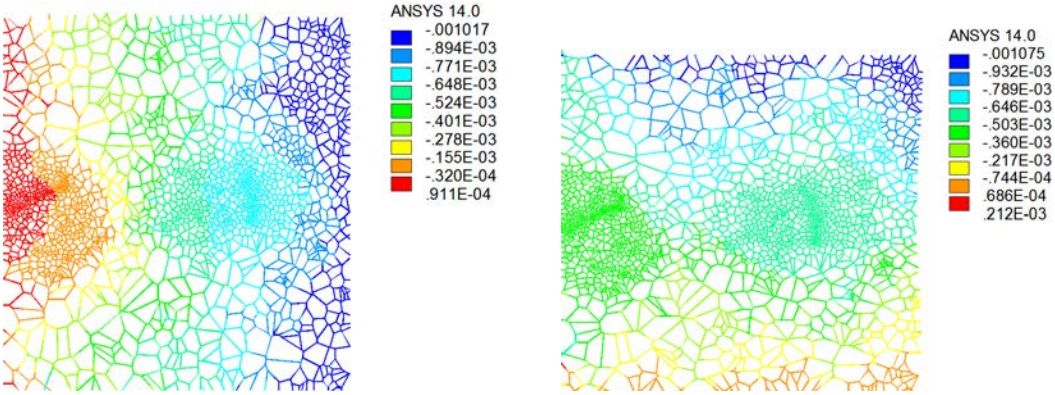

(a) Nodal displacement along X direction (b) Nodal displacement along Y direction

Figure 5–7: Nodal displacement of FECVT model of parenchyma tissue under uniaxial displacement BC (a) X component of nodal displacement (b) Y component of nodal displacement.

tissue in X direction compared to Y direction. Along with the higher gradient in clustered regions, the cell size and cellular distribution lower the stiffness

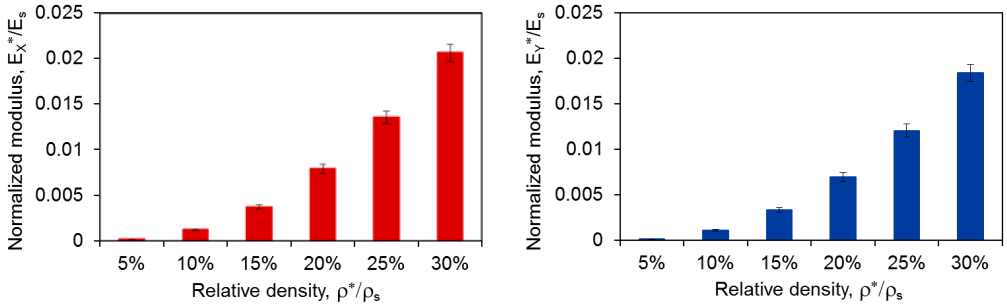

(a) Young's modulus along $X-$ axis (b) Young's modulus along $Y-$ axis

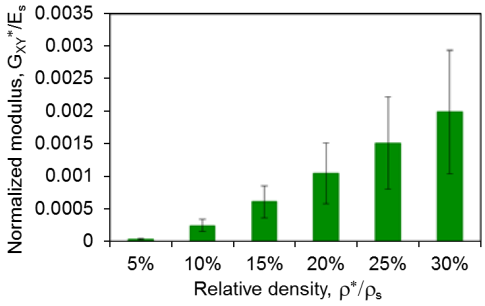

(c) Shear modulus

Figure 5–8: Variability of the mean stiffness of the FECVT models of parenchyma tissue for varying relative density with one standard error.

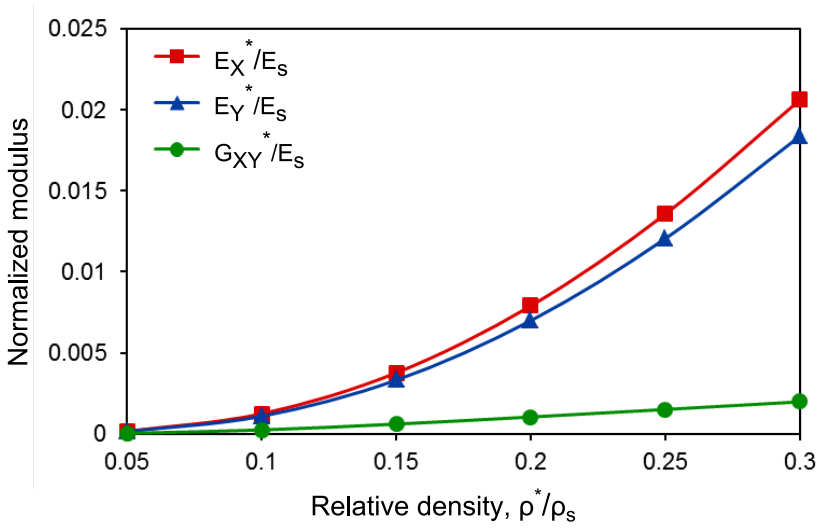

Figure 5–9: Normalized moduli of the FECVT model of parenchyma tissue.

of the parenchyma tissue compared to the collenchyma tissue. Figure 5–10 depicts the variability of the Poisson's ratios, ν^*_{XY} and ν^*_{YX}, of the FECVT model of the parenchyma tissue. However, the effective Poisson's ratios, ν^*_{XY} and ν^*_{YX}, of the FECVT model of the parenchyma tissue exhibit an average of 15% difference within the range of specified relative density (Figure 5–11). From a structural point of view, the micro-architecture of the parenchyma tissue seems to be the origin of this variation.

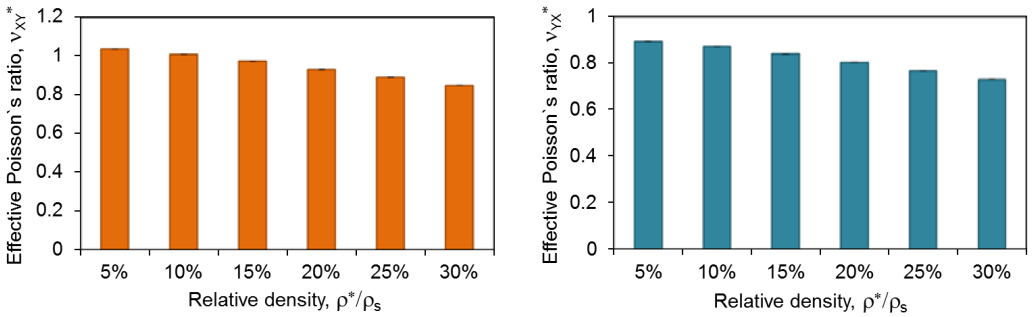

(a) Poisson's ratio ν^*_{XY} (b) Poisson's ratio ν^*_{YX}

Figure 5–10: Variability of mean Poisson's ratio of the FECVT models of parenchyma tissue for varying relative density with one standard error.

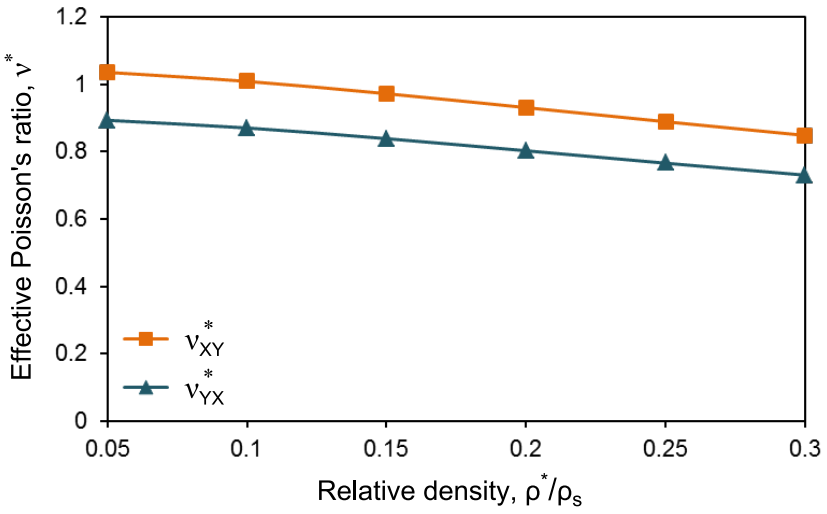

Figure 5–11: Effective Poisson's ratio of the FECVT model of parenchyma tissue.

5.4.3 Apparent Stiffness of Collenchyma-Parenchyma (Col-Par) Tissue using the FEA

Since the overall stiffness of a plant petiole or stem depends on the constituent tissues as a whole, the stiffness properties of the collective tissues also are analyzed in this section. To capture the cumulative effect of both the collenchyma and parenchyma (col-par) tissue, the FECVT models of the combined tissue sections also are simulated in ANSYS for the range of relative density, $0.05 \leq \rho^*/\rho_s \leq 0.30$, to determine the normalized tissue stiffness. Figure 5–12 displays the nodal displacements of the col-par FECVT model for 15% relative density, with compressive strain along the and directions. The displacements along both directions are close to same order of magnitude for the cellular distribution in the combined tissue.

Figures 5–13(a) to 5–13(c) represent the variability of the computed stiffness with one standard error. An expected trend of variability, similar to the collenchyma and parenchyma tissue, is observed for the combined tissues (Figure 5–14).

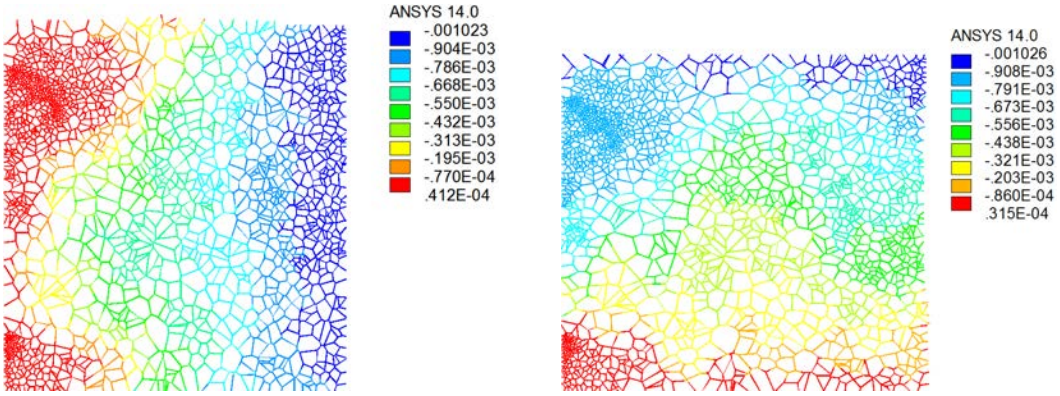

(a) Nodal displacement along X direction (b) Nodal displacement along Y direction

Figure 5–12: Nodal displacement of FECVT model of col-par tissue under uniaxial displacement BC (a) X component of nodal displacement (b) Y component of nodal displacement.

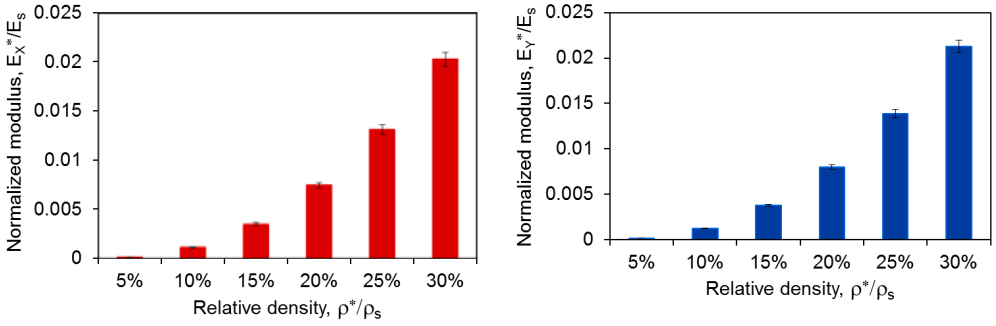

(a) Young's modulus along $X-$ axis (b) Young's modulus along $Y-$ axis

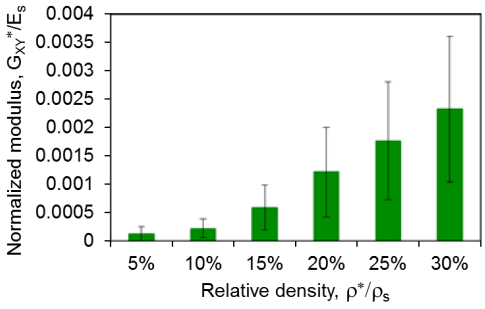

(c) Shear modulus

Figure 5–13: Variability of the mean stiffness of the FECVT models of combined collenchyma-parenchyma tissue for varying relative density with one standard error.

The combined effect of the collenchyma and parenchyma tissue is different than the individual tissues. The normalized effective stiffness of the col-par

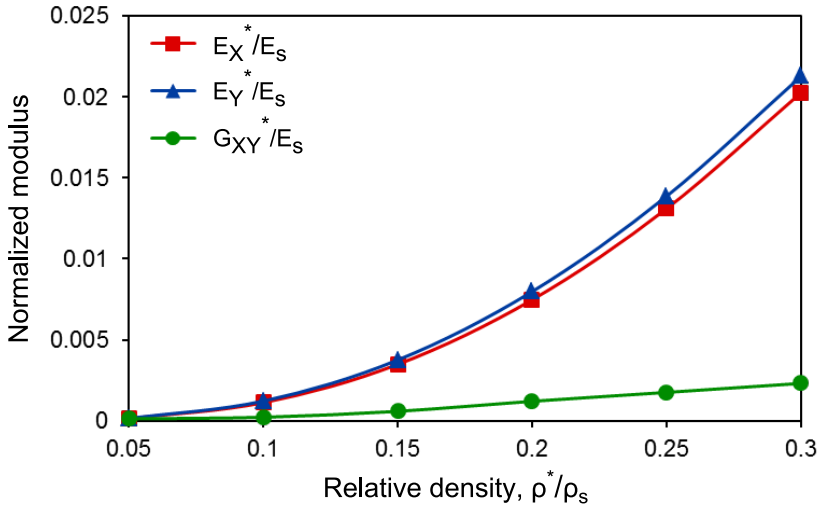

Figure 5–14: Normalized moduli of the FECVT model of combined collenchyma -parenchyma tissue.

FECVT model is nearly similar (an average of 4% higher along the X direction) along both the$X$ and Y directions throughout the relative density considered here (Figure 5–14). The overall effect of the combined tissues results in approximately equal stiffness. Nevertheless, the effective Young's moduli and shear modulus of the combined tissues are in-between the individual tissues. The Poisson's ratios, ν_{XY}^* and ν_{YX}^*, of the FECVT model of the combined tissues also exhibit a difference between the ratios (Figure 5–15 and 5–16).

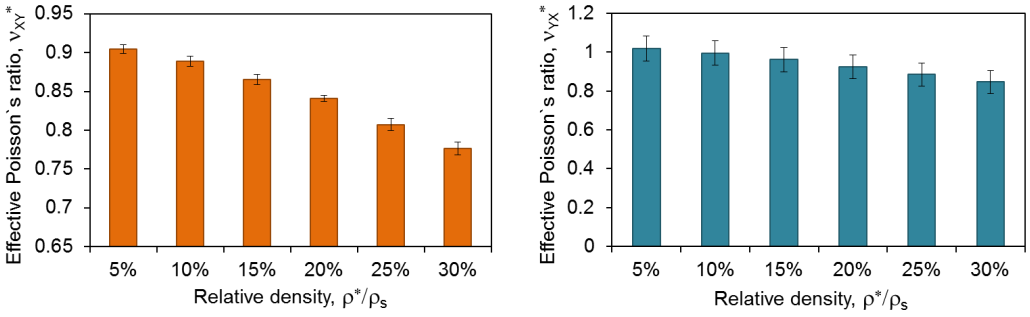

(a) Poisson's ratio ν_{XY}^*

(b) Poisson's ratio ν_{YX}^*

Figure 5–15: Variability of mean Poisson's ratio of the FECVT models of col-par tissue for varying relative density with one standard error.

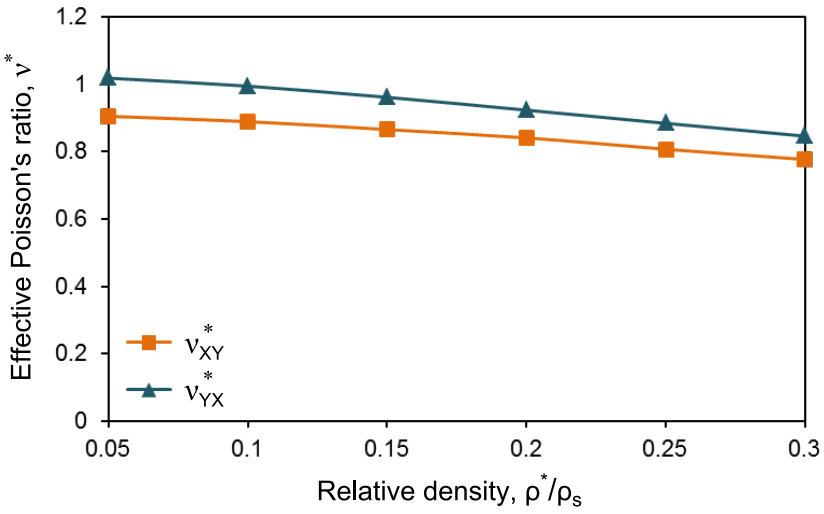

Figure 5–16: Effective Poisson's ratio of the FECVT model of combined collenchyma-parenchyma tissue.

The normalized stiffness of the individual tissues and their combination provides insight into the effect of cell size, shape, and cellular distribution with clustered and complex higher area gradient present in the rhubarb petiole. The analyses presented in these sections have manifested the micro architectural effect of constituent tissues.

5.4.4 Comparison of the Normalized Stiffness of Various Tissues

The normalized stiffness of the FECVT models are compared to the stiffness of a randomly generated Voronoi model, and the stiffness calculated from closed-form expressions available in literature for periodic cellular materials and used for plant tissue modeling [12]. However, this assumption is oversimplified and not well representative of the real random cellular distribution of plant tissue. These formulas are obtained with an isotropic periodic cellular model that has a hexagon as a unit cell and are given in Appendix C. On the other hand, the random Voronoi model is generated for a set of uniformly distributed points. Figure 5–17 shows a regular hexagonal unit cell and the randomly generated Voronoi model.

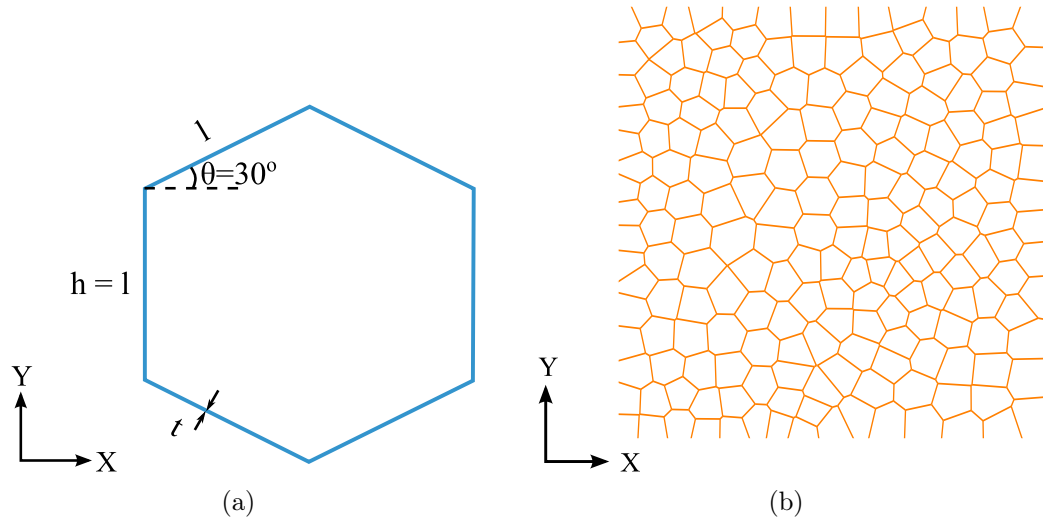

Figure 5–17: (a) Hexagonal unit cell (b) Randomly generated Voronoi model for uniformly distributed points.

The normalized stiffness of the FECVT models of collenchyma, parenchyma, and combined collenchyma-parenchyma tissues; randomly generated Voronoi model; and the hexagonal unit cell are shown in Figure 5–18. The FEA of the random Voronoi model shows an average of 8% and 6% higher axial and shear modulus, respectively, compared to the closed-form solutions obtained for the unit cell shown in Figure 5–17(a). The results of the moduli are in agreement with those presented by Gibson *et al.* [10, 12]. For a given set of relative density, the normalized effective elastic moduli of the different models at X and UY directions are shown in Figures 5–18(a) and 5–18(b). With respect to relative density, $0.05 \leq \rho^*/\rho_s \leq 0.30$, the FECVT models of the rhubarb tissues exhibit nearly equal stiffness, which is 31% to 40% less rigid than the randomly generated Voronoi model, and 29% to 35% less stiff than the periodic unit cell along the X direction. On the other hand, the stiffness of the FECVT models of the rhubarb tissues varies along the Y direction. Along this direction, for relative densities varying between 5% to 30%, the collenchyma FECVT model is 20% to 39% less stiff than the random Voronoi

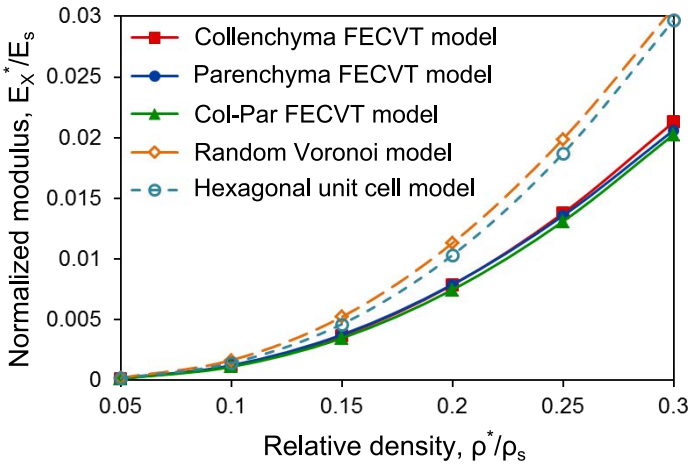

(a) Normalized modulus along $X-$ axis

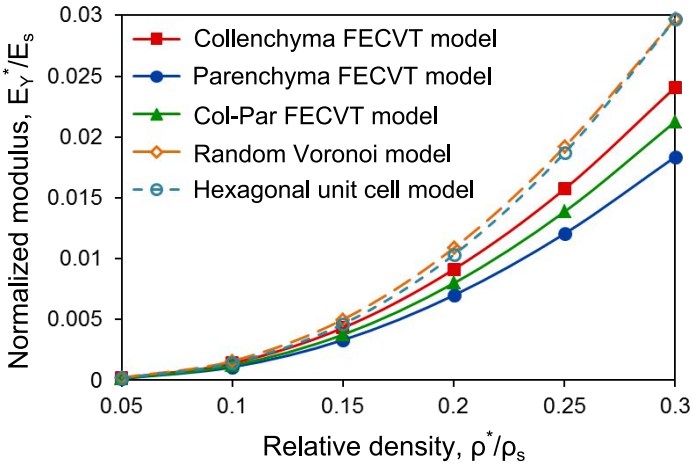

(b) Normalized modulus along $Y-$ axis

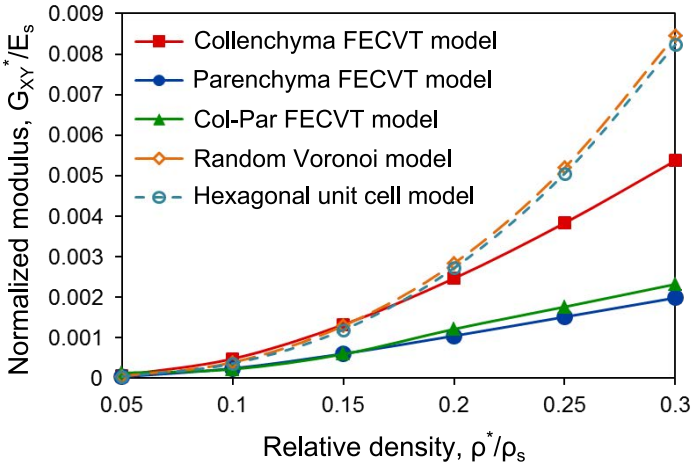

(c) Normalized Shear modulus

Figure 5–18: Comparison of the normalized modulus of the FECVT models of the different constituent tissues to random Voronoi and hexagonal unit cell models.

model and 15% to 35% less rigid than the unit cell model; the parenchyma FECVT model is 22% to 47% pliant than the random Voronoi model and 19% to 44% less stiff than the unit cell model. The col-par FECVT model is 18% to 39% more compliant than the random Voronoi model and 24% to 33% than the unit cell model. Similarly, the shear moduli of the FECVT models are considerably lower than both the random Voronoi and unit cell models. The shear modulus of the collenchyma FECVT model is 30% to 57% less rigid than the randomly generated Voronoi and hexagonal unit cell model. However, the FECVT models of the parenchyma and combined collenchyma-parenchyma tissues much less stiff than the random Voronoi and the unit cell models.

To generate the Voronoi tessellation, a uniform distribution of points has been imposed. Hence, the randomly generated Voronoi model displays a uniform cell size, a factor that influences the stiffness properties as shown in Figure 5–18. In the FECVT model, both the shape and size of the cells vary significantly with respect to the random Voronoi model and the hexagonal cell model. Therefore, the shape and size of the cells affect the normalized stiffness, which varies with density. The variation of the stiffness of the different FECVT models along the X and Y direction reflects the stiffening effect of the cell shape, size, and cellular distribution. Nonetheless, since the FECVT model contains smaller cells than those of the actual tissue, the stiffness could be overestimated. In addition, the short cell walls modeled by the beam element may impose superfluous stiffness.

Figure 5–19 depicts the effective Poisson's ratios for the FECVT, random Voronoi, and hexagonal unit cell models. The finite element analyses of the different FECVT models and random Voronoi models exhibit a marginal difference between the Poisson's ratio of ν^*_{XY} and ν^*_{YX}. The Poisson's ratios of the FECVT, and the random Voronoi model are weakly dependent on relative

density, and the micro-architecture of the tissue weakly affects the Poisson's ratio.

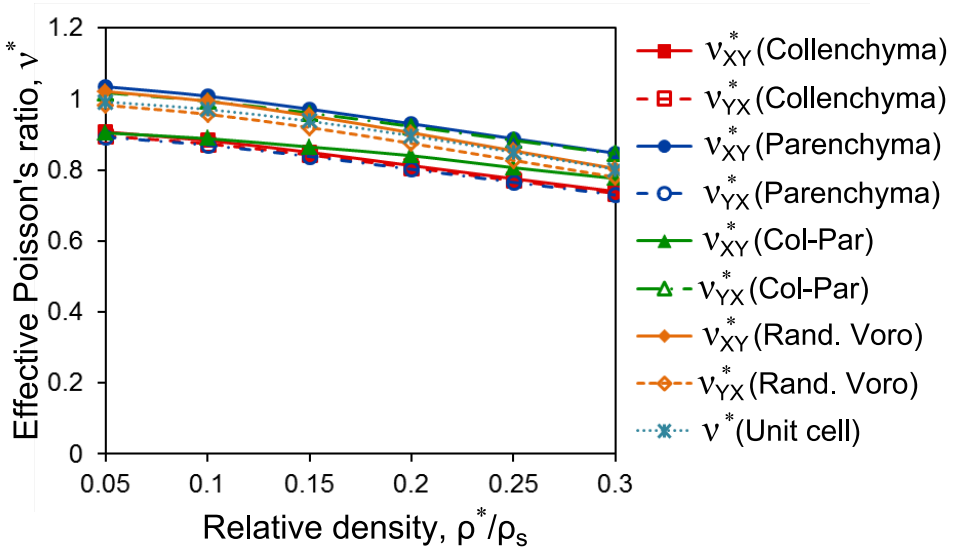

Figure 5–19: Comparison of effective Poisson's ratio of the FECVT models of the different constituent tissues to random Voronoi and hexagonal unit cell models.

5.4.5 Computational Stiffness of the Constituent Tissues of the Rhubarb Petiole

The effective stiffness of the cellular tissue can be obtained based on the computed wall stiffness described in Chapter 3. The effective axial and shear moduli of the collenchyma tissue vary between 9.2 $\sim$ 36.3 MPa and 2.3 $\sim$ 10.8 MPa, respectively. The axial stiffness of parenchyma tissue lies between 13.2 and 19.6 MPa and the shear modulus is approximately 6.7 MPa. However, the experimental stiffness of the fresh parenchyma tissue is approximately 5 MPa, which is considerably lower than the computed stiffness of the respective tissue. The stiffness of the cell wall of the collenchyma and parenchyma tissues are obtained by using typical cell wall configurations. Instead of using the generic composition of the dicotyledonous plant cell wall, the volume fractions and microfibril angle (MFA) of the model plant should be determined experimentally, so the corresponding computational stiffness would be more representative and

close to the actual tissue stiffness. Nevertheless, the computational stiffness of the parenchyma and collenchyma tissues provides a theoretical stiffness range for the constituent tissues.

5.5 Summary

In this chapter, the finite element analysis is used to assess the tissue properties of the rhubarb petiole, whose cellular microstructures have been modeled by using the FECVT algorithm presented in the previous chapter. Instead of a large scale RVE, the statistical volume elements, the FECVT models, of the tissue are considered to facilitate the FEA. The finite element analysis of the SVEs depicts the impact of complex heterogeneity and graded the cellularity in the tissues. The cell shape, size, and cellular distribution of the collenchyma and parenchyma tissues are shown to have a different impact on their respective normalized stiffness properties. The collenchyma tissue is found to be stiff along the Y direction, whereas the parenchyma tissue is stiff in the X direction. The axial stiffness of the combined tissue, on the other hand, is similar in both directions. The shear modulus of the collenchyma tissue also is higher compared to the parenchyma tissue, and is in-between for the tissues as a whole. By comparing these results with the randomly generated Voronoi and hexagonal unit cell models, a clear inference can be made that the cellularity in the rhubarb tissues make them more compliant. The apparent elastic properties of the constituent tissues will be used in Chapter 6 to create a theoretical stiffness map for the bending and torsional stiffness of the model plant.

CHAPTER 6
Flexural and Torsional Stiffness of Rhubarb Petiole

6.1 Overview

This chapter both computationally and experimentally examines the overall (macroscale) bending and torsional stiffness of the rhubarb petiole to characterize its compliance. In this chapter, the irregular cross-sectional shape of the petiole and the two layers of the constituent tissues are considered to evaluate the stiffness properties at the structural level. The arbitrary shape contour of the model plant rhubarb is generated by the Gielis superformula, which can produce a complex biological shape with reasonable accuracy. The stiffness and architecture of the constituent layered tissues are considered and modeled by using the concept of shape transformers so as to obtain the computational *twist-to-bend* ratio for the petiole. Additionally, structural efficiency maps displaying domains for bending and torsional stiffness also are generated to accommodate the experimental data for flexural and torsional stiffness of the rhubarb petioles. The maps may be a source of inspiration for biomimetic design, since they help to provide insight into the efficiency of the biological beams described by the different tissues properties, geometry, and turgidity.

6.2 Arbitrary/Irregular Shape and its Geometrical Properties

The shapes of biological organs are often asymmetric and difficult to capture. Since their geometry influences the overall mechanical properties of the organs, it is necessary to model their shapes and geometrical properties with considerable accuracy.

6.2.1 Gielis Parametrization

The capturing of the shapes of biological organisms and organs is an essential step to determine the stiffness properties, such as bending and torsional stiffness, of plant petioles. Circular, spherical, and cylindrical shapes and forms are observed occasionally in nature, whereas plant stem, petiole, and leaves often display a complex form in their adaptation to nature to provide mechanical support against the weight of the leaf and against environmental factors, such as rain and wind, resisting both bending and twisting load. Even though these asymmetric and complex shapes are mathematically difficult to represent, they can be interpreted as modified polygons, which are referred to *supershapes* [64].

The square and circle, rectangle and ellipse all belong to the family of Lamé curves [155], which are known as *superellipses*, and defined by

$$|x/a|^n + |y/a|^n = 1 \tag{6.1}$$

The superellipses can be divided into four quadrants only, a drawback for modelling asymmetric shape. Due to this limitation, the superellipses are not capable of generating a wide range of natural shapes, which are often far from being regular. Therefore, by using polar coordinates, the Gielis parametrization of the Lamé curves [64] has been introduced to redefine their formulation for biological cross-sectional shapes. This strategy enables the accurate representation of natural forms, which can be divided into a number of sectors equal to m using Equation (6.2), and is used here to capture the last order of hierarchy of the petiole, i.e., the arbitrary shape contour. With respect to the polar coordinates, the radius $r\,(\phi)$—a Gielis curve—is given by

$$r = f(\phi)\frac{1}{\sqrt[n_1]{\left(\left|\frac{1}{a}\cos(\frac{4}{m}\phi)\right|\right)^{n_2} + \left(\left|\frac{1}{b}\sin(\frac{4}{m}\phi)\right|\right)^{n_3}}} \tag{6.2}$$

where the parameters a and b control the scale, m represents the number of rotational symmetries, and n_1, n_2, and n_3 are the shape coefficients. The parameter n_1 determines the sharpness or the flatness of corners and the convexity of the sides. The parameters n_2 and n_3 determine whether the figure is circumscribed or inscribed. If $n_2, n_3 > 2$, the figure is circumscribed i.e., a super-polygon; and if $n_2, n_3 < 2$, the figure is inscribed i.e., a sub-polygon in the unit circle [64].

6.2.2 Geometric Properties of Irregular Shape

The topmost order of the structural hierarchy of the petiole shown in Figure 1–1 resembles the actual shape of the organ and is modeled by Gielis parametrization. To determine flexural and torsional stiffness, various geometric properties such as the area and second moment of area of the Gielis curve need to be calculated. Due to the irregular shape contour, the geometric quantities cannot be calculated with closed form expressions. Therefore, the domain integral is first transformed into the line integral by using Green's theorem. Then, the integral is computed using quadratic elements that represent the coordinates over the boundary. The procedure produces exact formulas for the shapes enclosed by boundaries that can be represented by 1^{st} or 2^{nd} order polynomials. The integrals are used to compute the area and inertial properties. Figure 6–1 shows a two dimensional arbitrary domain in the $x - y$ plane with a continuous piece-wise boundary.

The geometric and inertial properties of the domain can be obtained by integrating the following integrals:

$$A = \iint \mathrm{d}x\mathrm{d}y \tag{6.3a}$$

$$A_x = \iint y\mathrm{d}x\mathrm{d}y \tag{6.3b}$$

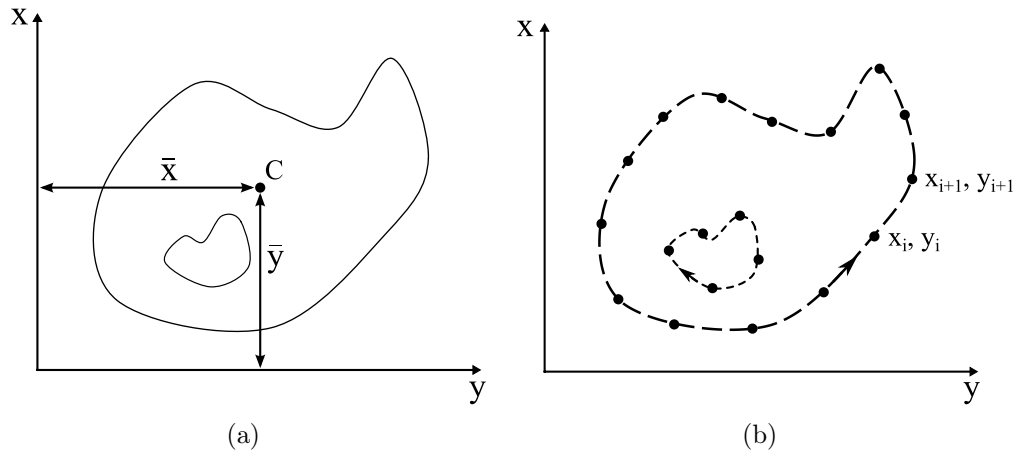

Figure 6–1: (a) 2-Dimensional arbitrary area with irregular interior and exterior boundaries (b) Discretization of interior and exterior boundaries.

$$A_y = \iint x \mathrm{d}x\mathrm{d}y \tag{6.3c}$$

$$I_{xx} = \iint y^2 \mathrm{d}x\mathrm{d}y \tag{6.4a}$$

$$I_{yy} = \iint x^2 \mathrm{d}x\mathrm{d}y \tag{6.4b}$$

$$I_{xy} = \iint xy \mathrm{d}x\mathrm{d}y \tag{6.4c}$$

$$\bar{x} = \frac{A_x}{A} \tag{6.5a}$$

$$\bar{y} = \frac{A_y}{A} \tag{6.5b}$$

where A is area, A_x is the moment of area about the $x-$axis, A_y is the first moment of area about the $y-$axis, I_{xx} is the second moment of area about the $x-$axis, $I_{yy}$is the second moment of area about the $y-$axis, I_{xy} is the product of inertia, and $\bar{x}$, and $\bar{y}$ are the centroid of the given domain. Each one of the preceding integrals can be written in one of the following forms:

$$I_1 = \iint \frac{\partial F_1}{\partial x} \mathrm{d}x\mathrm{d}y \tag{6.6a}$$

$$I_2 = \iint \frac{\partial F_2}{\partial y} \mathrm{d}x\mathrm{d}y \tag{6.6b}$$

$$I_2 = \frac{1}{2}\iint\left(\frac{\partial F_1}{\partial x} + \frac{\partial F_2}{\partial y}\right)\mathrm{d}x\mathrm{d}y \tag{6.6c}$$

where $F_1, x, xy, x^2/2, xy^2, x^3/3,$ and $x^2y/2$ for $A, A_x, A_y, I_{xx}, I_{yy},$ and I_{xy} respectively. The expressions for F_2 can be obtained in the same manner. Substituting the integrals of the Equations (6.3) to (6.5) in each one of the three forms given by Equation (6.6) and using the well-known Green's theorem for transforming domain to boundary integrals, the following equations are obtained for each case:

$$A_1 = \oint x\mathrm{d}y \qquad A_2 = -\oint y\mathrm{d}x \qquad A_3 = \frac{1}{2}\oint(x\mathrm{d}y - y\mathrm{d}x) \tag{6.7}$$

$$(A_x)_1 = \oint xy\mathrm{d}y \;\; (A_x)_2 = -\frac{1}{2}\oint y^2\mathrm{d}x \;\; (A_x)_3 = \frac{1}{2}\oint\left(xy\mathrm{d}y - \frac{1}{2}y^2\mathrm{d}x\right) \tag{6.8}$$

$$(A_y)_1 = \frac{1}{2}\oint x^2\mathrm{d}y \;\; (A_y)_2 = -\oint xy\mathrm{d}x \;\; (A_y)_3 = \frac{1}{2}\oint\left(\frac{1}{2}x^2\mathrm{d}y - xy\mathrm{d}x\right) \tag{6.9}$$

$$(I_{xx})_1 = \oint xy^2\mathrm{d}y \quad (I_{xx})_2 = -\frac{1}{3}\oint y^3\mathrm{d}x \quad (I_{xx})_3 = \frac{1}{2}\oint\left(xy^2\mathrm{d}y - \frac{1}{3}y^3\mathrm{d}x\right) \tag{6.10}$$

$$(I_{yy})_1 = \frac{1}{3}\oint x^3\mathrm{d}y \quad (I_{yy})_2 = -\oint x^2y\mathrm{d}x \quad (I_{yy})_3 = \frac{1}{2}\oint\left(\frac{1}{3}x^3\mathrm{d}y - x^2y\mathrm{d}x\right) \tag{6.11}$$

where the line integration over the exterior boundary is counter clockwise, and clockwise for the interior boundary as shown in Figure 6–1(b). The boundary is discretized by N number of nodes and intervals. The integration is performed over those intervals, and summing up the sub-integrals yields the desired area and inertial quantities. The discretized numerical boundary approximation is given in Appendix D. The area and inertial quantities are used to determine the flexural and torsional stiffness, where the effect of the cross-section plays an important role, as described in the next section.

6.3 Determination of Flexural and Torsional Stiffness using the Shape Transformers Method

The importance of the shape of engineering structures has been investigated using different methods [156–159]. To gain insight into the shape performance of engineering and natural structures, the shape transformers method was introduced [21, 160–162]. The concept is based on the geometry of the cross-section, which is described by two distinct contributions. The first is related to the size of the cross-section, whereas the second is the shape. The size is defined by a rectangle with the main dimensions of the cross-section and is referred to as the envelope D, as shown in Figure 6–2. S represents the shape of the cross-section enclosed in D, and its properties are dimensionless.

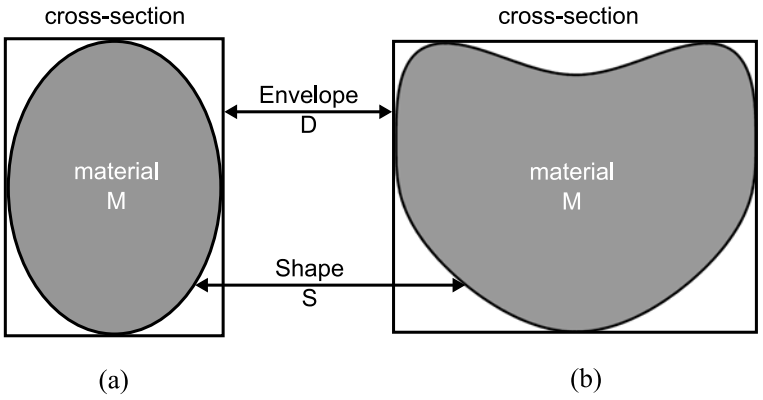

Figure 6–2: The constituents of a cross-section: shape and envelope.

The effect of the cross-section, multi-layered tissues, and cellular structuring within the tissues can be captured by using the method of shape transformers. With this method, a geometric quantity of a cross-section is normalized by the same geometric quantity of the surrounding envelope, which is a rectangle. Hence, the dimensionless shape transformers, ψ_g, of the geometric quantities, g, of a cross-section is defined by

$$\psi_g = \frac{g}{g_D} \tag{6.12}$$

where g_D is the geometric quantity of the envelope. For example, the shape transformers for area, the second moment of area (moment of inertia) about the $x-$axis, and the torsional constant can be defined as

$$\psi_A = \frac{A}{A_D} \tag{6.13a}$$

$$\psi_{I_{xx}} = \frac{I_{xx}}{I_{D_{xx}}} \tag{6.13b}$$

$$\psi_{J_T} = \frac{J_T}{J_{D_T}} \tag{6.13c}$$

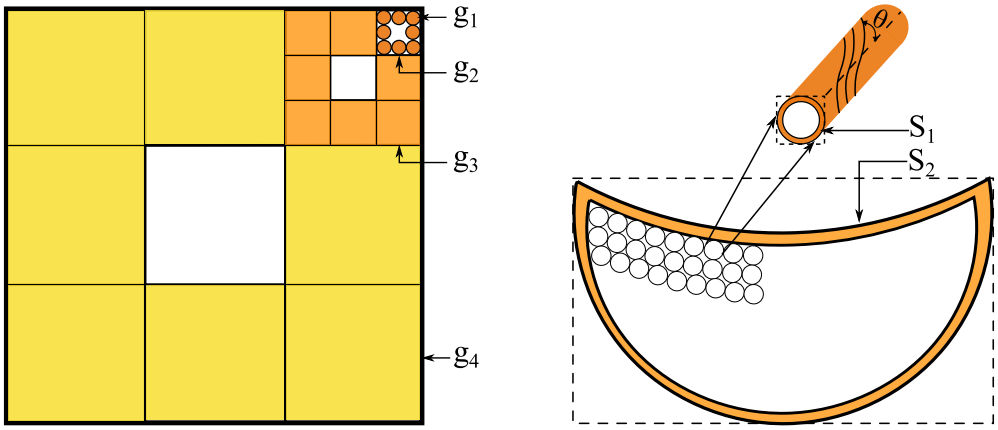

Figure 6–3: (a) An ideal cross-section structure (b) Structural hierarchies of a petiole. (Adapted from Pasini [22]).

To describe the structuring effect of a material, an idealized example can be examined as shown in Figure 6–3(a). This figure shows four hierarchical levels of a cross section, where the elements are assumed to be continuous at each order of hierarchy. At the order 0, the material M_0 is considered to be uniform and shapeless. When shaped, M_0 becomes a solid circular two-dimensional structure. During this process, M_0 is conferred with geometrical properties g_1 and M_1, i.e., the shaped material at order $n = 1$, and M_1 inherits properties $M_0 g_1$. The scheme of shape transformers, ψ_g, for instance, can be applied to

the bending stiffness [21, 66, 160]. The effective flexural property E_1 at the first order of hierarchy is obtained by normalizing $E_0 I_1$ with the envelope property I_{D1} and is expressed as

$$E_1 = E_0 \frac{I_1}{I_{D_1}} = E_0 \psi_I^1 \tag{6.14}$$

At the following hierarchical order, the circular elements of the first order are clustered together to form a hollow rectangular cross-section. Assuming that the circular elements of the first order exhibit isotropic and uniform material properties similar to the first level, the flexural property at the second order of hierarchy can be expressed as

$$E_2 = E_1 \psi_I^2 = E_0 \psi_I^1 \psi_I^2 \tag{6.15}$$

Therefore, the structure of two hierarchical orders is factored in by the shape properties, which can lead to the determination of the effective material properties. Further the structuring of the cells in the previous order results in an effective Young's modulus at the third hierarchical order and is expressed as

$$E_3 = E_2 \psi_I^3 = E_0 \psi_I^1 \psi_I^2 \psi_I^3 \tag{6.16}$$

If the process repeats at the higher orders (of hierarchy), the effective Young's modulus at the n^{th} order can be expressed as a ratio of effective material properties:

$$\frac{E_n}{E_0} = \prod_{j=1}^{n} \psi_I^j \tag{6.17}$$

To factor in the overall structure size, E_n in Equation (6.17) can be rearranged and substituted in the shape transformers expression of an *Equation of Mechanics E. M.* [21, 66]. Hence, mass, flexural, and torsional stiffness can be

expressed using the following relation:

$$E.M. = F \times M_0 \times \prod_{j=1}^{n} S^j \times g_D \tag{6.18}$$

where F represents the problem constant, g_D is the geometric quantity of the overall envelope, and S describes the shape properties at each hierarchical order. The Equation (6.18) is valid for a single-layered material. For a multi-layered structure consisting of different geometrical, material, and mechanical properties at each layer, the overall properties of the layered architecture are the sum of the properties of the integral layers.

The equation of mechanics can be applied to characterize the flexural and torsional moduli of the petiole having multi-layered tissues. To characterize the moduli of a multi-tissue system, the material properties of the layers, the shape and size of the cross-section, and the architecture and number of layers are considered as design variables. The model in the present work is based on the assumption that a perfect bonding occurs between each layer. Although this hypothesis is too unrefined to describe the real interfacial bonding between cells and layers, it still fits the purpose of an approximate study of the constituent materials, since it allows for finding limiting ideal bounds of the effective properties. The strain at the interface between materials also is anticipated to remain unchanged. It is assumed that flexural strain varies linearly along all the layers without any discontinuity. On the other hand, only the stress varies continuously within each layer, but discontinuously at the layer transition, since each material has its own modulus.

A petiole beam of generic cross-sectional shape, S, subjected to a pure bending moment, M_B, per unit width may consist of multiple material layers arranged with respect to the shape classes. The flexural stiffness and unit mass

of the system can be shown in simplified form:

$$\frac{M_B}{c_1} = \psi_I I_D E_D \tag{6.19}$$

$$\frac{m}{l} = \psi_A A_D \rho_D \tag{6.20}$$

where c_1 is the curvature of the beam. $\frac{M_B}{I_D c_1} = E_D$ and $\frac{m}{A_D l} = \rho_D$ are the effective properties of the beam, flexural modulus and density, respectively. To express these properties as a function $f\,()$ of the layer geometry, L_g, and their materials, we assign to the i^{th} layer, where $i = 1, 2, 3, \ldots k$, Young's modulus E_i and the second moment of area I_i, and density ρ_i and area A_i, respectively. Therefore, the geometry of the layer architecture can be expressed in terms of the shape transformers of each layer, ψ_{A_i} and ψ_{I_i}. Hence, the effective properties of the system can be shown as

$$E_D = \sum_{i=1}^{k} E_i \frac{I_i}{I_D} = \sum_{i=1}^{k} E_i \frac{\int_{A_i} y_i^2 \mathrm{d}A}{I_D} = \underbrace{\sum_{i=1}^{k} E_i \psi_{I_i}}_{f(L_g)} \tag{6.21}$$

$$\rho_D = \sum_{i=1}^{k} \rho_i \frac{A_i}{A_D} = \underbrace{\sum_{i=1}^{k} \rho_i \psi_{A_i}}_{f(L_g)} \tag{6.22}$$

Coupled with the cross-sectional shape of the layer, the transformed flexural modulus and density for the i_{th} layer can be expressed as

$$E_{T_{layer}} = \psi_I E_D = \underbrace{\psi_I}_{S} \underbrace{\sum_{i=1}^{k} E_i \psi_{I_i}}_{f(L_g)} \tag{6.23}$$

$$\rho_{T_{layer}} = \psi_A \rho_D = \underbrace{\psi_A}_{S} \underbrace{\sum_{i=1}^{k} \rho_i \psi_{A_i}}_{f(L_g)} \tag{6.24}$$

If structured materials exist among the layers, their contributions can be factored in by replacing E_n in Equation (6.17) with E_i in Equation (6.23)

$$E_T = \sum_{i=1}^{k} \left(E_0 \prod_{j=1}^{n} \psi_I^j \right) \psi_{I_i} \tag{6.25}$$

Including the effect of materials layering, the Equation (6.18) can be generalized in the following form:

$$E.M. = F \times M_0 \times \sum_{i=1}^{k} \left(E_0 \prod_{j=1}^{n} S^j \right) S_i \times g_D \tag{6.26}$$

This rationale can be used to evaluate the torsional stiffness and expressed as

$$J_T = \sum_{i=1}^{k} \left(J_0 \prod_{j=1}^{n} \psi_J^j \right) \psi_{J_i} \tag{6.27}$$

where J_T is the torsional constant of the cross-sectional shape. The preceding rationales can be used to evaluate the compliance of a petiole, resembling a cantilever, under wind and gravity loads. Therefore, the *twist-to-bend* ratio of a petiole with prescribed length and boundary conditions can be written as

$$\frac{EI}{GJ_t} = \frac{\sum_{i=1}^{k} \left(E_0 \prod_{j=1}^{n} \psi_I^j \right) \psi_{I_i}}{\sum_{i=1}^{k} \left(G_0 \prod_{j=1}^{n} \psi_J^j \right) \psi_{J_i}} \frac{I_{D_n}}{J_{D_n}} \tag{6.28}$$

where G is the shear modulus, J_t is the torsional constant of the cross-sectional shape. The above effective properties can capture the multiscale effect of changing the variables at different level of the structural hierarchy.

6.4 Experiments of Model Plant (Rhubarb) and Results

Since plant petioles and stems are soft compared to engineering materials and are of non-uniform cross-section, the mechanical testing could not be performed with a commercially available universal testing machine (UTM). Hence, a customized testing apparatus was constructed in-house to conduct

the mechanical tests. The experiments to determine the mechanical properties, the flexural and torsional stiffness, of petioles were conducted with imported rhubarb stalks from the Netherlands and USA. As mentioned earlier in Chapter 3, the freshness of the petioles was maintained by storing them below 4 °C in plastic bags. The length of the petioles varied between 35 to 55 cm. A distinctive/typical rhubarb petiole is shown in Figure 6–4. The rhubarb petiole is roughly uniform throughout its length, but a slight variation in cross-sectional shape is observed between the basal and apical locations.

Figure 6–4: A typical rhubarb stalk.

6.4.1 Measurement of Tissue Density

Cubes of parenchyma tissue were cut from the petioles using a potato chipper and a knife. The dimensions of the cubes were measured with digital calipers, and their weight was measured using a precise laboratory scale. Strips of collenchyma and combined collenchyma and parenchyma tissues were similarly cut, measured, and weighed. The densities of the tissues were measured for a large number of samples to obtain statistically significant results. Figure 6–5 shows a box and whisker plot of data from the density measurement of collenchyma, parenchyma, and whole petiole. The upper and lower boundaries of the box indicate upper (75^{th} percentile) and lower (25^{th} percentile) quartile, whereas the internal black line indicates the median data (density), and the thick white line represents the mean value (density). The lines extending vertically from the boxes, known as whiskers, illustrate the variability outside the upper and lower quartiles. The size of the box and

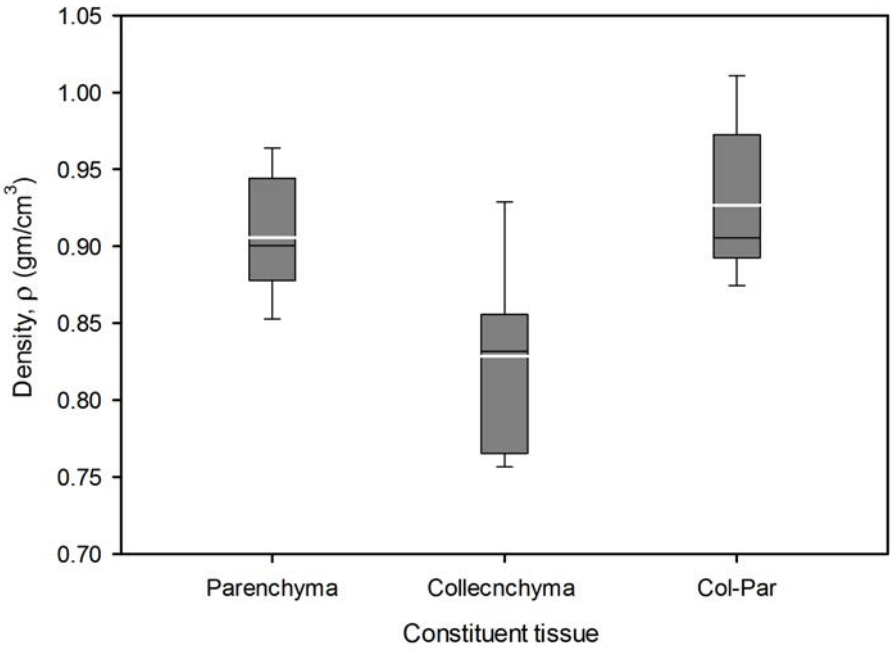

Figure 6–5: Experimental measurement of the density of the constituent tissue of the rhubarb petiole.

the spacing between the different parts of it indicate the dispersion/spread of the measured data (density). The densities of the collenchyma vary to a considerable amount in comparison with the parenchyma and complete tissues. The population size of the collenchyma samples was less when compared to the population size of other tissue types, which might causes the large dispersion. Apart from that difference, a variation in parenchyma density along the length of the petiole also was observed. The density of the parenchyma tissue is less dense in the apical location than in the basal location.

The mean densities of the tissues are as follows:

- Mean parenchyma tissue density = 0.903 (SD 0.04) gm/cm^3
- Mean collenchyma tissue density = 0.828 (SD 0.06) gm/cm^3
- Mean collenchyma-parenchyma tissue density = 0.93 (SD 0.05) gm/cm^3

6.4.2 Measurement of Flexural Stiffness of Rhubarb Petiole

To measure the flexural stiffness of the rhubarb petiole, 15 (whole) petioles were subjected to a three-point bending test by using the custom built apparatus shown in Figure 6–6. Samples were placed on aluminium supports with a gauge length of 287 mm, and force was applied to the center through a semi-annular probe. Samples were loaded using a hand crank, and care was taken to maintain a consistent speed throughout the test. Figure 6–6 demonstrates a three-point bending test using the in-house apparatus.

Figure 6–6: Three-point bending test of a rhubarb petiole using the apparatus built in-house.

After testing, a whole petiole was sampled at 5 points from basal to apical along its length for cross-sectional geometry. The height and width were measured using digital calipers, and hand-cut sections were imaged using a digital camera. The outline of each section was drawn and scaled in AutoCAD, which allowed us to calculate the geometric properties, such as area, A, and second moment of area, I_{xx}, that helped us calculate the flexural stiffness of the petioles. The box and whisker plot as shown in Figures 6–7 and 6–8 depict the distribution of area and I_{xx} of the rhubarb petioles along the length.

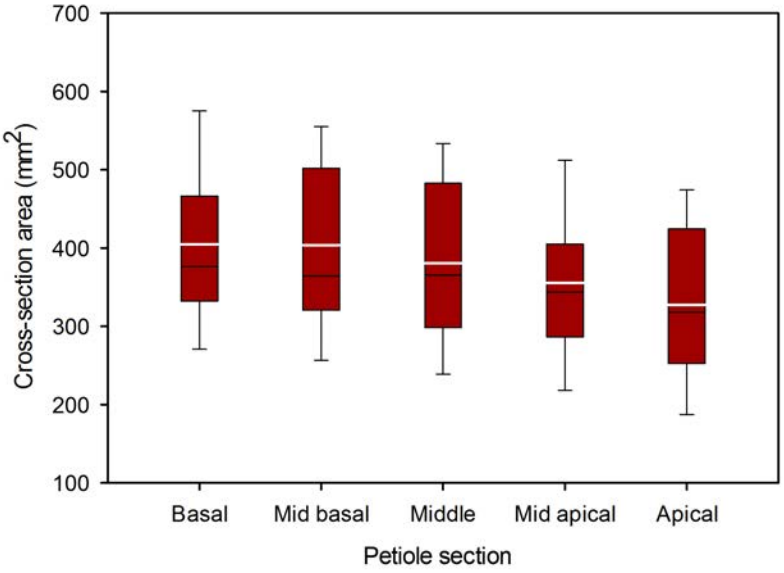

Figure 6–7: Experimental measurement of the lengthwise cross-sectional area of the rhubarb petioles used in the bending tests.

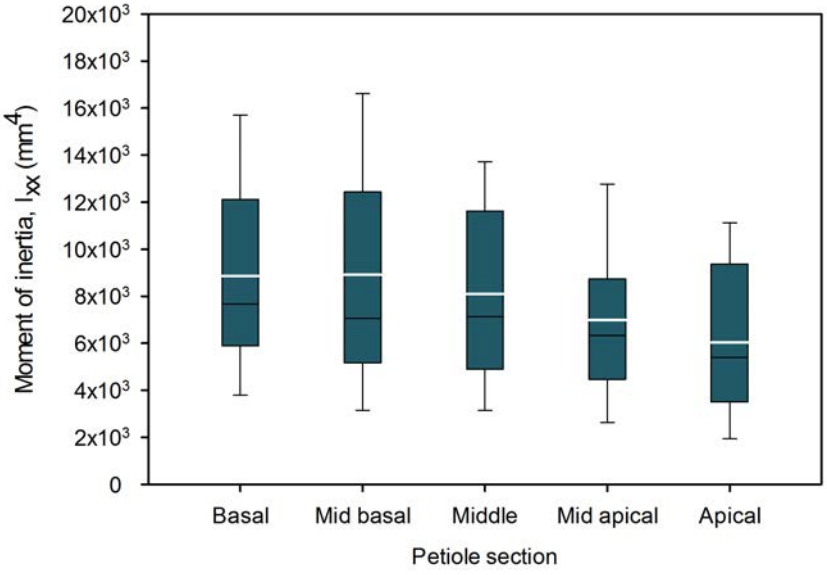

Figure 6–8: Experimental measurement of I_{xx} of the lengthwise cross-sectional shape of the rhubarb petioles in the bending tests.

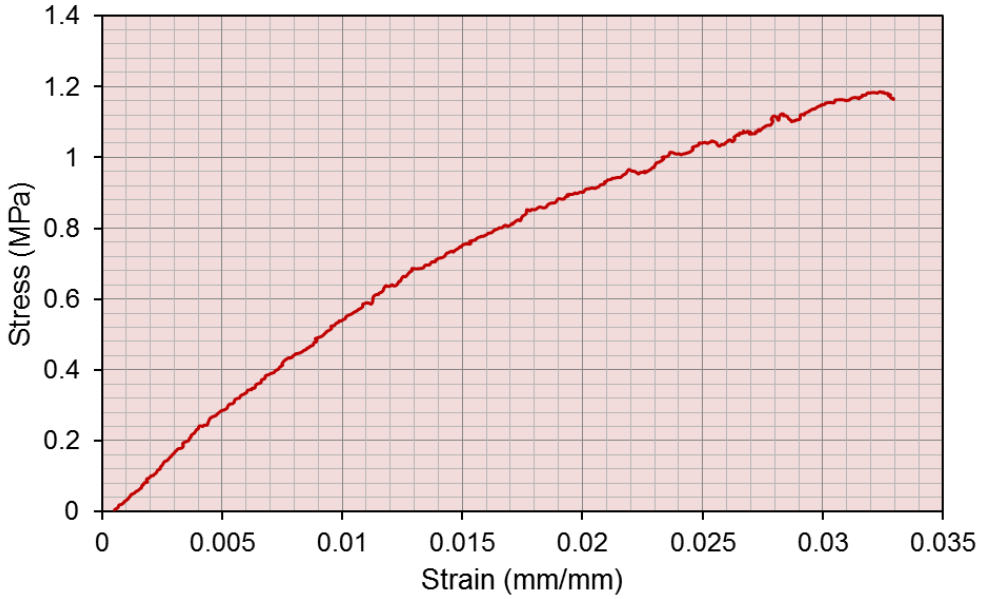

Figure 6–9: Experimental stress-strain diagram from the three-point bending test of a rhubarb petiole.

During the experiment, force and deflection were measured through a 10 lb load cell (Honeywell) and a linear potentiometer (Omega), respectively. Data was sampled and acquired at 100 Hz using an MTESTQUATTRO system from ADMET. The experimental stress and strain were calculated from the load-deflection by using the required geometrical properties determined by the CAD model. A distinctive stress-strain diagram is shown in Figure 6–9. It is to be noted that the applied loads were within the elastic limit. The experimental bending stiffness, EI, of the sample petioles were then obtained from the geometric properties and stress-strain plots.

6.4.3 Measurement of Torsional Stiffness of the Rhubarb Petiole

To measure the torsional stiffness of the rhubarb petiole, 15 (whole) petioles also were subjected to torsion tests using the apparatus built in-house as shown in Figure 6–10. The sample rhubarb stalks varied between 270 to 310 mm in length. Sample ends were fixed inside aluminium cylinders with cyanoacrylate glue (Loctite, UK) and epoxy resin (Scotch-Weld, 3M). One cylinder was held

in position, while the other was attached to a pulley. Torque was applied to the pulley using a hand crank, and care was taken to maintain a consistent speed throughout the test. Figure 6-9 shows the torsion test on the test bed.

Figure 6–10: Torsion test of a rhubarb petiole using the apparatus built in-house.

After testing, the whole petioles were similarly sampled at 5 points from basal to apical along their length for cross-sectional geometry. A similar procedure to the one used on the bending samples was followed to measure the geometric properties, area, A and torsional constant, J_T, of the petioles in torsion. The torsional constant was used to determine the torsional stiffness of the rhubarb petiole. The box and whisker plot as shown in Figures 6–11 and 6–12 illustrate the statistical distribution of area and J_T of the rhubarb petiole along the length.

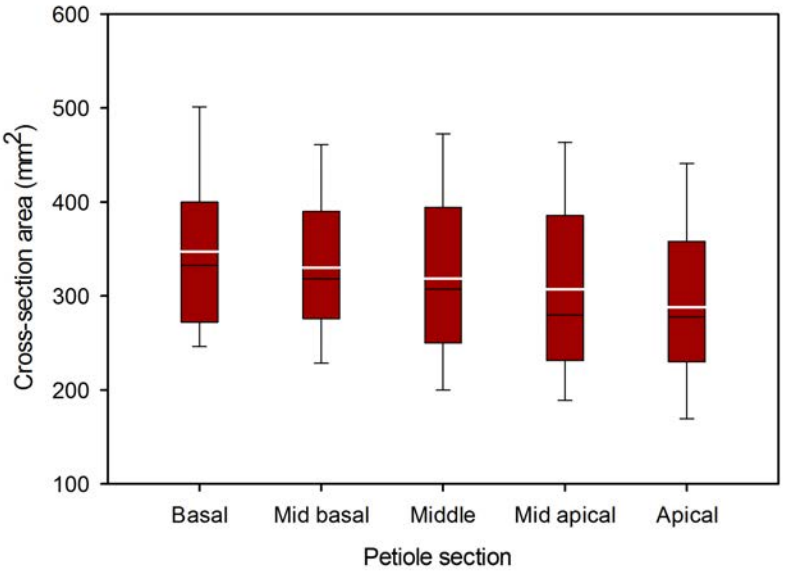

Figure 6–11: Experimental measurement of the lengthwise cross-sectional area of the rhubarb petioles used in the torsion tests.

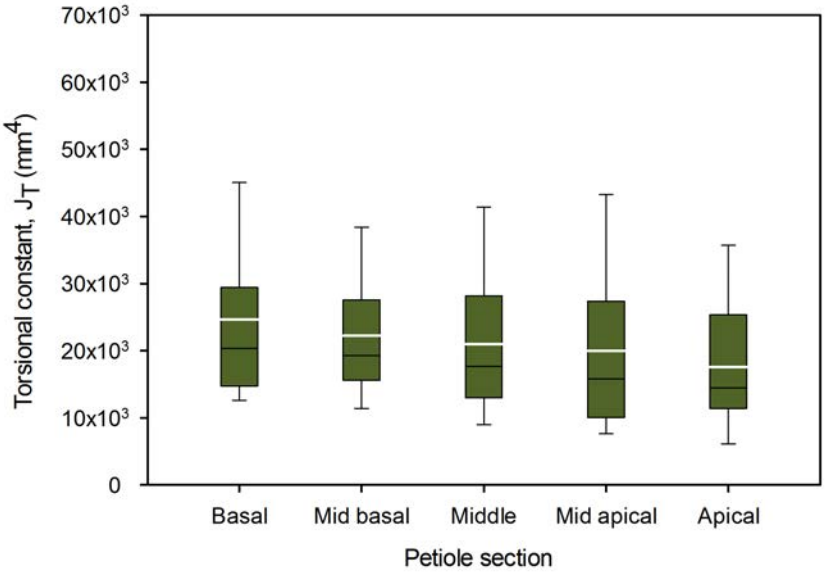

Figure 6–12: Experimental measurement of J_T of the lengthwise cross-sectional shape of the rhubarb petioles in the bending tests.

The force applied to the pulley line was measured using the 10 lb load cell, and the corresponding angle of deflection was measured using a touch-less rotary sensor (Novotechnik, Germany). Data were sampled and acquired at 100 Hz using the MTESTQUATTRO system from ADMET. The experimental torque was calculated from the applied load and plotted against the angle of twist as shown in Figure 6–13.

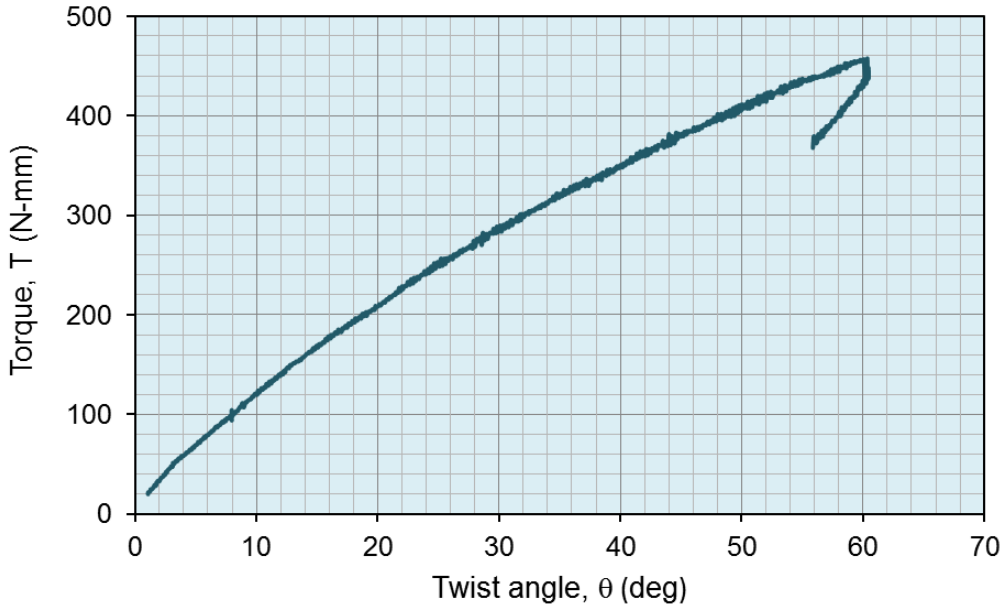

Figure 6–13: Experimental torque vs. angle of twist diagram from the torsion test of a rhubarb petiole.

6.4.4 Experimental Flexural and Torsional Stiffness of the Rhubarb Petiole

For both the flexural and torsional tests, while loading within the elastic range, the results show a linear stress-strain and Torque vs. twist angle variation (Figures 6–9 and 6–13), respectively. The experimental measurement of flexural stiffness, EI, and torsional rigidity, GJ_T, is used to determine the twist to bend ratio, EI/GJ. EI is the resistance to bending and GJ_T is the resistance to torsion of a structure. The dimensionless EI/GJ ratio indicates the relative torsional stiffness or twist-to-bend ratio of the rhubarb petiole.

Nature often strives to raise the ratio by forming grooved, flattened or some other non-circular cross-section in the stems and petioles. The experimental EI and GJ_T of the petioles are shown in Figure 6–14. A detailed sample wise plot also is described in section 6.5.4, the discussion about the computational results.

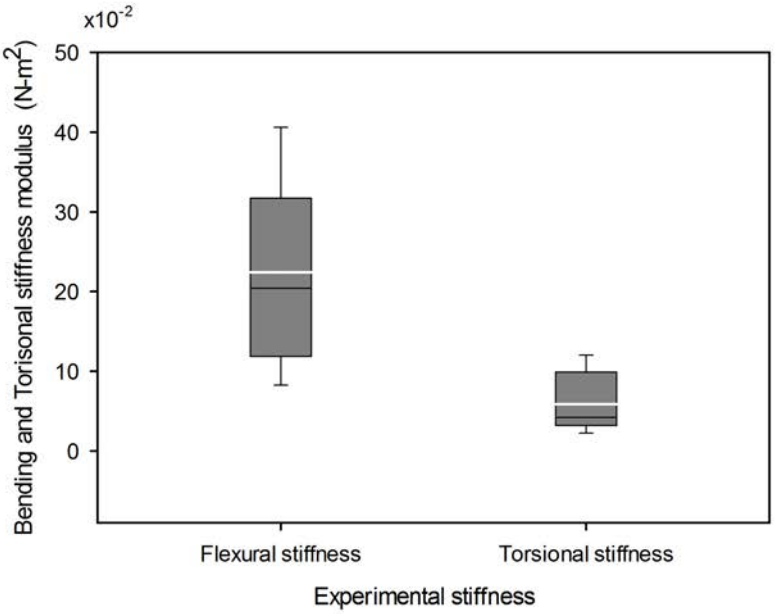

Figure 6–14: Experimental flexural and torsional stiffness.

6.5 Computational Results and Discussion

The effective flexural and torsional stiffness are computationally determined for the cross-sectional shapes at the locations shown in Figure 2–2 along the petiole length. The effective stiffness properties represent the overall outcome of the mechanical properties of the preceding orders of the structural hierarchy for the rhubarb petiole (Figure 1–1) that are considered in this work. The flexural and torsional stiffness are used to calculate the computational twist-to-bend ratio, which is compared to the experimental values. However, considering the two tissue (collenchyma and parenchyma) system, efficiency zones for both flexural and torsional domains can be proposed for all possible combinations of these two tissue types.

6.5.1 Generation of Cross-sectional Shapes of the Rhubarb Petiole

The Gielis superformula given by Equation (6.2) is used to capture the cross-sectional shape at the basal, middle, and apical locations of the *Rheum rhabarbarum* (rhubarb) petiole. In the computational analysis, the mid-basal and mid-apical locations are not considered because of their close resemblances with the basal and apical shapes, respectively. The values of the parameters of Equation (6.2) to obtain the shape contours are given in Table 6–1.

Table 6–1: Parameters used in Equation (6.2) [Gielis superformula] to plot the shape contours of the rhubarb petiole.

Lengthwise petiole location	m	n_1	n_2	n_3	a	b
Basal	8.0	2.9	3.1	2.9	0.76	1.1
Middle	7.7	2.8	4.1	2.3	0.76	1.1
Apical	7.8	2.5	3.0	3.5	0.90	1.3

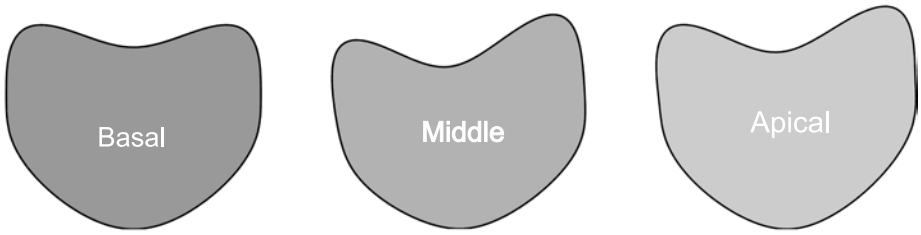

(a) near stem (b) middle (c) near leaf

Figure 6–15: Petiole cross-sections at different locations along the length.

The contours of the different cross-sectional shapes are mathematically captured and shown in Figure 6–15. The shape contours are fairly accurate for representing the cross-sectional shapes as shown in Figure 2–2. The shape contours are used to determine the computational flexural and torsional stiffness.

6.5.2 Effective Flexural Stiffness Map for Two Tissue System

In the computational model, the petiole is assumed to consist of two integrated tissues, collenchyma and parenchyma, although in reality, more than two tissues exist. In this analysis, each domain is created for a specific cross-section based on all possible combinations of the constituent tissues. The experimental bending (flexural) stiffness of the rhubarb petiole is expected to fall within this structural efficiency zone. Figures 6–16(a) to 6–16(c) show the flexural stiffness domains bounded by the limiting curve of the constituent tissue material. The change in domain due to cellularity is also shown in these figures.

Considering a tissue to be a homogeneous material can be informative; however, tissues are mostly cellular in nature. The thick (blue) solid lines in Figures 6–16(a) to 6–16(c) depict the boundary of the two-tissue (collenchyma and parenchyma) system, while considering both tissues to be homogeneous. The inherent cellularity of the constituent tissues is approximately represented

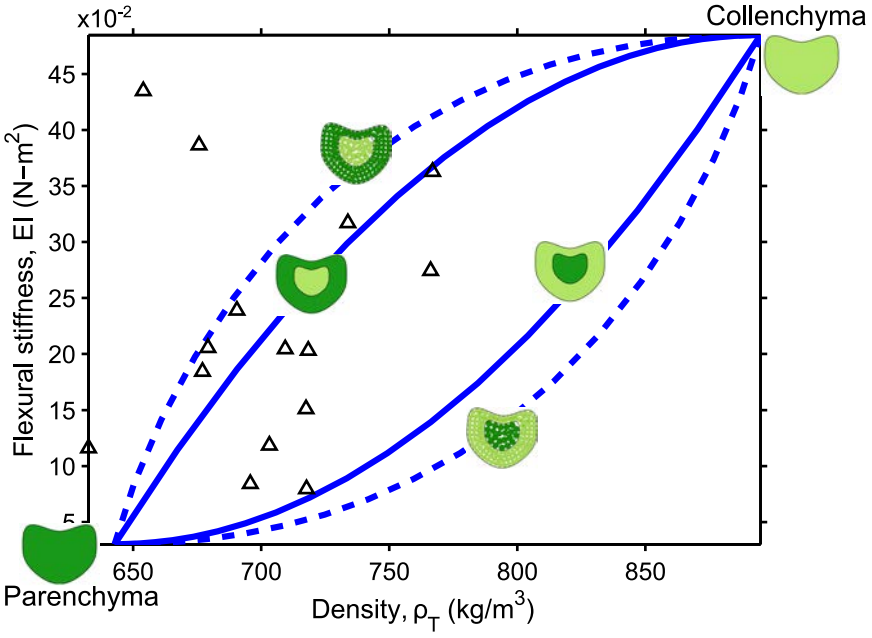

(a) Basal section

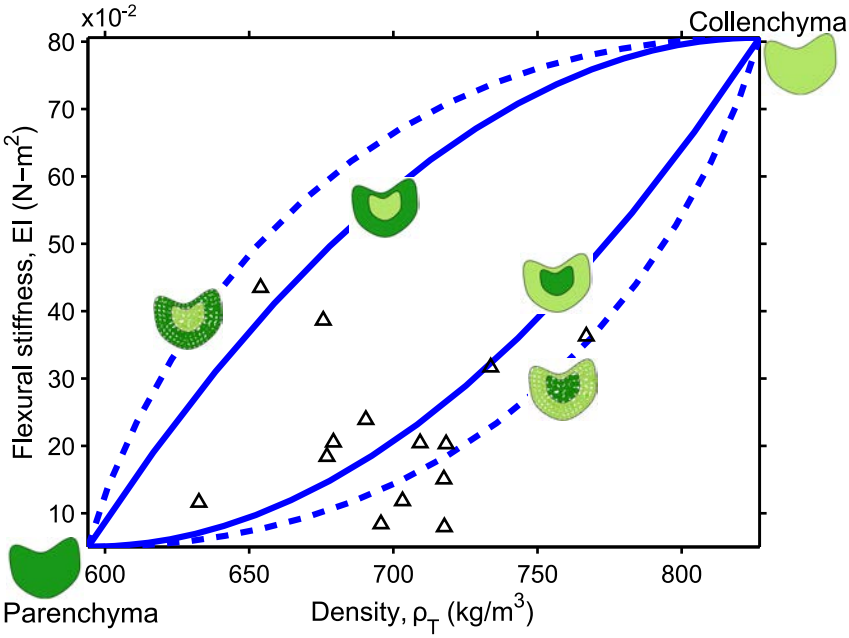

(b) Middle section

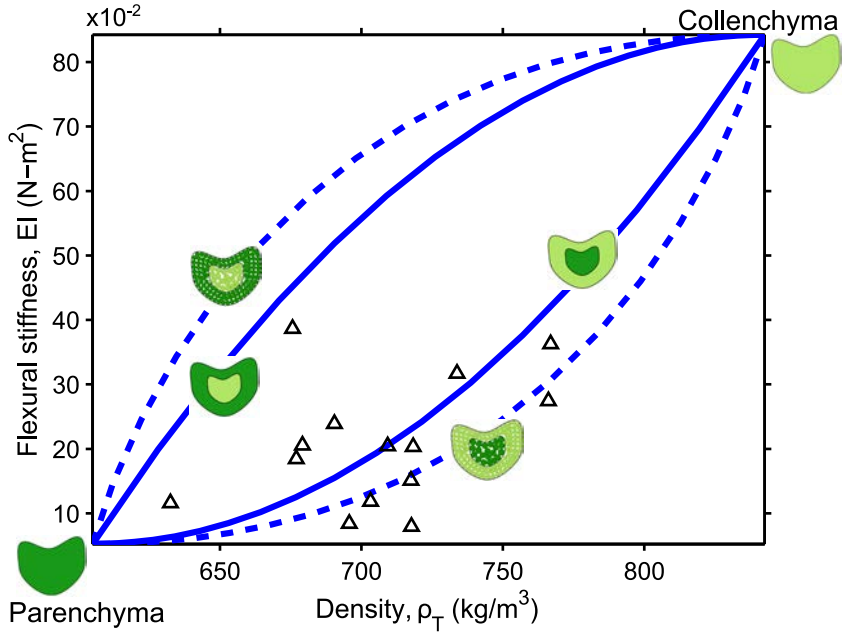

(c) Apical section

Figure 6–16: Flexural stiffness domain for the collenchyma-parenchyma tissues at the (a) basal, (b) middle, and (c) apical cross-sectional shape of the rhubarb petiole. Regions bounded by thick blue lines depict the domain with homogeneous tissue (solid blue) and the domain with cellular tissue (dashed blue). The upper triangles in the figure are experimental EI data from the bending test.

by the circular microstructure. The corresponding efficiency domain is expanded due to the structuring effect in the layered tissues, which is illustrated by the thick dashed (blue) lines in these figures.

The experimental bending stiffness shown by the upper triangles falls within the theoretical domain, although few data fell outside the domains. The variations of cross-sectional shapes and the inherent differences of volume and stiffness of constituent tissues of the sample petioles result in variations of experimental data. Therefore, the experimental EI values are a slightly scattered and a few values fall outside the domains. The domain with the cellular microstructure expectedly comprises more experimental EI values compared to the domain of the homogeneous tissue. It is observed that the domain of basal section contains more data points than the other two domains. This reflects the effect of cross-sectional shape. From the structural point of view, since the petiole acts as a cantilever, the maximum stress is developed at the basal location. The natural variation of the petiole's shape is to accommodate the applied load.

6.5.3 Effective Torsional Stiffness Map for Two Tissue System

The theoretical torsional stiffness domains similar to the domains of flexural stiffness at the three different locations of the rhubarb petiole are plotted in Figures 6–17(a) to 6–17(c). The thick (blue) solid lines in these figures illustrate the boundary of collenchyma and parenchyma system without any turgor pressure, while considering both tissues to be homogeneous. The effect of the inherent cellularity of the constituent tissues also is captured in the circular microstructure. The domain is expanded for the cellular microstructures compared to homogeneous tissues, which is shown by thick dashed (blue) lines in these figures (Figures 6–17[a] to 6–17[c]).

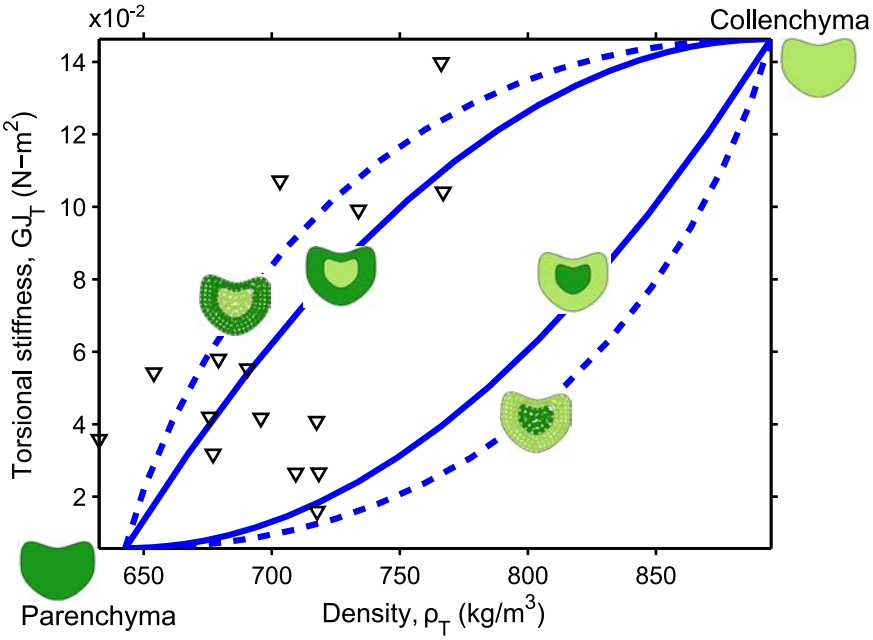

(a) Basal section

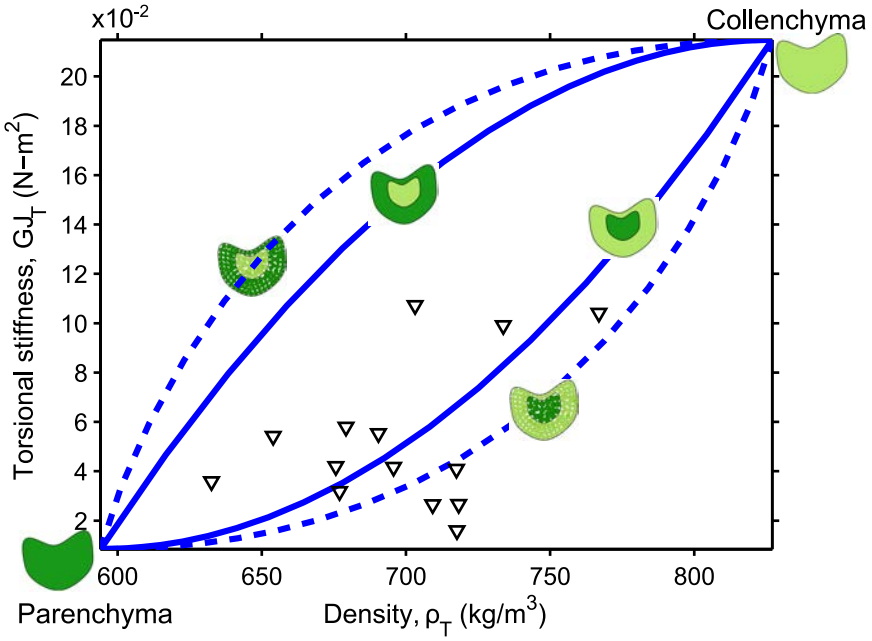

(b) Middle section

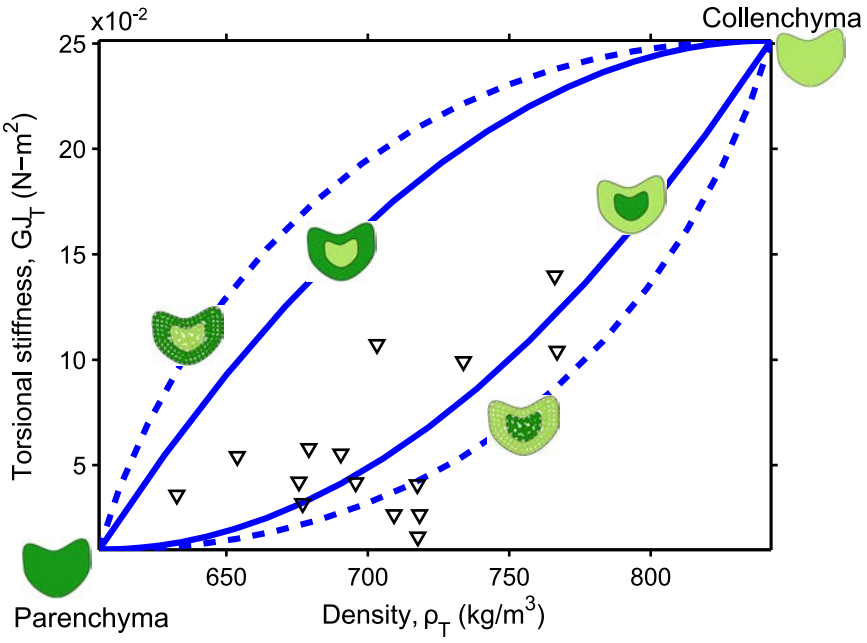

(c) Basal section

Figure 6–17: Torsional stiffness domain for the collenchyma-parenchyma tissues at the (a) basal, (b) middle, and (c) apical cross-sectional shape of the rhubarb petiole. Regions bounded by thick blue lines depict the domain with homogeneous tissue (solid blue) and the domain with cellular tissue (dashed blue). The lower triangles in the figure are experimental GJ data from the torsion test.

The experimental torsional stiffness shown by the lower triangles falls within the theoretical domain except few data. The domains of all the sections appear to contain the experimental GJ_T. However, the experimental results of the torsional stiffness lie closer to the boundary of collenchyma tissue for the mid and apical location, and can be explained in terms of the constitutive properties of the tissues. The collenchyma tissue is stronger in tension but not in twisting load. Since the collenchyma tissue is seen to the peripheral location, its stiffness appeared to influence the torsional rigidity of the petiole. Hence, the experimental results are closer to the region of collenchyma. Moreover, the torsional stiffness is also affected by the stiff outer epidermal layer, which has been ignored in the present computational model.

6.5.4 Comparison of Twist-to-Bend Ratio

Figure 6–18 shows the bar plot of the experimental EI/GJ_T for 15 samples of rhubarb petiole and the computational twist to bend ratio for the three shape contours, considering two constituent tissues. Since the variability of the experimental EI/GJ_T ratio is visible, a large number of experiments on petioles are therefore required to obtain a more accurate and statistically meaningful estimation. The average experimental twist to bend ratio of the rhubarb petiole is found to be 4.67 (SD 1.39), whereas the average computational EI/GJ_T ratio is approximately 4.04 (SD 0.65). It is evident that both shape and tissue (material) properties influence the EI/GJ_T ratio. Although expected to twist easily, permitting leaves to cluster and reduce their drag in high wind, the petioles must not bend too easily to work as cantilevers and to hold the leaf blades upright. Plants usually achieve high values of EI/GJ_T ratio by the concerted adjustment of material and geometry. Hence, the twist-to-bend ratio can be used to assess the efficiency of the cross-section shape in minimizing wind drag as well as in preventing the sag under gravity loads.

The computational model does not account for all of the tissue types normally present in a plant petiole. The tissues that have been ignored, despite contributing a narrow volume, may affect the mechanical properties in unpredicted ways. The effects of ignored tissues, especially epidermal layer, are expected to influence the experimental twist to bend ratio and result in a deviation. It is also assumed that a perfect bonding occurs between two layers, which may not be realistic for the petiole morphology. Moreover, the errors due to simplification of preceding hierarchies propagate from a lower to higher order hierarchy, and consequently, these errors accumulate at the last order of hierarchy.

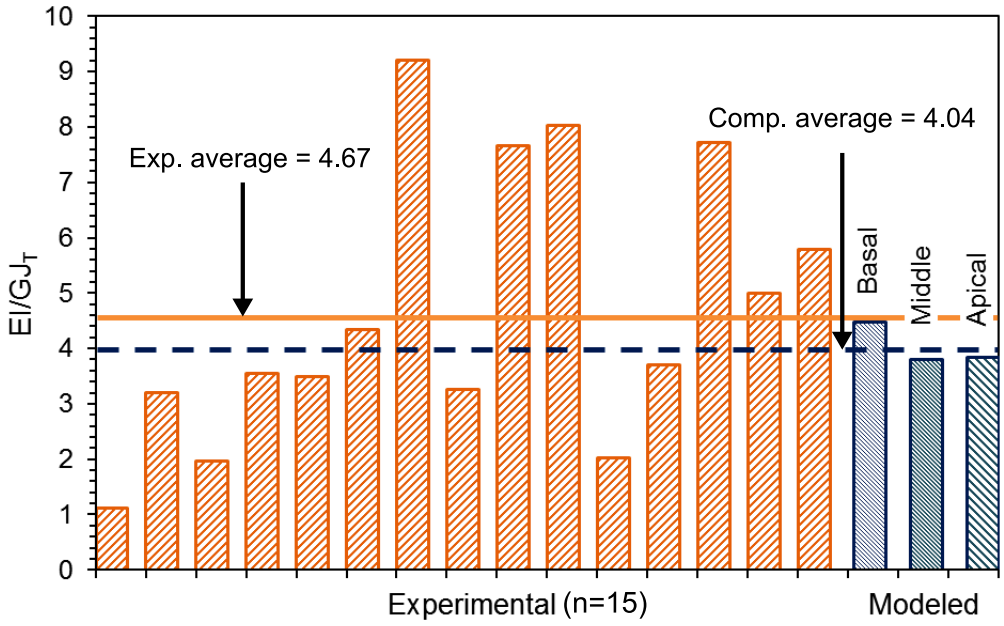

Figure 6–18: Comparison of experimental and computational twist-to-bend ratio of rhubarb petiole.

The material properties E and G are the cumulative outcome of the preceding orders, $n = 1$ to $n = 3$, of the hierarchy (Figure 1–1), whereas the geometric properties, I and G, of the shape denote the contribution of the topmost hierarchy. Without considering the material properties, the twist-to-bend ratio (I/J) of rhubarb petioles exhibit values just above 1 [66]. The contribution of material (tissue) anisotropy increases the twist-to-bend ratio to a considerable amount and reflects the influence of the multiple orders of the structural hierarchy observed in the petiole. Despite the simplification in modeling and the limitation in obtaining various experimental data at different hierarchical orders, the narrow difference between the experimental and computational twist to bend ratio depicts a comparative accuracy of the multiscale computational modeling approach presented in this thesis. The modeling approach and the associated experiments are, therefore, capable of capturing the contribution of the cross-sectional shape and the tissue on the petiole's twist-to-bend ratio.

The study of biological structure is essential to the innovation of novel biomimetic technology. The mechanisms used by the plants to grow flexible and resistant structure require to be unravelled to get a pathway to discover advanced engineering materials. The current study is a first step to understand how plants exploit the structural and functional integration at each order of hierarchhape morphology require the study that correlates biology and engineering modeling.

6.6 Summary

This chapter has discussed the flexural and torsional stiffness properties of the rhubarb petiole at the structural hierarchy. The mechanical properties are found to be contingent on the previous orders of hierarchy, since the stiffness of the constituent tissues considered in this chapter are obtained hierarchically. The effect of cross-sectional shape in determining the flexural and torsional stiffness also has confirmed. With respect to tissue properties, the cellular microstructure and the shape of the cross-section at the structural hierarchy play a substantial role in determining the compliance of the petiole. Described by the twist to bend ratio, the compliance of the petiole is higher when determined experimentally and slightly lower when measured by the computational model. The variation is obvious and is expected to have lower value for the computational model. However, the computational model is representative to characterize compliance behavior of the actual petiole and demonstrates an ability to do multiscale modeling of a petiole.

CHAPTER 7
Conclusion

7.1 Summary of Accomplishments

This work has used a multiscale method to model the mechanical properties—flexural and torsional stiffness—of a plant petiole in conjunction with experiments conducted at multiple length scale to validate the properties. The goal of such modeling is to capture the mechanical properties of the petiole by correlating its structural responses at multiple orders of the plant structural hierarchy via theoretical and computation models validated via experiments of plant tissue and organs. Experimentally determined cell and tissue properties are coupled with the mathematical models at various orders of hierarchy, such as sub-cellular, cellular, and tissue level, to compute the stiffness at each structural level; and the computed stiffness is validated with the stiffness obtained via experiments at the tissue and structural levels.

At the sub-cellular level, the cell wall has been modeled using the theory of a composite material to obtain the constitutive properties of the cell wall. A novel finite edge centroidal Voronoi tessellation (FECVT) algorithm has been developed and implemented to generate the virtual (geometric) tissues that represent the constituents of the petiole at the tissue level. The effective (homogenized) tissue properties have been obtained through the finite element analysis of the FECVT models. In contrast to the representative volume element (RVE) approach, the concept of the statistical volume element (SVE) has been implemented to compute the apparent tissue stiffness using finite element analysis. Such an approach is appropriate for natural cellular solids, whose microstructures are completely random with complex heterogeneity. The

effective stiffness of the constituent tissues has been used at the structural level with the shape morphology to compute the flexural and torsional stiffness of the petiole. Studies that have used the integration of multiple orders of hierarchy to determine the macrostructural properties of a plant petiole are currently lacking in the literature. The method implemented in this thesis is general, meaning that it can be applied to any plant and animal organs, and is capable of accounting for both the micro and macro architectural behaviors of these organs.

Plant biomimetics is a part of an innovative scientific field that uses biology as a model to create new energy production, storage and delivery systems, sensors, actuators, advanced materials and structures, electric systems, artificial intelligence, and computer systems. The challenge for a systematic knowledge transfer from nature to engineering is to integrate biology and engineering. Existing engineering technology fails to fully exploit the structural and functional integration found in plants at each length scale, from cell to whole organism. The conducted research can bridge the plant biology and engineering to develop novel bio-inspired material and structures. This research can help to develop fundamental knowledge of plant cellular biomechanics and its impact on the macroscopic mechanics of stems and petioles with the end goal of transferring this knowledge to the processing and design of compliant engineering structures and materials. Plant biomimetics for compliant structures is an efficient engineering design route to create high performance material systems that adapt to loads, reduce weight, and deploy when needed.

In *Chapter 3*, two orders of the structural hierarchy of plant have been examined. The cell wall belonging to the first order of hierarchy is modeled considering a fiber-reinforced composite material. The stiffness of the

parenchymal cell wall is approximated based on the composition of the wall constituents, their volume fractions, and elastic properties. Additionally, the effect of the fiber orientation angle is taken into account to predict the elastic properties of the collenchymatous cell wall. The constitutive properties are computed based on the generic composition of dicotyledonous plant cell wall with reasonable assumptions. The computational stiffness, however, would be more representative and closer to the actual wall stiffness if the experimentally determined volume fractions and MFA could be used in the mathematical model. Despite the limitation of acquiring the experimental data, the modelling approach provides a fundamental framework to relate the cell wall stiffness to its configuration.

In *Chapter 4*, the virtual (geometric) model of plant tissue has been generated. A novel algorithm, FECVT, is developed and efficiently applied to a variety of plant tissues, including *Arabidopsis*, *Philodendron melinonii*, and *Rheum rhabarbarum* (rhubarb), to construct the geometric models. The FECVT method is capable of capturing the tissue microstructure, and eliminating the semi-infinite edges at the boundary—an inherent drawback of conventional Voronoi tessellation. The generated models are statistically representative of the actual plant tissues. Therefore, this FECVT method can be applied to the geometric modeling of a microstructure of any shape with complex heterogeneity and graded cellularity.

In *Chapter 5*, the finite element analysis has been conducted on the FECVT models, generated in Chapter 4 coupled with the cell wall properties obtained in Chapter 3, to determine the homogenized/effective stiffness of the constituent tissues. Instead of using the classic approach of RVE to determine homogenized properties, a stochastic approach has been applied. Since the microstructures of the constituent tissues are highly random with clustered

higher area gradients, an RVE approach is not computationally efficient for capturing the complete randomness observed in the tissue. Therefore, the statistical volume elements are considered in contrast to a large-scale RVE to compute the homogenized properties with a reduced amount of computational effort. The cellular distribution in the FECVT models accounts for the lower values of the normalized effective stiffness of the respective models compared to the unit cell and randomly generated Voronoi models. The effective elastic properties of the constituent tissues are used to determine the flexural and torsional stiffness of the petiole.

In *Chapter 6*, the flexural and torsional stiffness and the corresponding twist-to-bend ratio based on the cross-sectional shape of the rhubarb petiole and its tissue properties have been computationally determined. The stiffness and the twist-to-bend ratio represent the cumulative effect of the shape morphology and micro-architectural effect of the tissues and cells. The stiffness and twist-to-bend ratio obtained via experiments validate the computed results. Therefore, the computational model demonstrates its ability to capture the multiscale characteristics and mechanics of plant petiole and other organs.

7.2 Original Contributions

The following are the original contributions of this thesis:

1. A multiscale modeling approach is presented to determine the flexural and torsional stiffness of the plant petiole (and stem) by integrating its hierarchical organization, which spans from the cell wall assembly to the overall structural geometry.
2. The parenchyma and collenchyma cell wall stiffness are determined by using the theory of composite material considering the volume fractions and microfibril orientation (assembly) of the respective cell wall constituents. The adopted approach is able to capture the anisotropic

cell wall stiffness, whereas in the existing literature, the wall stiffness mostly approximated to be isotropic.

3. A novel algorithm, FECVT, is used to capture the random distribution of cells in the tissue microstructures with complex heterogeneity. The method is capable of replicating any tissue microstructure with reasonable accuracy, resolving the inherent drawback of semi-infinite edges at the boundary. This algorithm can be applied to model any material microstructure.
4. The effective (homogenized) stiffness of the constituent tissues is determined by introducing the concept of statistical volume element. For a relatively simple cellular distribution, the existing approaches in literature consider RVE, which cannot determine the characteristic/representative stiffness of plant tissue.
5. The shape morphology is integrated with hierarchically determined constituent tissues' stiffness to computationally determine the flexural and torsional stiffness of plant organ. The approach is applied to determine the macrostructural response of rhubarb petiole.

7.3 Outlook to Future Research Paths

The hierarchical modeling approach used in this present work provides insight into the mechanics of plant organs at multiple orders of hierarchy. The methodology developed in this thesis allows the modeling of a wide variety of natural cellular solids. Moreover, this modeling approach can be extended to provide a more detailed examination of the mechanism of the micro and macro structure of the natural hierarchical cellular solids. The following are a few areas, in which the current research can be further extended or applied:

- Viscoelastic Modeling of the Cell Wall

  The cell wall has been modeled by assuming a linear elastic behavior

in the present work. The cell wall, however, often exhibits viscoelastic properties. The mechanical characterization of the cell wall will be more representative if the viscoelasticity is considered. Therefore, the micromechanical modeling of viscoelastic composites can be implemented to determine the wall stiffness in future.

- Modeling of Morphogenesis

  With respect to the living structures in nature, the structural properties of tissue and organism are affected by the differentiation and growth of the tissue and organism during development. During the growth process, the formation and reorganization of cells occur within the tissue. In the current work, the morphogenesis of tissue is not considered. With respect to the *in vivo* and in vitro experimental evidence of cell differentiation, a series of cellular distribution can be obtained for a period of time. The time dependent distribution of the cells can be modeled via the FECVT algorithm by determining the centroids of the cells at different time frame. Hence, the FECVT algorithm can be extended to investigate the temporal growth process and its impact on the structural properties of tissue thorough finite element analysis.

- Fluid Solid Interaction

  Turgor pressure plays an important role in controlling the structural properties of a plant. The effect of fluid structure interaction and fluid flow can be addressed in future endeavours. It is important because the properties of cell wall constituents change, for instance, hemicelluloses easily hydrolyze and swell; and consequently, the stiffness reduces due to the interaction with water. Therefore, a multi-physics analysis of the fluid structure interaction will provide a deeper understanding of the whole process.

- Biomimetic Application

  One of the aims of this research is to gain insight into the mechanics of the petiole structure at a multiple length scale, so these lessons could be applied to designing a bio-inspired compliant composite beam/structure displaying hierarchical structural features and cellular organization. The tissue architecture and structural mechanics in conjunction with the mechanical testing of petioles with altered cell organization will support the development of engineering structures with optimized structural properties. The knowledge gained through this research can be applied to designing a compliant biological beam like structure for boat masts, a wind turbine base, or other such structures that are subjected to both flexural and torsional loading. The stiffness of such a beam can be controlled by regulating the micro and macro architectures. A plant-based actuation system controlled by water content and turgor pressure is another area of application for bio-inspired design. As a whole, the methodology and the results of this current research provide a framework for plant-based biomimetics.

Appendix A

The elements of *transformed reduced compliance* matrix $[\bar{S}]$, shown in Equation (3.9c), are

$$\bar{S}_{11} = S_{11}m^4 + (2S_{12} + S_{66})m^2n^2 + S_{22}n^4$$

$$\bar{S}_{12} = (S_{11} + S_{22} - S_{66})m^2n^2 + S_{12}(m^4 + n^4)$$

$$\bar{S}_{16} = (2S_{11} - 2S_{12} - S_{66})m^3n - (2S_{22} - 2S_{12} - S_{66})mn^3$$

$$\bar{S}_{22} = S_{11}n^4 + (2S_{12} + S_{66})m^2n^2 + S_{22}m^4$$

$$\bar{S}_{26} = (2S_{11} - 2S_{12} - S_{66})mn^3 - (2S_{22} - 2S_{12} - S_{66})m^3n$$

$$\bar{S}_{66} = 2(2S_{11} + 2S_{22} - -4S_{12} - S_{66})m^2n^2 + S_{66}(m^4 + n^4)$$

where

$$S_{11} = 1/E_1$$

$$S_{12} = -\nu_{21}/E_2 = -\nu_{12}/E_1 = S_{21}$$

$$S_{22} = 1/E_2$$

$$S_{66} = 1/G_{12}$$

Appendix B

Pooled Variance and Mean

if n_1 = number of subjects in sample 1

n_2 = number of subjects in sample 2

$\bar{x}_1$ = mean of sample 1

$\bar{x}_2$ = mean of sample 2

$s_1^2 = \dfrac{\sum (x_1 - \bar{x}_1)^2}{n_1}$ = variance of sample 1

$s_2^2 = \dfrac{\sum (x_2 - \bar{x}_2)^2}{n_2}$ = variance of sample 2

σ_1 = standard deviation of sample 1, $\sigma_1 = \sqrt{s_1^2}$

σ_2 = standard deviation of sample 2, $\sigma_2 = \sqrt{s_2^2}$

For the conditions, $n_1 \neq n_2$, $\bar{x}_1 \neq \bar{x}_2$, and $s_1^2 \neq s_2^2$, the (composite) pooled mean, pooled variance, and pooled standard deviation for the two samples can respectively be expressed as

$$\bar{x} = \frac{n_1\bar{x}_1 + n_2\bar{x}_2}{n_1 + n_2}$$

$$s^2 = \frac{n_1\left\{s_1^2 + (\bar{x}_1 - \bar{x})^2\right\} + n_2\left\{s_2^2 + (\bar{x}_2 - \bar{x})^2\right\}}{n_1 + n_2}$$

$$\sigma = \sqrt{s^2}$$

where $\bar{x}$ is the composite or pooled mean, s^2 is the pooled variance, and $\sigma$is the corresponding pooled standard deviation [163].

Appendix C

The closed form expressions to determine the elastic properties of a periodic array of repeating hexagonal cells (hexagonal honeycomb) are described here. For the isotropic case, hexagonal unit cell as shown in figure 5–17(a), the relative density is given by

$$\frac{\rho^*}{\rho_s} = \frac{2}{\sqrt{3}} \left(\frac{t}{l} \right) \tag{C.1}$$

where ρ^* and ρ_s are the densities of the cellular material and of the solid cell wall material, respectively; t and l are the thickness and length of the cell wall, respectively. In terms of the thickness-to-length ratio, t/l, the two independent elastic constants of the unit cell are given by

$$\frac{E^*}{E_s} = \frac{4\sqrt{3}}{3} \left(\frac{t}{l} \right)^3 \left[\frac{1}{1 + (5.4 + 1.5\nu_s)\,(t/l)^2} \right] \tag{C.2}$$

$$\nu^* = \left[\frac{1 + (1.4 + 1.5\nu_s)\,(t/l)^2}{1 + (5.4 + 1.5\nu_s)\,(t/l)^2} \right] \tag{C.3}$$

where E^* and ν^* are the Young's modulus (effective modulus) and Poisson's ratio (effective Poisson's ratio) of the cellular material, respectively; and E_s and ν_s are the Young's modulus and Poisson's ratio of the solid cell wall material, respectively [12].

Appendix D

Boundary Approximation

The boundary integrals for a general boundary curve are defined by Equations (6.7) to (6.11) in Chapter 6. To compute the integrals numerically, the boundary needs to be discretized. The boundary is discretized by N number of nodes and intervals as shown in Figure 6-1. The integration is performed over those intervals, and summing up the sub-integrals yields the desired area and inertial quantities.

Let us assume first order polynomial interpolation over each boundary

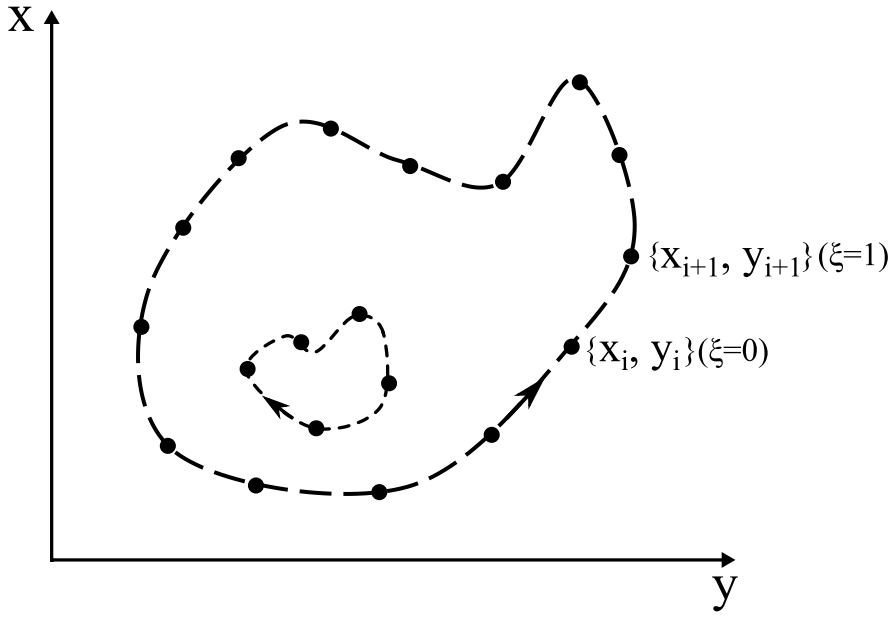

Figure D-1: Two dimensional arbitrary area with discretized interior and exterior boundary.

segment, where the i^{th} segment connects the nodes x_i and x_{i+1}. Interpolating the x-coordinate of the boundary linearly over that segment using a local coordinate ξ, yields,

$$x = x_i\phi_1(\xi) + x_{i+1}\phi_2(\xi) \qquad x_i < x < x_{i+1} \tag{D.1}$$

where $\phi_1(\xi) = 1 - \xi$ and $\phi_2(\xi) = \xi$ so that $\xi = 0$ corresponds to x_i, and $\xi = 1$ corresponds to x_{i+1}. Similarly for the y-coordinate, we have

$$y = y_i\phi_1(\xi) + y_{i+1}\phi_2(\xi) \qquad y_i < y < y_{i+1} \tag{D.2}$$

where $\phi_1(\xi) = 1 - \xi$ and $\phi_2(\xi) = \xi$ so that $\xi = 0$ corresponds to y_i, and $\xi = 1$ corresponds to y_{i+1}.

The differential quantities dx and dy can be obtained by differentiating Equations (D.1) and (D.2), respectively:

$$dx = x_i\frac{d\phi_1(\xi)}{d\xi} + x_{i+1}\frac{d\phi_2(\xi)}{d\xi} = x_{i+1} - x_i \tag{D.3}$$

$$dy = y_i\frac{d\phi_1(\xi)}{d\xi} + y_{i+1}\frac{d\phi_2(\xi)}{d\xi} = y_{i+1} - y_i \tag{D.4}$$

Let us consider the area integrals given in Equation (6.7). The first integral of Equation (6.7), area A_1 can be computed by summing the sub-integral over the N segments:

$$\begin{aligned} A_1 &= \sum_{i=1}^{N}\int_{i}^{i+1} x(\xi)dy(\xi) = \sum_{i=1}^{N}\left(x_i\int_{i}^{i+1}\phi_1(\xi)d(\xi) + x_{i+1}\int_{i}^{i+1}\phi_2(\xi)d(\xi)\right) \\ &= \frac{1}{2}\sum_{i=1}^{N}(x_{i+1} - x_i)(y_{i+1} - y_i) \\ &= \sum_{i=1}^{N} A_1^i \end{aligned} \tag{D.5}$$

where $A_1^i = \frac{1}{2}(x_{i+1} - x_i)(y_{i+1} - y_i)$ is the contribution of the i^{th} segment. Applying the similar procedure for the second and third area integrals, A_2 and A_2, respectively, gives

$$A_2^i = \frac{1}{2}(x_i - x_{i+1})(y_{i+1} + y_i) \tag{D.6}$$

$$A_3^i = \frac{1}{2}(x_i y_{i+1} - x_{i+1}y_i) \tag{D.7}$$

Although different forms of mathematical expressions are obtained for the corresponding area integrals, all formulations provide the same numeric result after summing all the sub-integrals over the N segments. Applying the similar procedure repeatedly for the other geometric properties given in Equations (6.8) to (6.11), we can derive the formulas for all the Equations as given in Table D-1. The generated formulas yield exact results for domains enclosed by piece wise straight segments.

Table D-1: Formulas for geometric quantities of a arbitrary polygon using 1st order polynomial.

Geometric Quantities	Formula
A	$\frac{1}{2}(x_i y_{i+1} - x_{i+1} y_i)$
A_x^i	$\frac{1}{6}(x_i - x_{i+1})(y_i^2 + y_i y_{i+1} + y_{i+1}^2)$
A_y^i	$-\frac{1}{6}(x_i^2 + x_i x_{i+1} + x_{i+1}^2)(y_i - y_{i+1})$
I_{xx}^i	$\frac{1}{12}(x_i - x_{i+1})(y_i^3 + y_i^2 y_{i+1} + y_i y_{i+1}^2 + y_{i+1}^3)$
I_{yy}^i	$-\frac{1}{12}(x_i^3 + x_i^2 x_{i+1} + x_i x_{i+1}^2 + x_{i+1}^3)(y_i - y_{i+1})$

A more accurate approximation can be obtained assuming 2nd order interpolating polynomial over each boundary segment. The Equation (D.1) and (D.2) will then be replaced by

$$x = x_{i_1}\phi_1(\xi) + x_i\phi_2(\xi) + x_{i+1}\phi_3(\xi) \qquad x_{i-1} < x < x_{i+1} \tag{D.8}$$

$$y = y_{i_1}\phi_1(\xi) + y_i\phi_2(\xi) + y_{i+1}\phi_3(\xi) \qquad y_{i-1} < y < y_{i+1} \tag{D.9}$$

where $\phi_1(\xi) = (1-2\xi)(1-\xi)$, $\phi_2(\xi) = 4\xi(1-\xi)$, and $\phi_3(\xi) = \xi(1-2\xi)$. Differential quantities dx and dy can be obtained by differentiating Equations

(D.8) and (D.9) and result in

$$\begin{aligned} dx &= x_{i-1}\frac{d\phi_1(\xi)}{d\xi} + x_i\frac{d\phi_2(\xi)}{d\xi} + x_{i+1}\frac{d\phi_3(\xi)}{d\xi} = x_{i+1} - x_i \\ &= (4\xi - 3)x_{i-1} - (8\xi - 4)x_i - (4\xi - 1)x_{i+1} \end{aligned} \tag{D.10}$$

$$dy = (4\xi - 3)y_{i-1} - (8\xi - 4)y_i - (4\xi - 1)y_{i+1} \tag{D.11}$$

Carrying out the integrations over each segment for each one of the integrals given in Equations (6.7) to (6.11), we get element formulas as shown in Table D-2. The 2$^{\text{nd}}$ order interpolation is sufficient to have desired level of accuracy. However, higher order interpolating polynomial can also be applied to the integrals to obtain more accurate element formulas, which would be lengthy and impractical to use. Formulas in Table D-1 and D-2 can be used to compute the required property for any given section, whose boundary is described by $x - y$ coordinates [164].

Table D-2: Formulas for geometric quantities of a arbitrary polygon using 2nd order polynomial.

Geometric Quantities	Formula
A	$\frac{1}{6}(4x_{i-1}y_i - 4x_{i+1}y_i - 4x_iy_{i-1} + x_{i+1}y_{i-1} + 4x_iy_{i+1} - x_{i-1}y_{i+1})$
A_x^i	$\frac{1}{30}(-2x_i(y_{i_1} - y_{i+1})(4y_i + 3y_{i-1} + 3y_{i+1}) +$ $x_{i+1}(-8y_i^2 + 2y_iy_{i-1} + y_{i-1}^2 - 6y_iy_{i+1} + y_{i-1}y_{i+1} + 10y_{i+1}^2) -$ $x_{i-1}(-8y_i^2 + 10y_{i-1}^2 + 2y_iy_{i+1} + y_{i+1}^2 + y_{i-1}(y_{i+1} - 6y_i)))$
A_y^i	$\frac{1}{30}(-8x_i^2(y_{i_1} - y_{i+1}) - x_{i-1^2}(-6y_i + 5y_{i-1} + y_{i+1}) +$ $2x_ix_{i+1}(-4y_i + y_{i-1} + 3y_{i+1}) + x_{i+1}^2(-6y_i + y_{i-1} + 5y_{i+1}) +$ $x_{i-1}(x_{i+1}(y_{i-1} - y_{i+1}) - 2x_i(-4y_i + 3y_{i-1} + y_{i+1})))$
I_{xx}^i	$\frac{1}{420}(-4x_i(y_{i_1} - y_{i+1})$ $(16y_i^2 + 12y_iy_{i-1} + 11y_{i-1}^2 + 12y_iy_{i+1} + 8y_{i-1}y_{i+1} + 11y_{i+1}^2) -$ $x_{i-1}(-64y_i^3 + 105y_{i-1}^3 + 16y_i^2y_{i+1} + 4y_iy_{i+1}^2 + y_{i+1}^3) +$ $y_{i-1}^2(-44y_i + 9y_{i+1}) + y_{i-1}(-48y_i^2 + 16y_iy_{i+1} - 3y_{i+1}^2)) +$ $x_{i+1}(-64y_i^3 - 9y_{i-1}^3 + y_{i-1}^2(4y_i - 3y_{i+1}) - 48y_i^2y_{i+1} -$ $44y_iy_{i+1}^2 + 105y_{i+1}^3 + y_{i-1}(16y_i^2 + 16y_iy_{i+1} + 9y_{i+1}^2)))$
I_{yy}^i	$\frac{1}{420}(x_{i-1}^3(44y_i - 35y_{i-1} - 9y_{i+1}) -$ $64xi^3(y_{i-1} - y_{i+1}) + 16x_i^2x_{i+1}(-4y_i + y_{i-1} + 3y_{i+1}) +$ $4x_i^2xi + 1(-12y_i + y_{i-1} + 11y_{i+1}) + x_{i+1}^3(-44y_i + 9y_{i-1} + 35y_{i+1}) +$ $x_{i-1}^2(3x_{i+1}(-4y_i + 3y_{i-1} + y_{i+1}) - 4x_i(-12y_i + 11y_{i-1} + y_{i+1})) -$ $x_{i-1}(-16x_ix_{i+1}(y_{i-1} - y_{i+1}) + 16x_i^2(-4y_i + 3y_{i-1} + y_{i+1}) +$ $3x_{i+1}^2(-4y_i + y_{i-1} + 3y_{i+1})))$

References

[1] S. Vogel, "Twist-to-bend ratios of woody structures," *Journal of Experimental Botany*, vol. 46, no. 8, pp. 981–985, 1995. [Online]. Available: http://jxb.oxfordjournals.org/content/46/8/981.abstract

[2] A. Ennos, H. C. Spatz, and T. Speck, "The functional morphology of the petioles of the banana, musa textilis," *Journal of Experimental Botany*, vol. 51, no. 353, pp. 2085–2093, 2000. [Online]. Available: http://jxb.oxfordjournals.org/content/51/353/2085.abstract

[3] A. R. Ennos, "The mechanics of the flower stem of the sedge carex acutiformis," *Annals of Botany*, vol. 72, no. 2, pp. 123–127, 1993. [Online]. Available: http://aob.oxfordjournals.org/content/72/2/123.abstract

[4] S. A. Etnier and S. Vogel, "Reorientation of daffodil(narcissus: Amaryllidaceae) flowers inwind: drag reduction andtorsional flexibility," *American Journal of Botany*, vol. 87, no. 1, pp. 29–32, 2000. [Online]. Available: http://www.amjbot.org/content/87/1/29.abstract

[5] N. A. Campbell and J. B. Reece, *Biology*, 8th ed. Benjamin Cummings, 2008.

[6] L. J. Gibson, "Biomechanics of cellular solids," *Journal of Biomechanics*, vol. 38, no. 3, pp. 377–399, 2005.

[7] P. Fratzl, I. Burgert, and H. S. Gupta, "On the role of interface polymers for the mechanics of natural polymeric composites," *Physical Chemistry Chemical Physics*, vol. 6, no. 24, pp. 5575–5579, 2004.

[8] H. Kha, S. Tuble, S. Kalyanasundaram, and R. E. Williamson, *Finite element analysis of plant cell wall materials*, ser. Advanced Materials Research. Stafa-Zurich: Trans Tech Publications Ltd, 2008, vol. 32, pp. 197–201.

[9] L. Salmen, "Micromechanical understanding of the cell-wall structure," *Comptes Rendus Biologies*, vol. 327, no. 9-10, pp. 873–880, 2004.

[10] L. J. Gibson and M. F. Ashby, *Cellular solids : structure and properties*, 2nd ed., ser. Cambridge solid state science series. Cambridge ; New York: Cambridge University Press, 1999.

[11] M. J. Silva and L. J. Gibson, "The effects of non-periodic microstructure and defects on the compressive strength of two-dimensional cellular solids,"

International Journal of Mechanical Sciences, vol. 39, no. 5, pp. 549–563, 1997.

[12] M. J. Silva, W. C. Hayes, and L. J. Gibson, "The effects of nonperiodic microstructure on the elastic properties of 2-dimensional cellular solids," *International Journal of Mechanical Sciences*, vol. 37, no. 11, pp. 1161–1177, 1995.

[13] S. Vogel, "Drag and flexibility in sessile organisms," *American Zoologist*, vol. 24, no. 1, pp. 37–44, 1984. [Online]. Available: http://icb.oxfordjournals.org/content/24/1/37.abstract

[14] ——, "Drag and reconfiguration of broad leaves in high winds," *Journal of Experimental Botany*, vol. 40, no. 8, pp. 941–948, 1989. [Online]. Available: http://jxb.oxfordjournals.org/content/40/8/941.abstract

[15] ——, "Living in a physical world xi. to twist or bend when stressed," *Journal of Biosciences*, vol. 32, pp. 643–655, 2007, 10.1007/s12038-007-0064-6. [Online]. Available: http://dx.doi.org/10.1007/s12038-007-0064-6

[16] V. Chickarmane, A. H. Roeder, P. T. Tarr, A. Cunha, C. Tobin, and E. M. Meyerowitz, "Computational morphodynamics: a modeling framework to understand plant growth," *Annual review of plant biology*, vol. 61, pp. 65–87, 2010.

[17] T. R. Faisal, N. Hristozov, A. D. Rey, T. L. Western, and D. Pasini, "Experimental determination of *Philodendron melinonii* and *Arabidopsis thaliana* tissue microstructure and geometric modeling via finite-edge centroidal voronoi tessellation," *Phys. Rev. E*, vol. 86, p. 031921, Sep 2012. [Online]. Available: http://link.aps.org/doi/10.1103/PhysRevE.86.031921

[18] T. R. Faisal, A. D. Rey, and D. Pasini, "A multiscale mechanical model for plant tissue stiffness," *Polymers*, vol. 5, no. 2, pp. 730–750, 2013. [Online]. Available: http://www.mdpi.com/2073-4360/5/2/730

[19] ——, "Hierarchical microstructure and elastic properties of leaf petiole tissue in philodendron melinonii," ser. MRS Proceedings, vol. 1420, no. mrsf11-1420-oo06-15. Cambridge University Press, 2011.

[20] H. X. Zhu, J. R. Hobdell, and A. H. Windle, "Effects of cell irregularity on the elastic properties of 2d voronoi honeycombs," *Journal of the Mechanics and Physics of Solids*, vol. 49, no. 4, pp. 857–870, 2001.

[21] D. Pasini, "Shape transformers for material and shape selection of lightweight beams," *Materials & Design*, vol. 28, no. 7, pp. 2071–2079, 2007.

[22] ——, "Modelling the micro- and macro-structure efficiencies of a compliant petiole beam," *Design and Nature Iv: Comparing Design in Nature with Science and Engineering*, vol. 114, pp. 107–117, 2008.

[23] S. Vogel, *Comparative Biomechanics: Life's Physical World.* Princeton University Press, 2003.

[24] U. Kutschera, "The growing outer epidermal wall: Design and physiological role of a composite structure," *Annals of Botany*, vol. 101, no. 5, pp. 615–621, 2008. [Online]. Available: http://aob.oxfordjournals.org/content/101/5/615.abstract

[25] N. C. Carpita and D. M. Gibeaut, "Structural models of primary-cell walls in flowering plants - consistency of molecular-structure with the physical-properties of the walls during growth," *Plant Journal*, vol. 3, no. 1, pp. 1–30, 1993.

[26] J. Fahlen and L. Salmen, "Pore and matrix distribution in the fiber wall revealed by atomic force microscopy and image analysis," *Biomacromolecules*, vol. 6, no. 1, pp. 433–438, 2005.

[27] D. Fengel and G. Wegener, *Wood: chemistry, ultrastructure, reactions.* Berlin: Walter de Gruyter, 1984.

[28] M. McNeil, A. G. Darvill, S. C. Fry, and P. Albersheim, "Structure and function of the primary-cell walls of plants," *Annual Review of Biochemistry*, vol. 53, pp. 625–663, 1984.

[29] K. J. Niklas, *Plant Biomechanics.* Chicago & London: The University of Chicago Press, 1992.

[30] S. Kerstens, W. F. Decraemer, and J. P. Verbelen, "Cell walls at the plant surface behave mechanically like fiber-reinforced composite materials," *Plant Physiology*, vol. 127, no. 2, pp. 381–385, 2001.

[31] A. Bergander and L. Salmen, "Cell wall properties and their effects on the mechanical properties of fibers," *Journal of Materials Science*, vol. 37, no. 1, pp. 151–156, 2002.

[32] I. Burgert and J. W. C. Dunlop, "Micromechanics of cell walls," in *Mechanical Integration of Plant Cells and Plants*, ser. Signaling and Communication in Plants, P. Wojtaszek, Ed. Springer Berlin Heidelberg, 2011, vol. 9, pp. 27–52. [Online]. Available: http://dx.doi.org/10.1007/978-3-642-19091-9-2

[33] K. J. Niklas, "Voigt and reuss models for predicting changes in young's modulus of dehydrating plant organs," *Annals of*

Botany, vol. 70, no. 4, pp. 347–355, 1992. [Online]. Available: http://aob.oxfordjournals.org/content/70/4/347.abstract

[34] W. Gindl, H. Gupta, T. Schoberl, H. Lichtenegger, and P. Fratzl, "Mechanical properties of spruce wood cell walls by nanoindentation," *Applied Physics A: Materials Science & Processing*, vol. 79, pp. 2069–2073, 2004, 10.1007/s00339-004-2864-y. [Online]. Available: http://dx.doi.org/10.1007/s00339-004-2864-y

[35] W. Gindl and T. Schöberl, "The significance of the elastic modulus of wood cell walls obtained from nanoindentation measurements," *Composites Part A: Applied Science and Manufacturing*, vol. 35, no. 11, pp. 1345 – 1349, 2004. [Online]. Available: http://www.sciencedirect.com/science/article/pii/S1359835X04001149

[36] I. Cave, "The anisotropic elasticity of the plant cell wall," *Wood Science and Technology*, vol. 2, pp. 268–278, 1968. [Online]. Available: http://dx.doi.org/10.1007/BF00350273

[37] ——, "Theory of x-ray measurement of microfibril angle in wood. part 1. the condition for reflection x-ray diffraction by materials with dibre type symmetry," *Wood Science and Technology*, vol. 31, pp. 143–152, 1997. [Online]. Available: http://dx.doi.org/10.1007/BF00705881

[38] B. R. D. R. M. J. C. Cown, D. J., "Wood density and microfibril angle in 10 pinus 23 radiata clones: Distribution and influence on product performance." *New Zeland Joural of Forestry Science*, vol. 34, pp. 293–315, 2004.

[39] Y. K. N. R. F. Y. Hirakawa, Y., "The effects of s2 microfibril angles 24 of latewood tracheids and densities on modulus of elasticity variations of sugi tree 25 (cryptomeria japonica) logs." *Mokuzai Gakkaishi*, vol. 43, pp. 717–724, 1997.

[40] S. Ghosh, K. Lee, and S. Moorthy, "Two scale analysis of heterogeneous elastic-plastic materials with asymptotic homogenization and voronoi cell finite element model," *Computer Methods in Applied Mechanics and Engineering*, vol. 132, no. 1-2, pp. 63–116, 1996.

[41] T. R. Faisal, E. M. Khalil Abad, N. Hristozov, and D. Pasini, "The impact of tissue morphology, cross-section and turgor pressure on the mechanical properties of the leaf petiole in plants," *Journal of Bionic Engineering*, vol. 7, Supplement, no. 0, pp. S11–S23, 2010.

[42] K. Li, X. L. Gao, and G. Subhash, "Effects of cell shape and cell wall thickness variations on the elastic properties of two-dimensional cellular solids," *International Journal of Solids and Structures*, vol. 42, no. 5-6, pp. 1777–1795, 2005.

[43] A. Okabe, B. Boots, K. Sugihara, and S. N. Chiu, *Spatial Tessellations: Concepts and Applications of Voronoi Diagrams*, 2nd ed. John Wiley & Sons Ltd, 2000.

[44] J. A. Blackman and P. A. Mulheran, "Scaling behavior in submonolayer film growth: A one-dimensional model," *Physical Review B*, vol. 54, no. 16, pp. 11 681–11 692, 1996.

[45] D. L. Gonzalez, A. Pimpinelli, and T. L. Einstein, "Spacing distribution functions for the one-dimensional point-island model with irreversible attachment," *Physical Review E*, vol. 84, no. 1, p. 011601, 2011.

[46] G. Cailletaud, S. Forest, D. Jeulin, F. Feyel, I. Galliet, V. Mounoury, and S. Quilici, "Some elements of microstructural mechanics," *Computational Materials Science*, vol. 27, no. 3, pp. 351–374, 2003.

[47] K. Hussain, E. R. De los Rios, and A. Navarro, "A two-stage micromechanics model for short fatigue cracks," *Engineering Fracture Mechanics*, vol. 44, no. 3, pp. 425–436, 1993.

[48] M. Mattea, M. J. Urbicain, and E. Rotstein, "Computer model of shrinkage and deformation of cellular tissue during dehydration," *Chemical Engineering Science*, vol. 44, no. 12, pp. 2853–2859, 1989.

[49] D. F. P. E. Roudot, A. C., "Simulation of a penetrometric test on apples using voronoi-delaunay tessellation," *Food structure*, vol. 9, no. 3, pp. 215–222, 1990.

[50] H. K. Mebatsion, P. Verboven, Q. T. Ho, F. Mendoza, B. E. Verlinden, T. A. Nguyen, and B. M. Nicolai, "Modelling fruit microstructure using novel ellipse tessellation algorithm," *Cmes-Computer Modeling in Engineering & Sciences*, vol. 14, no. 1, pp. 1–14, 2006.

[51] H. K. Mebatsion, P. Verboven, Q. T. Ho, B. E. Verlinden, and B. M. Nicolai, "Modelling fruit (micro)structures, why and how?" *Trends in Food Science & Technology*, vol. 19, no. 2, pp. 59–66, 2008.

[52] R. Ntenga and A. Beakou, "Structure, morphology and mechanical properties of rhectophyllum camerunense (rc) plant-fiber. part i: Statistical description and image-based reconstruction of the cross-section," *Computational Materials Science*, vol. 50, no. 4, pp. 1442–1449, 2011.

[53] A. Beakou and R. Ntenga, "Structure, morphology and mechanical properties of rhectophyllum camerunense (rc) plant fiber. part ii: Computational homogenization of the anisotropic elastic properties," *Computational Materials Science*, vol. 50, no. 4, pp. 1550–1558, 2011.

[54] L. J. Gibson and M. F. Ashby, "The mechanics of 3-dimensional cellular materials," *Proceedings of the Royal Society of London Series a-Mathematical Physical and Engineering Sciences*, vol. 382, no. 1782, pp. 43–59, 1982.

[55] A. Fazekas, R. Dendievel, L. Salvo, and Y. Brechet, "Effect of microstructural topology upon the stiffness and strength of 2d cellular structures," *International Journal of Mechanical Sciences*, vol. 44, no. 10, pp. 2047–2066, 2002.

[56] A. P. Roberts and E. J. Garboczi, "Elastic moduli of model random three-dimensional closed-cell cellular solids," *Acta Materialia*, vol. 49, no. 2, pp. 189–197, 2001.

[57] M. Ostoja-Starzewski, "Micromechanics as a basis of random elastic continuum approximations," *Probabilistic Engineering Mechanics*, vol. 8, no. 2, pp. 107 – 114, 1993. [Online]. Available: http://www.sciencedirect.com/science/article/pii/026689209390004F

[58] M. Ostoja-Starzewski and J. Schulte, "Bounding of effective thermal conductivities of multiscale materials by essential and natural boundary conditions," *Phys. Rev. B*, vol. 54, pp. 278–285, Jul 1996. [Online]. Available: http://link.aps.org/doi/10.1103/PhysRevB.54.278

[59] M. Ostoja-Starzewski, "Random field models of heterogeneous materials," *International Journal of Solids and Structures*, vol. 35, no. 19, pp. 2429 – 2455, 1998. [Online]. Available: http://www.sciencedirect.com/science/article/pii/S0020768397001443

[60] S. A. Etnier, "Flexural and torsional stiffness in multi-jointed biological beams," *The Biological Bulletin*, vol. 200, no. 1, pp. 1–8, 2001. [Online]. Available: http://www.biolbull.org/content/200/1/1.abstract

[61] ——, "Twisting and bending of biological beams: Distribution of biological beams in a stiffness mechanospace," *The Biological Bulletin*, vol. 205, no. 1, pp. 36–46, 2003. [Online]. Available: http://www.biolbull.org/content/205/1/36.abstract

[62] K. J. Niklas, "The mechanical roles of clasping leaf sheaths: Evidence from arundinaria tecta (poaceae) shoots subjected to bending and twisting forces," *Annals of Botany*, vol. 81, no. 1, pp. 23–34, 1998.

[63] J. G. J. Wainwright, S. A. Biggs. W.D. Currey, *Mechanical Design in Organisms*. Princeton University Press, 1982.

[64] J. Gielis, "A generic geometric transformation that unifies a wide range of natural and abstract shapes," *American Journal of Botany*, vol. 90, no. 3, pp. 333–338, 2003.

[65] M. A. R. Koehl, "Effects of sea anemones on the flow forces they encounter," *The Journal of Experimental Biology*, vol. 69, no. 1, pp. 87–105, 1977. [Online]. Available: http://jeb.biologists.org/content/69/1/87.abstract

[66] D. Pasini, "On the biological shape of the polygonaceae rheum rhabarbarum petiole," *Journal of Design & Nature and Ecodynamics*, vol. 3, no. 1, p. 25, 2008.

[67] M. F. Ashby, *Materials Selection in Mechanical Design*, 3rd ed. Elsevier Butterworth-Heinemann, 2005.

[68] B. A. Bodig, J.; Jayne, *Mechanics of wood and wood composites*, 2nd ed. NY: Krieger Pub Co, May 1993.

[69] P. P. Gillis, "Effect of hydrogen bonds on the axial stiffnes of crystalline native cellulose," *Journal of Polymer Science Part A-2: Polymer Physics*, vol. 7, no. 5, pp. 783–794, 1969. [Online]. Available: http://dx.doi.org/10.1002/pol.1969.160070504

[70] I. Sakurada and K. Kaji, "Relation between the polymer conformation and the elastic modulus of the crystalline region of polymer," *Journal of Polymer Science Part C: Polymer Symposia*, vol. 31, no. 1, pp. 57–76, 1970. [Online]. Available: http://dx.doi.org/10.1002/polc.5070310108

[71] I. Sakurada, Y. Nukushina, and T. Ito, "Experimental determination of the elastic modulus of crystalline regions in oriented polymers," *Journal of Polymer Science*, vol. 57, no. 165, pp. 651–660, 1962. [Online]. Available: http://dx.doi.org/10.1002/pol.1962.1205716551

[72] I. Satcurada, T. Ito, and K. Nakamae, "Elastic moduli of the crystal lattices of polymers," in *Journal of Polymer Science Part C: Polymer Symposia*, vol. 15, no. 1. Wiley Online Library, 1967, pp. 75–91.

[73] K. Tashiro and M. Kobayashi, "Theoretical evaluation of three-dimensional elastic constants of native and regenerated celluloses: role of hydrogen bonds," *Polymer*, vol. 32, no. 8, pp. 1516 – 1526, 1991. [Online]. Available: http://www.sciencedirect.com/science/article/pii/003238619190435L

[74] W. Cousins, "Young's modulus of hemicellulose as related to moisture content," *Wood Science and Technology*, vol. 12, no. 3, pp. 161–167, 1978, cited By (since 1996) 70.

[75] W. J. Cousins, "Elastic modulus of lignin as related to moisture content," *Wood Science and Technology*, vol. 10, pp. 9–17, 1976, 10.1007/BF00376380. [Online]. Available: http://dx.doi.org/10.1007/BF00376380

[76] W. J. Cousins, R. W. Armstrong, and W. H. Robinson, "Young's modulus of lignin from a continuous indentation test," *Journal of Materials Science*, vol. 10, pp. 1655–1658, 1975, 10.1007/BF00554925. [Online]. Available: http://dx.doi.org/10.1007/BF00554925

[77] M. L. Fishman, D. R. Coffin, J. J. Unruh, and T. Ly, "Pectin/starch/glycerol films: Blends or composites?" *Journal of Macromolecular Science, Part A*, vol. 33, no. 5, pp. 639–654, 1996. [Online]. Available: http://www.tandfonline.com/doi/abs/10.1080/10601329608010884

[78] T. Giancone, E. Torrieri, P. D. Pierro, L. Mariniello, M. Moresi, R. Porta, and P. Masi, "Role of constituents on the network formation of hydrocolloid edible films," *Journal of Food Engineering*, vol. 89, no. 2, pp. 195 – 203, 2008. [Online]. Available: http://www.sciencedirect.com/science/article/pii/S0260877408001957

[79] T. Ichibouji, T. Miyazaki, E. Ishida, M. Ashizuka, A. Sugino, C. Ohtsuki, and K. Kuramoto, "Evaluation of apatite-forming ability and mechanical property of pectin hydrogels," *Journal of the Ceramic Society of Japan*, vol. 116, no. 1349, pp. 74–78, 2008.

[80] LiuLiu, C.-K. Liu, M. L. Fishman, and K. B. Hicks, "Composite films from pectin and fish skin gelatin or soybean flour protein," *Journal of Agricultural and Food Chemistry*, vol. 55, no. 6, pp. 2349–2355, 2007. [Online]. Available: http://pubs.acs.org/doi/abs/10.1021/jf062612u

[81] S. Garkhail, R. Heijenrath, and T. Peijs, "Mechanical properties of natural-fibre-mat-reinforced thermoplastics based on flax fibres and polypropylene," *Applied Composite Materials*, vol. 7, no. 5-6, pp. 351–372, 2000.

[82] C. Gerdeen, H. Lord, and R. Rorrer, *Engineering Design: With Polymers and Composites*, ser. Engineering Design with Polymers and Composites. CRC/Taylor & Francis, 2006. [Online]. Available: http://books.google.ca/books?id=Lqml0RJHrMAC

[83] J. McCabe and A. Walls, *Applied Dental Materials*, J. McCabe and A. Walls, Eds. Wiley, 2009. [Online]. Available: http://books.google.ca/books?id=vfxsE_o_7BcC

[84] T. Huber, N. Graupner, and J. Müssig, "As tough as it is delicious? a mechanical and structural analysis of red rhubarb (rheum rhabarbarum)," *Journal of materials science*, vol. 44, no. 15, pp. 4195–4199, 2009.

[85] W. L. Schrader. (2008) Rhubarb production in california. Division of Agriculture and Natural Resources, University of California. [Online]. Available: http://anrcatalog.ucdavis.edu/

[86] S. E. Ruzin, *Plant Microtechnique & Microscopy*. New York: Oxford University Press, 1999.

[87] I. Cave, "Theory of x-ray measurement of microfibril angle in wood. part 2. the diffraction diagram x-ray diffraction by materials with fibre type symmetry," *Wood Science and Technology*, vol. 31, pp. 225–234, 1997. [Online]. Available: http://dx.doi.org/10.1007/BF00702610

[88] L. Donaldson, "Microfibril angle: Measurement, variation and relationships–a review," *IAWA journal*, vol. 29, no. 4, p. 345, 2008.

[89] I. Burgert and P. Fratzl, "Plants control the properties and actuation of their organs through the orientation of cellulose fibrils in their cell walls," *Integrative and Comparative Biology*, 2009. [Online]. Available: http://icb.oxfordjournals.org/content/early/2009/05/22/icb.icp026.abstract

[90] J. R. Barnett and V. A. Bonham, "Cellulose microfibril angle in the cell wall of wood fibres," *Biological reviews*, vol. 79, no. 2, pp. 461–472, 2007.

[91] K. J. Niklas and H. Spatz, *Plant Physics*. University of Chicago Press, 2012.

[92] O. Leroux, "Collenchyma: a versatile mechanical tissue with dynamic cell walls," *Annals of Botany*, vol. 110, no. 6, pp. 1083–1098, 2012. [Online]. Available: http://aob.oxfordjournals.org/content/110/6/1083.abstract

[93] P. A. Roelofsen, *The plant cell wall In: Von Lindbauer K. ed. Handbuch der Pflanzenanatomie*, Berlin, 1959.

[94] T. Kerr and I. W. Bailey, "The cambium and its derivative tissue. x. structure, optical properties and chemical composition of the so-called middle lamella," *Journal of the Arnold Arboretum*, vol. 15, pp. 329–349, 1934.

[95] M. Beer and G. Setterfield, "Fine structure in thickened primary walls of collenchyma cells of celery petioles," *American Journal of Botany*, vol. 45, no. 7, pp. pp. 571–580, 1958. [Online]. Available: http://www.jstor.org/stable/2439583

[96] S. C. Chafe, "The fine structure of the collenchyma cell wall," *Planata*, vol. 90, no. 1, pp. 12–21, 1969. [Online]. Available: http://dx.doi.org/10.1007/BF00389292

[97] G. P. Gupta, *Plant Cell Biology*, 1st ed. Discovery Publishing House Pvt. Ltd., 2004.

[98] J. C. Roland, "Infrastructure des membranes du collenchyme," *CR Acad. Sci., Paris*, vol. 259, pp. 4331–4334, 1964.

[99] ——, "Edification et infrastructure de la membrane collenchymateuse . son remaniement lors de la sclerification," *Comptes Rendus Hebdomadaires Des Seances De L Academie Des Sciences*, vol. 260, no. 3, pp. 950–953, 1965.

[100] ——, "Organisation de la membrane paraplasmique du collenchyme," *Journal of Microscopy-Oxford*, vol. 5, no. 3, pp. 323–348, 1966, iSI Document Delivery No.: 81786 Times Cited: 26 Cited Reference Count: 36 Roland, jc Blackwell science ltd Oxford.

[101] C. Stevens and J. Müssig, *Industrial Applications of Natural Fibres: Structure, Properties and Technical Applications*. John Wiley & Sons Ltdy, 2010.

[102] K. Esau, *Plant Anatomy*. New York: John Wiley & Sons, Inc., 1965.

[103] T. Goodwin and E. Mercer, "The plant cell wall," *Introduction to plant biochemistry*, pp. 55–91, 1983.

[104] R. C. Salisbury, F.B., *Plant Physiology*. Belmont, CA: Wadsworth, Inc, 1992, ch. Plant Physiology and Plant Cells, pp. 3–26.

[105] M. K. Weibel, "Parenchymal cell cellulose and related materials, and a method of producing the same," Nov. 25 1987, eP Patent 0,102,829.

[106] S. Vorwerk, S. Somerville, and C. Somerville, "The role of plant cell wall polysaccharide composition in disease resistance," *Trends in Plant Science*, vol. 9, no. 4, pp. 203 – 209, 2004. [Online]. Available: http://www.sciencedirect.com/science/article/pii/S1360138504000512

[107] P. J. S. B. A. Bacic, A.; Harris, *The Biochemistry of Plants*. San Diego, CA: Academic Press, 1988, vol. 14, ch. Structure and function of plant cell walls, pp. 297–371.

[108] L. D. Talbott and P. M. Ray, "Molecular size and separability features of pea cell wall polysaccharides implications for models of primary wall structure," *Plant physiology*, vol. 98, no. 1, pp. 357–368, 1992.

[109] J. C. Thimm, D. J. Burritt, I. M. Sims, R. H. Newman, W. A. Ducker, and L. D. Melton, "Celery (apium graveolens) parenchyma cell walls: cell walls with minimal xyloglucan," *Physiologia Plantarum*, vol. 116, no. 2, pp. 164–171, 2002. [Online]. Available: http://dx.doi.org/10.1034/j.1399-3054.2002.1160205.x

[110] D. Cosgrove and m. Jarvis, "Comparative structure and biomechanics of plant primary and secondary cell walls," *Frontiers in Plant Science*, vol. 3, no. 204, 2012.

[111] H. Abe, R. Funada, H. Imaizumi, J. Ohtani, and K. Fukazawa, "Dynamic changes in the arrangement of cortical microtubules in conifer tracheids during differentiation." *Planta*, vol. 197, no. 2, pp. 418–421, 1995.

[112] H. Abe, R. Funada, J. Ohtani, and K. Fukazawa, "Changes in the arrangement of cellulose microfibrils associated with the cessation of cell expansion in tracheids," *Trees*, vol. 11, no. 6, pp. 328–332, 1997.

[113] Y. Imamura, H. Harada, and H. Saiki, "Electron microscopic study on formation and organization of cell wall in coniferous trachieds: criss-crossed and transition structures in secondary wall.[jap.; eng. summ.]," *Bull, Kyoto Univ. For*, vol. 44, pp. 183–193, 1972.

[114] M. McCann and K. Roberts, "Architecture of the primary cell wall," *The cytoskeletal basis of plant growth and form*, pp. 109–129, 1991.

[115] A. Wardrop, "The organization of the primary wall in differentiating conifer tracheids," *Australian Journal of Botany*, vol. 6, no. 4, pp. 299–305, 1958.

[116] A. B. Wardrop, *The formation of wood in forest trees*. Academic Press, 1964, ch. The structure of formation of cell wall in xylem, pp. 87–134.

[117] C. J. W. A. Harada, H., *Biosynthesis and biodegradation of wood components*. Ac, 1985, ch. Structure of wood, pp. 1–42.

[118] H. Abe, R. Funada, J. Ohtani, and K. Fukazawa, "Changes in the arrangement of microtubules and microfibrils in differentiating conifer tracheids during the expansion of cells," *Annals of Botany*, vol. 75, no. 3, pp. 305–310, 1995.

[119] D. J. Cosgrove, "Growth of the plant cell wall," *Nature Reviews Molecular Cell Biology*, vol. 6, no. 11, pp. 850–861, 2005.

[120] I. MacKinnon, A. Sturcova, K. Sugimoto-Shirasu, I. His, M. McCann, and M. Jarvis, "Cell-wall structure and anisotropy in procuste, a cellulose synthase mutant of arabidopsis thaliana," *Planta*, vol. 224, no. 2, pp. 438–448, 2006. [Online]. Available: http://dx.doi.org/10.1007/s00425-005-0208-6

[121] A. Wolters-Arts, T. Van Amstel, and J. Derksen, "Tracing cellulose microfibril orientation in inner primary cell walls," *Protoplasma*, vol. 175, no. 3-4, pp. 102–111, 1993.

[122] E. Frei and R. D. Preston, "Cell wall organization and wall growth in the filamentous green algae cladophora and chaetomorpha. i. the basic structure and its formation," *Proceedings of the Royal Society of London. Series B. Biological Sciences*,

vol. 154, no. 954, pp. 70–94, 1961. [Online]. Available: http://rspb.royalsocietypublishing.org/content/154/954/70.abstract

[123] J. F. Vincent, *Plant Biomechanics*. John Wiley & Sons, Ltd, 2001. [Online]. Available: http://dx.doi.org/10.1038/npg.els.0002062

[124] M. Koornneef and D. Meinke, "The development of arabidopsis as a model plant," *Plant Journal*, vol. 61, no. 6, pp. 909–921, 2010.

[125] G. W. Haughn and C. Somerville, "Sulfonylurea-resistant mutants of arabidopsis-thaliana," *Molecular & General Genetics*, vol. 204, no. 3, pp. 430–434, 1986.

[126] T. L. Western, J. Burn, W. L. Tan, D. J. Skinner, L. Martin-McCaffrey, B. A. Moffatt, and G. W. Haughn, "Isolation and characterization of mutants defective in seed coat mucilage secretory cell development in arabidopsis," *Plant Physiology*, vol. 127, no. 3, pp. 998–1011, 2001.

[127] Z. Hejnowicz and W. Barthlott, "Structural and mechanical peculiarities of the petioles of giant leaves of amorphophallus (araceae)," *American Journal of Botany*, vol. 92, no. 3, pp. 391–403, 2005.

[128] R. M. Haralick and L. G. Shapiro, *Computer and Robot Vision*, 1st ed. Boaton, MA, USA: Addison-Wesley Longman Publishing Co., Inc., 1992, vol. 1.

[129] N. Otsu, "A threshold selection method from gray-level histograms," *Systems, Man and Cybernetics, IEEE Transactions on*, vol. 9, no. 1, pp. 62–66, 1979.

[130] J. Canny, "A computational approach to edge detection," *IEEE Transaction of Pattern Analysis and Machine Intelligence*, vol. PAMI-8, no. 6, p. 20, 1986.

[131] K. F. Mulchrone and K. R. Choudhury, "Fitting an ellipse to an arbitrary shape: implications for strain analysis," *Journal of Structural Geology*, vol. 26, no. 1, pp. 143–153, 2004.

[132] C. B. Barber, D. P. Dobkin, and H. Huhdanpaa, "The quickhull algorithm for convex hulls," *Acm Transactions on Mathematical Software*, vol. 22, no. 4, pp. 469–483, 1996.

[133] T. Huang, T. Tsuji, M. R. Kamal, and A. D. Rey, "Structural characterization of grain pattern diversity in parametric space," *Journal of Materials Science*, vol. 34, no. 18, pp. 4551–4561, 1999.

[134] M. R. Kamal, T. Huang, and A. D. Rey, "Topological properties of polymer spherulitic grain patterns from simultaneous nucleation," *Journal of Materials Science*, vol. 32, no. 15, pp. 4085–4099, 1997.

[135] S. Chiu, "Aboav-weaire's and lewis' laws—a review," *Materials Characterization*, vol. 34, no. 2, pp. 149–165, 1995.

[136] F. T. Lewis, "A comparison between the mosaic of polygons in a film of artificial emulsion and the pattern of simple epithelium in surface view (cucumber epidermis and human amnion)," *The Anatomical Record*, vol. 50, no. 3, pp. 235–265, 1931.

[137] D. Aboav, "The arrangement of cells in a net," *Metallography*, vol. 13, no. 1, pp. 43–58, 1980.

[138] J. C. M. Mombach, R. M. C. de Almeida, and J. R. Iglesias, "Mitosis and growth in biological tissues," *Physical Review E*, vol. 48, no. 1, pp. 598–602, 1993.

[139] ——, "Two-cell correlations in biological tissues," *Physical Review E*, vol. 47, no. 5, pp. 3712–3716, 1993.

[140] P. Pina and M. A. Fortes, "Characterization of cells in cork," *Journal of Physics D-Applied Physics*, vol. 29, no. 9, pp. 2507–2514, 1996.

[141] G. L. Caer and R. Delannay, "The administrative divisions of mainland france as 2d random cellular structures," *J. Phys. I France*, vol. 3, no. 8, pp. 1777–1800, 1993.

[142] J. S. Huang and L. J. Gibson, "Microstructural design of cellular materials .1. honeycomb beams and plates," *Acta Metallurgica Et Materialia*, vol. 43, no. 4, pp. 1643–1650, 1995.

[143] P. Pina, J. Saraiva, L. Bandeira, and J. Antunes, "Polygonal terrains on mars: A contribution to their geometric and topological characterization," *Planetary and Space Science*, vol. 56, no. 15, pp. 1919–1924, 2008.

[144] P. Mulheran, "The scaling state in two-dimensional grain growth," *Acta Metallurgica Et Materialia*, vol. 42, no. 11, pp. 3589–3593, 1994.

[145] J. C. M. Mombach, M. A. Z. Vasconcellos, and R. M. C. d. Almeida, "Arrangement of cells in vegetable tissues," *Journal of Physics D: Applied Physics*, vol. 23, no. 5, p. 600, 1990.

[146] I. Alber, J. L. Bassani, M. Khantha, V. Vitek, and G. J. Wang, "Grain boundaries as heterogeneous systems: Atomic and continuum elastic properties," *Philosophical Transactions of the Royal Society of London. Series A: Physical and Engineering Sciences*, vol. 339, no. 1655, pp. 555–586, 1992. [Online]. Available: http://rsta.royalsocietypublishing.org/content/339/1655/555.abstract

[147] S. Nemat-Nasser and M. Hori, *Micromechanics: overall properties of heterogeneous materials*. Elsevier Amsterdam, 1999, vol. 2.

[148] R. Hill, "Elastic properties of reinforced solids: some theoretical principles," *Journal of the Mechanics and Physics of Solids*, vol. 11, no. 5, pp. 357–372, 1963.

[149] W. K. Liu, D. Qian, S. Gonella, S. Li, W. Chen, and S. Chirputkar, "Multiscale methods for mechanical science of complex materials: Bridging from quantum to stochastic multiresolution continuum," *International Journal for Numerical Methods in Engineering*, vol. 83, no. 8-9, pp. 1039–1080, 2010. [Online]. Available: http://dx.doi.org/10.1002/nme.2915

[150] X. Yin, W. Chen, A. To, C. McVeigh, and W. K. Liu, "Statistical volume element method for predicting microstructure—constitutive property relations," *Computer Methods in Applied Mechanics and Engineering*, vol. 197, no. 43 – 44, pp. 3516 – 3529, 2008, <ce:title>Stochastic Modeling of Multiscale and Multiphysics Problems</ce:title>. [Online]. Available: http://www.sciencedirect.com/science/article/pii/S0045782508000339

[151] M. Ostoja-Starzewski, "Material spatial randomness: From statistical to representative volume element," *Probabilistic Engineering Mechanics*, vol. 21, no. 2, pp. 112 – 132, 2006. [Online]. Available: http://www.sciencedirect.com/science/article/pii/S0266892005000433

[152] C. Chen, T. Lu, and N. Fleck, "Effect of imperfections on the yielding of two-dimensional foams," *Journal of the Mechanics and Physics of Solids*, vol. 47, no. 11, pp. 2235 – 2272, 1999. [Online]. Available: http://www.sciencedirect.com/science/article/pii/S0022509699000307

[153] V. Shulmeister, M. V. der Burg, E. V. der Giessen, and R. Marissen, "A numerical study of large deformations of low-density elastomeric open-cell foams," *Mechanics of Materials*, vol. 30, no. 2, pp. 125 – 140, 1998. [Online]. Available: http://www.sciencedirect.com/science/article/pii/S0167663698000337

[154] M. W. D. VanderBurg, V. Shulmeister, E. VanderGeissen, and R. Marissen, "On the linear elastic properties of regular and random open-cell foam models," *Journal of Cellular Plastics*, vol. 33, no. 1, pp. 31–54, 1997.

[155] N. T. Gridgeman, "Lamé ovalsy," *The Mathematical Gazette*, vol. 54, no. 387, pp. pp. 31–37, 1970. [Online]. Available: http://www.jstor.org/stable/3613154

[156] M. Ashby, "Overview no. 92: Materials and shape," *Acta Metallurgica et Materialia*, vol. 39, no. 6, pp. 1025 – 1039, 1991. [Online]. Available: http://www.sciencedirect.com/science/article/pii/0956715191901898

[157] S. C. Burgess, "Shape factors and material indices for dimensionally constrained structures part 1: Beams," *Proceedings of the Institution of Mechanical Engineers, Part C: Journal of Mechanical Engineering Science*, vol. 214, no. 2, pp. 371–379, 2000. [Online]. Available: http://pic.sagepub.com/content/214/2/371.abstract

[158] ——, "Shape factors and material indices for dimensionally constrained structures part 2: shaft," *Proceedings of the Institution of Mechanical Engineers, Part C: Journal of Mechanical Engineering Science*, vol. 214, no. 2, pp. 381–388, 2000.

[159] P. Weaver and M. Ashby, "Material limits for shape efficiency," *Progress in Materials Science*, vol. 41, no. 12, pp. 61 – 128, 1998. [Online]. Available: http://www.sciencedirect.com/science/article/pii/S0079642597100342

[160] D. Pasini, "Shape and material selection for optimizing flexural vibrations in multilayered resonators," *Journal of Microelectromechanical Systems*, vol. 15, no. 6, pp. 1745–1758, 2006.

[161] D. Pasini, S. Burgess, and D. Smith, "A method for selecting macro-scale structures with axially loaded members," *International Journal of Mechanics and Materials in Design*, vol. 3, pp. 185–199, 2006. [Online]. Available: http://dx.doi.org/10.1007/s10999-007-9022-6

[162] D. Pasini, D. J. Smith, and S. C. Burgess, "Structural efficiency maps for beams subjected to bending," *Proceedings of the Institution of Mechanical Engineers Part L-Journal of Materials-Design and Applications*, vol. 217, no. L3, pp. 207–220, 2003.

[163] B. Agarwal, *Programmed Statistics (Question-Answers)*. New Age International (P) Limited, 2007. [Online]. Available: http://books.google.ca/books?id=QlC-Yiy_ZDsC

[164] H. J. Al-Gahtani, "Geometric and inertial properties of areas enclosed by irregular boundaries."